Inaugural - Dissertation

zur
Erlangung der Doktorwürde
der
Gesamtfakultät für Mathematik-,
Ingenieur- und Naturwissenschaften
der
Ruprecht-Karls-Universität
Heidelberg

vorgelegt von

M.Sc. Christine Arndt

aus Göttingen

Tag der mündlichen Prüfung

19. Juli 2022

Microengineered conductive scaffolds for cell-based actuation

Referees:

Prof. Dr. Christine Selhuber-Unkel
Prof. Dr. Rasmus R. Schröder

To my family and friends

"There's only us, there's only this. Forget regret or life is yours to miss. No other course, no other way, no day but today."
— Jonathan Larson, *RENT*

"On I go, to wonder and to learning. Name the stars and know their dark returning. I'm calling, to know the world's true yearning. The hunger that a child feels for everything they're shown."
— Steven Sater, *Spring Awakening*

Abstract

A functional 3D-engineered scaffold where cells are able to grow *in vitro* mimics the microstructural, mechanical, electrical and biochemical features of the cell's natural extracellular matrix (ECM) that is crucial for supporting numerous cell functions such as proliferation and growth. The scaffolds electrical conductivity and deformability are particularly essential for assorted cell types that rely on electrical signals to perform various cellular mechanical functions as in skeletal muscle cells contraction that transpire upon electrical stimulation. My thesis presents successful procedures for developing electrically-conductive, deformable 3D artificial cellular scaffolds that provide the deformability to accommodate muscle cell contraction and the electrical conductivity to enable cell-to-cell signalling, both of which are vital aspects in 3D cell tissue scaffolds and biohybrid robotics. I employed a novel microengineering approach based on a sacrificial template made from interconnected tetrapod-shaped zinc oxide micro particles with two state of the art methods that are based on (1) a hydrogel permeated with a filler material that renders it conductive and (2) a conductive polymer.

The hydrogel system is based on polyacrylamide where the interconnected zinc oxide microchannels network is coated with an exfoliated graphene flakes dispersion that eventually creates a graphene framework structure and promotes an outstanding electrical conductivity using an extremely low filler concentration. This method imposes no significant impact on the hydrogel mechanical integrity and maintains the original matrix toughness and physicochemical properties, thus achieves versatile, conductive, microchannel-containing 3D scaffolds. Composites of polyacrylamide and a semi-synthetic gelatin methacryloyl hydrogel were also developed as a facile way of generating a biofunctional conductive scaffold that enhances and promotes skeletal muscle cells spreading and proliferation. Additionally, the suitability of non-contractile fibroblast cells for biohybrid actuators is analyzed and presented in a pioneering study.

In the second microengineered system, I analyzed a 3D fibrous conductive scaffold based on a conductive poly(3,4-ethylenedioxythiophene):polystyrene sulfonate (PEDOT:PSS) polymer that proved suitable for culturing contractile cells. The scaffolds exhibit four orders of magnitude greater specific conductivity than previously reported 3D PEDOT:PSS structures even after two weeks of storage in water in addition to demonstrating a substantial mechanical stability in an aqueous environment. Biofunctional studies with fibroblasts, skeletal muscle cells and cardiomyocytes derived from induced pluripotent stem cells cultured on biofunctionalized scaffolds were carried out in terms of cell adhesion, distribution, beating behavior and their scaffold deformation ability.

Zusammenfassung

Eine funktionale 3D-Gerüststruktur in der Zellen *in vitro* wachsen können, muss die mikrostrukturellen, mechanischen, elektrischen und biochemischen Eigenschaften der natürlichen extrazellulären Matrix nachbilden, die für die Unterstützung zahlreicher Zellfunktionen wie z.B. Proliferation und Wachstum entscheidend sind. Die elektrische Leitfähigkeit und Verformbarkeit der Struktur sind dabei besonders wichtig für die Zelltypen, die auf elektrische Signale angewiesen sind, um verschiedene zelluläre mechanische Funktionen auszuführen, wie beispielsweise die durch elektrische Stimulation ausgelöste Kontraktion von Skelettmuskelzellen. In meiner Dissertation stelle ich Herstellungsverfahren für elektrisch leitfähige, verformbare künstliche 3D-Zellgerüste vor, die die nötige Verformbarkeit für die Kontraktion von Muskelzellen und die elektrische Leitfähigkeit für die Zellsignalübertragung bieten, welches beide wichtige Aspekte für die 3D-Zellkultur und biohybride Robotik sind. Dafür habe ich ein neuartiges, mikrotechnisches Verfahren angewandt, das auf einem Opfertemplat aus miteinander verbundenen, tetrapodenförmigen Zinkoxid-Mikropartikeln basiert, wobei die Methoden entweder auf (1) einem Hydrogel, das mit einem leitfähigen Füllstoff durchsetzt ist, oder (2) einem leitfähigen Polymer basieren.

Das Hydrogelsystem beruht auf Polyacrylamid (PAM), bei dem das Zinkoxid-Mikrokanalnetzwerk mit einer Dispersion aus exfolierten Graphenflocken (EG) beschichtet und schließlich entfernt wird, sodass eine das Hydrogel durchziehende Graphengerüststruktur entsteht, wodurch dieses bei einer extrem niedrigen Füllstoffkonzentration eine hervorragende elektrische Leitfähigkeit aufweist. Diese Methode hat keine nennenswerten Auswirkungen auf die mechanische Integrität des Hydrogels und erhält die ursprüngliche Zähigkeit und die physikalisch-chemischen Eigenschaften der Matrix, wodurch anpassbare, leitfähige und mit Mikrokanälen durchzogene 3D-Gerüststruktur entstehen. Zusätzlich wurden Komposite aus PAM und einem Gelatine-Methacryloyl-Hydrogel entwickelt, um auf einfache Weise eine biofunktionale, leitfähige Gerüststruktur zu erzeugen, die die Adhäsion und Proliferation von Skelettmuskelzellen verbessert. Darüber hinaus wird die Eignung von nicht kontraktilen Fibroblastenzellen für biohybride Aktoren analysiert und in einer wegweisenden Studie vorgestellt.

Im zweiten Ansatz wird eine faserartige 3D-Gerüststruktur analysiert, die auf dem leitfähigen Polymer Poly(3,4-Ethylendioxythiophen):poly(Styrolsulfonat) (PEDOT:PSS) basiert und für die Kultivierung kontraktiler Zellen geeignet ist. Die Strukturen weisen selbst nach zweiwöchiger Lagerung in Wasser eine um vier Größenordnungen höhere Leitfähigkeit auf als bisher beschriebene 3D-PEDOT:PSS-Strukturen und zeigen darüber hinaus eine geeignete mechanische Stabilität in wässrigen Umgebung. Biofunktionalitätsstudien an Fibroblasten, Skelettmuskelzellen und Kardiomyozyten aus induzierten pluripotenten Stammzellen wurden im Hinblick auf Adhäsion, Verteilung, Kontraktion, sowie ihrer Fähigkeit ihre umgebende Struktur zu deformieren, analysiert.

Contents

Objective

Electrically conductive hydrogels are used in biosensors [1–4], bioelectronics [5–7], biomedical scaffolds for nervous [8, 9] or cardiac [10, 11] functional tissue [12], as well as in biohybrid robotics [13] where cell contraction causes material actuation. Most of the cells that are suitable for biohybrid actuation can be electrically stimulated, hence sufficient material conductivity is essential for spreading the electrical signals efficiently. [13] Using a conductive hydrogel that promotes cell-to-cell signals to enhance the biohybrid actuator function is advantageous as demonstrated by cardiomyocytes embedded in electrically conductive scaffolds that expressed higher connexin-43 and showed better beating characteristics and elongated morphology. [14, 15] Besides electrical conductivity, the scaffold is required to be soft to allow robotic actuation and withstand repeated contraction cycles yet able to provide structural integrity to support the cells. Also, as cells demonstrate acute mechanosensitivity to their extracellular matrix, the scaffold material stiffness and the physicochemical properties of the matrix material are essential contributing factors. [13, 16] Additionally, vascularization of the scaffold is an important factor to ensure sufficient nutrient and waste transport as well as oxygen diffusion when preparing scaffolds that exceeds a thickness of approximately $500 \, \mu m$. [17, 18] Therefore, besides the biocompatibility and biofunctionality, scaffolds for cell-based actuation need to meet certain requirements such as (a) sufficient electrical conductivity of at least $0.1 \, S \, m^{-1}$, (b) appropriate mechanical properties of around $20 \, kPa$, (c) reasonable elasticity to withstand repeated contraction cycles and (d) suitable pores or microchannels for oxygen diffusion, nutrient and waste transport.

A scaffold that fulfils these objectives can either be based on a mechanically-apt, conductive polymer or a hydrogel with an added conductive filler material in its matrix that is attainable through solution mixing, postpolymerization or *in situ* polymerization. [1, 19] However, whereas the drawback of the latter technique is that it requires additional processing steps, [19] postpolymerization is prone to inhomogeneity [1] and solution mixing necessitates the addition of high filler amounts that eventually alter matrix properties and often lead to matrix reinforcement. [20] Ultimately, finding a strategy for preparing biofunctional, conductive hydrogels with high conductivities at low filler concentration as well as appropriate mechanical and physicochemical properties is a scope of this work. This scope was also approached using inherently conductive polymers after overcoming a fundamental drawback represented by the much smaller conductivity of 3D scaffolds than that of heart tissue. This could be achieved through exploring scaffold materials with a fibrous structure that are soft enough to enable cell-induced contraction and have sufficiently high electrical conductivity for cell-based actuation. In soft actuators and artificial muscles research, stimuli-responsive polymers, like thermoresponsive hydrogels, offer great possibilities for their ability to respond to environmental changes, however their slow response rates and comparably weak force

generation capabilities are limiting their use. Also, biohybrid actuators reported in literature are mostly powered by contractile cells [21,22], whole tissue [23,24] or bacteria [13], but fibroblast cells, which exert the necessary tensile forces to support wound closure, were not explored yet. Thus, two additional aims in this thesis were to study force generation and volume change in thermoresponsive matrices and whether they can be effectively enhanced by microengineering, and also, to develop a novel strategy to exploit the fibroblasts' potential as cellular motors in biohybrid actuators.

This thesis is divided into three parts. In the first part, a biological background and an introduction to synthetic scaffolds for cell cultivation are given. In the second part, I present a novel microengineering approach to fabricate functional hydrogels for cell-based actuation and analyze their potential as scaffolds for biohybrid actuators. I also explore the use of fibroblast cells as actuators for cell-induced scaffold contraction. In the last part of my thesis, a 3D soft, fibrous, conductive scaffold for cell-based actuation is presented and discussed.

1 | Introduction

In biohybrid robotics, living biological systems like cells are implemented in robotic systems to perform as actuators. An actuator is the part of a machine that converts, for instance, electrical or hydraulic energy into mechanical work that enables a physical movement. Whereas actuators function to perform a mechanical action in a robot, hundreds of muscles in the human body are similarly able to convert energy into some form of motion that is regulated by the nervous system. A miniaturized form of a biohybrid robot is achievable through exploiting the forces exerted by cells on their environment to power the system. Due to their softness and their compliant actuation possibilities, such robotics would be advantageous in medical applications especially when in close contact to humans where rigid objects impose a potential hazard. Biohybrid robots have the potential to sense, respond and adapt to environmental changes, and can thus be used in toxicity assessment and drug screening. They are typically less harmful to the environment and more lightweight than conventional robots as they require nutrients instead of batteries to function.

In this chapter, different contractile cell types as well as the requirements for a suitable cell matrix where cells are allowed to develop and transfer their cellular forces are presented in Section 1.1, with a more detailed insight into different matrix materials given in Section 1.2.

1.1. Cells as motors for biohybrid actuators

Pneumatic, thermal, photo- or electrical field actuation are commonly used in non-biohybrid soft robotics whereas in biohybrid actuation, living biological material drives the robotic system. [25–27] A large variety of cell and tissue types have been used and tested in biohybrid devices including mammalian cells as well as insect cells or even whole animals, [13] however muscle cells are most commonly used for their ability to contract and exert forces on their environment. In vertebrates, there are three different kinds of muscle tissue: skeletal and cardiac muscles that belong to the striated muscle tissue which are responsible for the voluntary movement and pumping of blood, respectively. The third type smooth muscle tissue is present in organs with involuntary movements like our stomach, intestines or blood vessels. [28, 29] The main difference between striated and smooth muscle tissue is the presence of muscle-specific complexes

called sarcomeres, which are the smallest contractile units that consist of repetitive actin-myosin units. [29, 30] Biohybrid actuation necessitates the ability of muscle cells to be stimulated in order to trigger contraction, thus smooth muscle tissue can not be employed and the focus in biohybrid applications is primarily on striated muscle tissue. Still, other non-contractile mammalian cell types like fibroblast might be used for biohybrid actuation. Fibroblasts are able to exert tensile forces in the form of contraction that plays an important role in wound healing upon injury as tissue lose their mechanical integrity. [31]

1.1.1. Cell contraction and stimulation in striated muscle tissue

Contraction in cells is an interplay mediated by actin and myosin proteins interactions that are generally responsible for many types of cellular movements and are present in the sarcomere, the smallest contractile unit. Here, actin and myosin are anchored in the so-called Z-disk (also Z-bands), which are optically dense and visible under a microscope so they define the boundary of each sarcomere. [30] In a sarcomere, the myosin bundles slide along the actin filaments and thus lead to the shorting of the sarcomere structures that eventually results in muscle contraction. In cardiomyocytes, nearly the whole cytoplasmic space is filled with parallel oriented and aligned sarcomeres. [30] The sarcomeres are connected to the cell membrane through costameres that are structural components responsible for force-transmission to the extracellular matrix. [32]

The difference in the contractile behavior between cardiac and skeletal muscle tissue is that the former is able to contract spontaneously whereas the latter lacks specific ion channels that are responsible for spontaneous membrane depolarization, hence a contraction stimulus must be provided by a nerve pulse or an external trigger. [33] Albeit cardiomyocytes seem to be a better choice for biohybrid actuators at first glance, skeletal muscle cells offer in fact a higher force output and produce faster locomotion than cardiomyocytes when cultured under the same conditions on the same device. [34] Another difference between the two tissue types is represented by the skeletal muscle ability to regenerate in comparison to the cardiac muscle cells annual renewal rate that is limited to only 1 % at the age of 25 in humans and decreases even more with age. [35, 36] Either way, actuation via cardiomyocytes or skeletal muscle cells can be controlled precisely by applying electrical stimuli or, when optogenetically modified, by light pulses. [23]

Cardiac cells demonstrate an action potential that lasts for over 200 ms compared to the two milliseconds long one in skeletal muscle cells. An action potential is the characteristic membrane potential deviation from the resting potential that takes place when a cell is excited and it shows a cell-specific electrical signal course and spread over the cell membrane. The threshold potential is approximately - 55 mV where voltage-gated ion channels are activated and opened in a chained sequence to enable ion currents.

During this sequence of opening and closing processes, the channels are temporarily changing the membrane current for different ions that, together with these short ion currents, give rise to the characteristic action potential curve that is cell specific and independent of the triggering stimulus as shown schematically in Figure 1.1 for skeletal and cardiac muscle cells. [37]
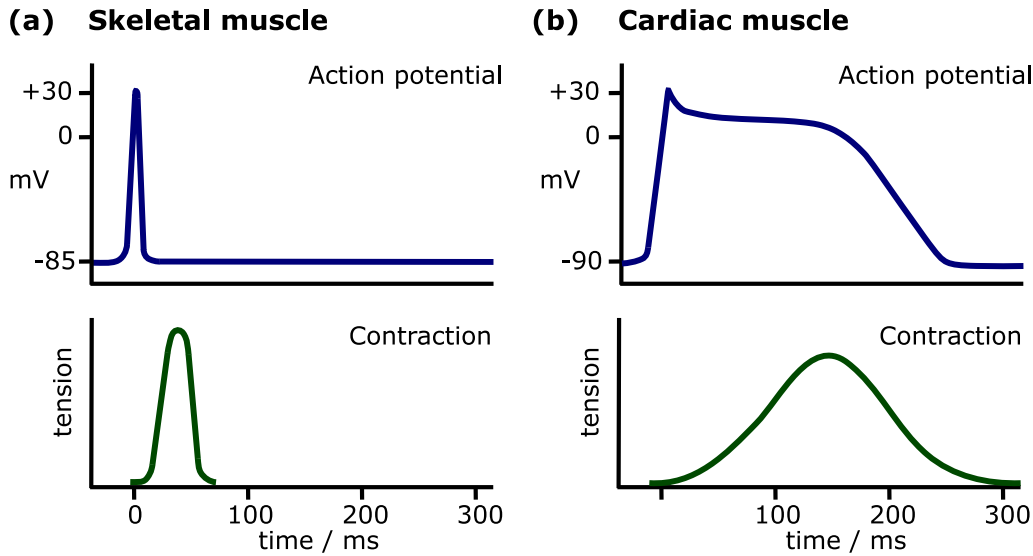
Figure 1.1. *Action potentials and maximum of contraction tension of a) skeletal and b) cardiac muscle tissue. Skeletal muscle cells demonstrate a short action potential and steep increase in muscle tension whereas the action potential from cardiac cells can last for over 200 ms. Adapted from [37]*

1.1.2. Skeletal muscle cells

Skeletal muscles are the primary actuators in mammals with an ability to operate over a wide range of lengths, forces and frequencies that make them good candidates for biohybrid robotic applications. [13] Muscle precursor cells, so called myoblasts, proliferate rapidly under high serum conditions but fuse into a syncytium with multiple cell nuclei to form long, tubular-like structures called myotubes under low serum conditions. [28] An example of C2C12 mouse myoblasts fused into myotubes after two days in low serum conditions is shown in Figure 1.2 a and first striated myofibrils formed orthogonal to the nuclei chain are highlighted in Figure 1.2 b.

When the myotubes mature, cell nuclei migrate to the outside. The whole muscle formation process is called myogenesis and is shown in Figure 1.3 using the C2C12 mouse myoblast cell line as an example. Cell nuclei in myotubes are no longer able to divide but the so called satellite cells are present in the basal membrane of muscle
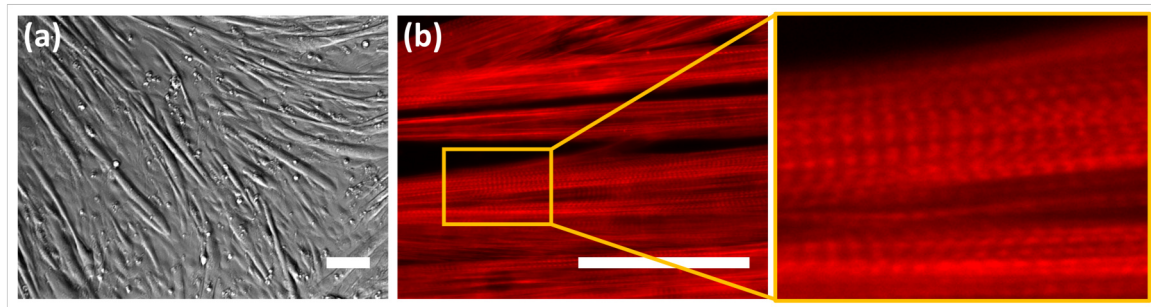
Figure 1.2. *C2C12 skeletal muscle cells. a) Myoblasts grown on cell culture plastic fused into elongated, multinucleated myotubes and imaged in phase contrast 2 days after changing to starvation medium. b) Myotubes stained after 7 days for F-actin fibers with SiR-actin visualizing the striated myofibrils. Scale bars: 100 µm. (Own work)*

fibers, which are in a quiescent and undifferentiated state and can enter the mitotic circle. [13,28] In order to generate *in vivo*-like structures and functions of skeletal muscle cells *in vitro*, a compliant substrate stiffness is particularly important for sarcomere formation. [38] As muscle strains are normally around 20 % but can also reach over 40 % in some scenarios [39], a call for compliant substrate stiffness and elasticity is essential.
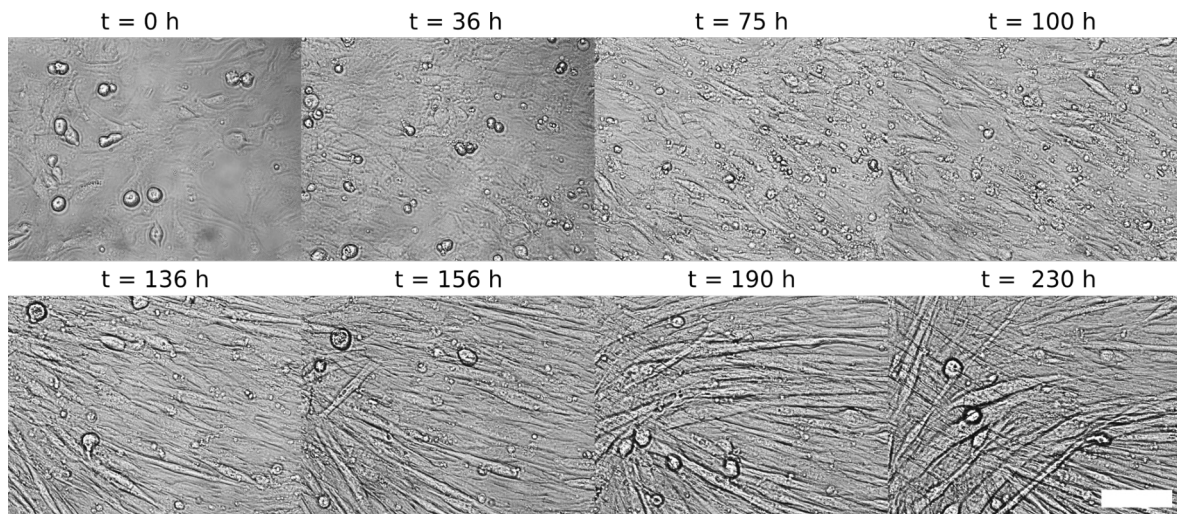
Figure 1.3. *Timeline of the myogenesis of C2C12 mouse skeletal muscle cells grown on cell culture plastic over a period of 9.5 days. Scale bar: 100 µm. (Own work)*

Myocytes fuse into myotubes even on glass or tissue culture plastic but they do not form sarcomeres unless the scaffold stiffness matches that of the native muscle tissue (approx. 12 kPa). [13, 40] Myotube organization can be guided by physical or topographical features, e.g., by using electrospun nanofibers to align myotubes uniaxially. [41, 42] For sarcomeric structure development and maturation, not only a compliant substrate

stiffness is necessary, but the cells need to actively contract and work against a load, which makes suitable electrical, mechanical or optical stimulation necessary. [38,43,44] An electrical stimulation resulted in periodic membrane depolarization and contraction that supports the regulation of cell-cell and cell-matrix interactions and thus lead to enhanced alignment and myotube formation [23,44], whereas a mechanical stimulation promoted proliferation, myofiber organization, gene regulation and protein expression. [45] A non-invasive, contact-free and thus less harmful way to stimulate cells is the use of optogenetically modified cells that react to light triggers, which offer higher spatial and temporal precision in comparison to electrical stimulation. [13,46] All in all, an exercise training during differentiation increases force output [23] and shows that biohybrid devices are able to dynamically adapt to their environment. [47]

1.1.3. Cardiac muscle cells

Cardiac muscle cells (cardiomyocytes) are a common and sensible choice in biohybrid actuators due to their ability to synchronize and beat spontaneously with no stimulation required, provided that the cells are connected in a closed cell biofilm. Still, even when the cells on a scaffold are dispersed, a synchronized beating can be attained through electrical stimulation as long as the substrate is sufficiently conductive. [48,49] Therefore, remodeling the native environment of cardiomyocytes is necessary for a successful native myocardium mimicry and a suitable conductive pathways formation that are essential for establishing functional gap junctions. The latter are intercellular channels that mediate direct communication via small molecules and ions passive diffusion and are responsible for transferring electrical signals that are required for the synchronized cardiac contraction in a native heart tissue. [27,50,51] The electrical conductivity (DC) of a heart tissue is around $0.1\,\mathrm{S\,m^{-1}}$. [48] Despite the solid progress in heart tissue engineering, the realization of a heart-like system remains a great challenge [52] due to the complexity of achieving electromechanical coupling through artificial fabrication. Tackling this obstacle by using, e.g., conductive materials can pave the way for a sustainable system that properly resembles a heart. In that context, neonatal rat cardiomyocytes isolated from 1 to 3 days old rat represent a suitable cell type, however bear the disadvantage of being extracted from animals and cannot be proliferated in cell cultures. [53] Nevertheless, neonatal rat cardiomyocytes are the most commonly used cells in biohybrid robotics. One of the prominent examples is the work of Shin *et al.* [21] who mimicked the shape of batoid fish using primary cardiomyocytes seeded on a hierarchically structured hydrogel scaffold that incorporates flexible gold microelectrode array for actuation. Another milestone was presented by Park, Parker and co-workers [54] who combined optogenetically modified primary cardiomyocytes on structured poly(dimethylsiloxane) thin films that enclose a microfabricated gold skeleton in the shape of a tissue engineered ray. In a recent work, the same group developed an autonomously swimming biohybrid fish powered by a bilayer of cardiomyocytes using the cardiac mechanoelectrical signaling capabilities for a closed-loop actuation

cycle, employing also human cardiomyocytes derived by induced pluripotent stem cells (iPSC; Figure 1.4) besides primary rat cardiomyocytes. [22] Cardiomyocytes derived from iPSCs also led to a significant progress in cardiac tissue engineering. [55, 56]
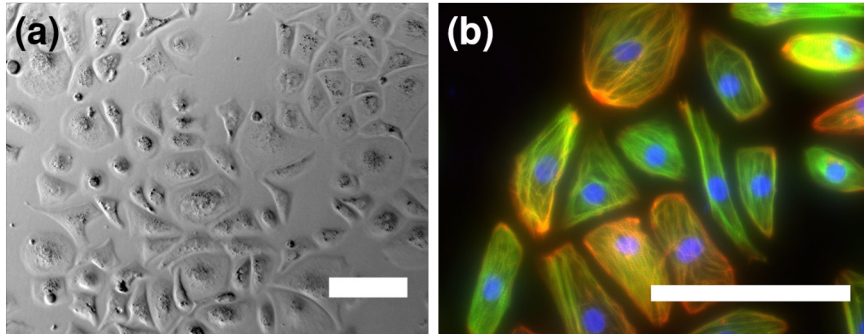
Figure 1.4. *Cardiomyocytes derived from induced pluripotent stem cells[1] (iPSC-CM). a) iPSC-CM cultured on fibronectin-coated glass slides after 24 hours imaged in phase contrast. b) iPSC-CM cultured for 48 hours on fibronectin-coated glass slides and immunofluorescently stained with Hoechst (nucleus, blue), anti-myosin (myosin heavy chain 7, green) and rhodamine-phalloidin (actin filaments, red) with striated cytoskeletal organization visible. Scale bars: 100 μm. (Own work)*

Although not naturally present in the human body, iPSCs originate from fully differentiated cells that were induced to return to their primary state with properties similar to embryonic stem cells, which are capable of differentiating into any cell type again. [57] iPSCs were first derived from mouse somatic cells using a combination of four retrovirally transduced transcription factors (*Oct3/4, Sox2, Klf4, c-Myc*) [57]. Soon after, human fibroblasts have been successfully induced to human iPSCs as well, laying the foundation for disease-specific iPSC cell lines generation from patients. [58] Albeit the high cost of iPSCs culture that might be a limiting factor, these cells offer great potential for providing more ethically-accessible cells in biohybrid actuators without sacrificing animals.

1.1.4. Cell-material interaction

Cell adhesion is a crucial mechanism for cell-cell [59] and cell-extracellular (ECM; Figure 1.5) matrix interactions that constitute the physiological connections in tissue. The ECM typically consist of large glycoproteins like collagen, elastin, fibronectin and laminin [60, 61] and its connection with the cell membrane is mediated by transmembrane glycoproteins and cell adhesion molecules such as cadherins, selectins and integrins. [61] Consisting of an α- and a β-subunit, integrins are the most important

---

[1]iPSC-CMs and media were kindly provided by Dr. Ayca Seyhan Agircan and Prof. Dr. Johannes Backs from Heidelberg University Hospital.

receptors in the cell membrane for their role in binding to ligands in ECM as well as to collagen, fibronectin and laminin, which require calcium and often a short amino acid sequence such as Arg-Gly-Asp (RGD). In myocardium, the RGD is found in repeating segments of fibronectin that facilitates cell-matrix binding through the activity of the $\alpha 5\beta 1$ integrin complex [62, 63], hence integrins are essential for a stable intracellular cytoskeleton connection with the ECM. Thus, the growth of cells on a material surface relies on the availability of suitable binding proteins [59,60] in addition to other factors such as surface charge, topography, stiffness and hydrophilicity. [64]
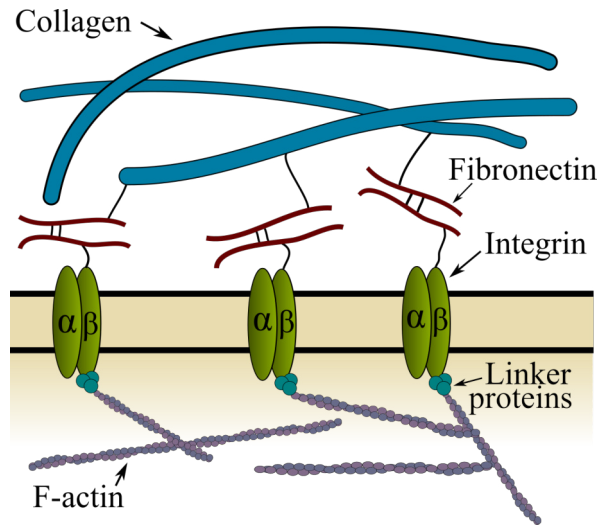
Figure 1.5. *The cell surface is linked to the extracellular matrix (ECM) consisting mainly of collagen by integrins and the linker protein fibronectin. The β-domain of the integrin is connected to F-actin, which provides a stable connection between the intracellular cytoskeleton and the ECM. Adapted from [60].*

1.1.5. Mechanotransduction

Mechanosensing describes the cellular behavior in response to mechanical signals that a cell experiences which influences its functional behavior in terms of spreading, proliferation, migration and differentiation. The mechanical forces can be emanated from the extracellular matrix or neighboring cells and then transduce into biomechanical signals that trigger numerous structural and functional responses in the cell. [65] Mechanical forces are transmitted in eukaryotes from the extracellular matrix to the cell's cytoskeleton, e.g., through integrins, which in turn are connected to the actin filaments through a number of linker proteins such as vinculin, paxillin, zyxin and talin. [16] For instance, extracellular signals arising from the underlying substrate stiffness, form and topography have been shown to affect cell fate [16] and dictate mesenchymal stem cells differentiation *in vitro*. [66] Also, fibroblasts cultured on solid substrates demonstrated enhanced cell growth whereas soft substrates induced cell apoptosis. [67] Engler *et*

al. [68] illustrated that the beating behavior of embryonic cardiomyocytes was ideal on matrices with a stiffness in the range of a healthy native tissue (10 - 20 kPa) while stiffer substrates similar to that of a post-infarct fibrotic scar inhibited beating. Thus, the contractile work done by cardiomyocytes is dependent on the underlying substrate stiffness as cells transmit actin-myosin contractions through their anchorage points onto the substrate: A cell can shorten its length (concentric contraction), maintain it against resistance (isometric contraction) or resist extension (eccentric contraction). [40] The work output is at its highest with a matrix elasticity around 10 kPa and decreases when the substrate is softer (negligible work output around 1 kPa) or stiffer (higher than 60 kPa). It has also been demonstrated that geometrical constraints impact cell behavior. Cells grown on substrates without constraints show active growth while cells undergo apoptosis when their spreading was restricted. [69] Taken together, shape, geometry and substrate rigidity need to be taken into careful consideration when designing artificial cell scaffolds.

1.1.6. Forces generated by cells

In addition to sensing their environment, mammalian cells constantly apply contractile forces onto the substrate they are cultured on. The forces are generated by the actin and myosin filaments and propagate through the stress fibers down to the integrins in focal adhesions that in turn are responsible for force transmission to the underlying substrate. Focal adhesions apply forces and stresses in the nN and kPa ranges, respectively. [70] According to Klein *et al.* [71], a single cardiomyocyte cell can generate a force of 40 to 60 nN, whereas mature adult cardiomyocytes can induce forces in the µN regime as a single cell and up to 40 to 80 mN per square millimeter as a 3D tissue. Also, Kajzar *et al.* [30] measured myocyte forces on a PDMS pillar array to be around 400 nN upon contraction and 140 nN in the relaxed state. The difference between the reported forces is either because the myocytes in some of these studies were externally stimulated by electrical pulses or calcium activation, or because the cells were cultivated and tested in two or three dimensions, with the latter showing smaller forces than cells cultured on flat or topographically structured 2D substrates in general. [30, 71] Moreover, a skeletal human muscle produces up to 0.35 MPa stresses at strains higher than 40 % for more than 10^9 life cycles [7] and a single skeletal muscle myotube is reported to generate a force of around 1 µN. [72] Passive tension forces generated by a C2C12 skeletal muscle strip were measured to be 1940 µN, whereas active tension forces under electrical stimulation were 195 µN. [23]

1.2. Synthetic scaffolds for cell cultivation

Cells experience a wide range of stiffness in the body that impact basic cellular processes like proliferation, migration and differentiation of, for instance, stem cells. [66]

Culturing cells on stiff substrates like cell culture plastic or glass does not adequately mimic physiological conditions, hence soft substrates with tunable mechanical properties can offer both passive and non-intrusive means to analyze cell behavior *in vitro*. For example, when considering actomyosin forces generated by contractile cells like cardiomyocytes, using an appropriately soft substrate would be crucial for their contraction whereas the rhythmic beating behavior would vanish when cultured on plastic. [68] To provide a suitable environment that mimics *in vivo* conditions, hydrogels are excellent candidates.

1.2.1. Hydrogels as scaffold materials

Hydrogels are three dimensional crosslinked networks of polymer chains with a complex viscoelastic behaviour [73] due to a large number of hydrophilic groups (e.g., $-COOH$, $-OH$, $-NH_2$) that enables them to absorb and hold a great amount of water (up to 98%) or other aqueous solutions while still be able to withstand dissolution through the crosslinking of polymer chains. [74, 75]. They are promising materials for biomedical applications like cell culture substrates, tissue engineering and drug delivery systems, because of their similarity to the extracellular matrix environment, their biodegradability, biocompatibility, their tailorable mechanical properties and high water content. [74, 75] The latter helps with the diffusion of nutrients, proteins and chemical signal molecules from and towards cells. Additionally, hydrogels can serve as the framework for functional materials that can be used to control cells by external cues, such as material-induced stimuli and material structures. The mechanical properties of hydrogels can be tailored, e.g., by the initial monomer and crosslinker concentrations, the polymerization temperature, as well as the swelling degree at the measurement time point. Thus, the stiffness of different tissue such as brain (a few kPa) or cartilage (a few MPa) can be matched in order to resemble *in vivo* conditions to a large extent [76, 77] in addition to the physical and chemical properties that can also be tailored to meet a wide range of unique requirements for any specific purpose. [74]

Hydrogels can have either natural or synthetic origins. Natural hydrogels (e.g., gelatin) have the advantage that they are inherently biocompatible and biodegradable with moieties that promote cellular activities but are often unable to provide the necessary mechanical stability under physiological conditions, [78] whereas synthetic hydrogels, on the contrary, offer customizable mechanical properties but lack the inherent bioactive features. Generally, the latter shortcoming can be overcome through tailoring the hydrogel chemical structure to acquire the required bioactive properties. [78] Hydrogels can also be classified according to their bond type. Physical hydrogels are connected via ionic or hydrogen bridge bonds hence prone to degradation, yet also known as reversible gels with self-healing properties. [79] On the other hand, chemical hydrogels have covalent bonds and are often crosslinked via radical polymerization (cf. Section 1.2.2) whereby the initiator can vary. My work focuses on this type of hydrogels.

In the field of biomedical engineering, stimuli-responsive hydrogels, also known as smart materials, have attracted a lot of interest for the high degree of control over material properties through reacting to external cues such as temperature, light and pH. Thermoresponsive hydrogels are among the most studied as tools to be employed for modifying substrate stiffness reversibly by an external trigger as well as their ability to be controlled easily and thus ultimately promote a wide range of applications, e.g., in drug delivery applications. [80,81] A prominent example for a temperature-sensitive hydrogel is N-isopropylacrylamide (PNIPAM, cf. Section 1.2.3) because its temperature response is close to the human body temperature. [82,83]

1.2.2. Radical polymerization

Hydrogels are commonly crosslinked by free radical polymerization, which consists of a three-step reaction. In the initiation step, free radicals are formed by light, temperature or redox initiators, which are targeting the vinyl or methacrylate groups of the hydrogel monomers. In the propagation step, radicals formed from the initiators are transferred to the monomer units and a polymer chain grows through monomer combination up until the reaction is either terminated by a monomer deficiency or by a radical combination (termination step). [84,85]

As a common initiator, the chemical oxidizer ammonium persulfate (APS) in combination with a catalyst like N, N, N', N'-Tetramethylethylenediamine (TEMED) can be used, however to mediate reactions in a controlled manner, the use of light as an external regulator is highly attractive. Photoinitiators like phenyl-2,4,6-trimethylbenzoylphosphinate (LAP), 2-Hydroxy-4'-(2-hydroxyethoxy)-2-methylpropiophenone (Irgacure 2959) or Riboflavin are used, which can be activated by UV light (365 or 405 nm). [86] The exposure or UV dose H_v used for photopolymerization is expressed as the radiant energy Q per area, or equivalently as the integral of the irradiance E over a certain time period Δt:

$$H_v = \frac{dQ}{dA} = \int_{\Delta t} E(t) \, dt. \tag{1.1}$$

1.2.3. Synthetic hydrogels

Two different synthetic hydrogels are used in this work, namely polyacrylamide and the thermoresponsive hydrogel poly-N-isopropylacrylamide, which are both formed by radical co-polymerization.

Polyacrylamide Polyacrylamide (PAM), a synthetic, chemical hydrogel, is formed by co-polymerization of acrylamide and N, N'-methylenebisacrylamide (bis-acrylamide). It is well-known in literature for its adjustable stiffness that can be altered by the

amount of the crosslinker bis-acrylamide, leading to a stiffness that ranges from 0.5 up to 740 kPa. [87] Notably, despite being inert to cell adhesion as it lacks bioactive moieties, crosslinked polyacrylamide is biocompatible and hence suitable for medical and biological applications as well-established protocols show protein coupling. [76] The reaction to form polyacrylamide is a vinyl addition polymerization initiated by a free radical-generating system that commonly consists of ammonium persulfate (APS) and N, N, N', N'-tetramethylethylenediamine (TEMED) in an oxygen-free environment. TEMED serves as a catalyst since it accelerates the formation rate of free radicals formed by persulfate. The reaction scheme is shown in Figure 1.6. Bis-acrylamide statistically crosslinks the long, covalently linked acrylamide chains and the stiffness of polyacrylamide can be tailored by varying the amount of crosslinkers and time for crosslinking. [74] Since the reaction is based on free radicals, every element serving as a radical trap, like for instance oxygen, inhibits the acrylamide polymerization reaction.
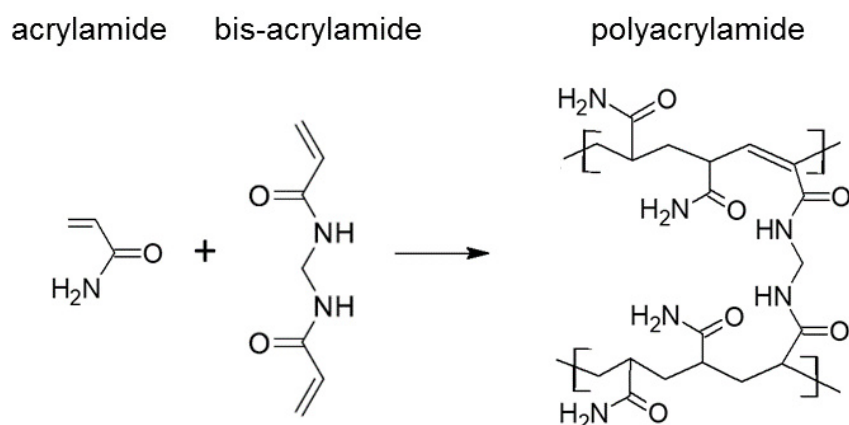
Figure 1.6. *Formation of polyacrylamide by a vinyl addition polymerization of acrylamide and N, N'-methylenebisacrylamide.*

Poly-N-isopropylacrylamide Poly-N-isopropylacrylamide (PNIPAM) is a thermoresponsive hydrogel with a so-called lower critical solution temperature (LCST). Depending on whether they exhibit an LCST or an upper critical solution temperature (UCST), thermoresponsive hydrogels can in general be categorized as negatively or positively thermosensitive, respectively. [82] Whereas the latter expands when the temperature exceeds their UCST, the negatively thermosensitive polymers shrink above their LCST temperature. [83] Gelatin is a prominent example of a hydrogel with a UCST that forms a gel upon cooling.

PNIPAM (reaction scheme shown in Figure 1.7) with its LCST has a negative temperature-dependence. Below 32 °C PNIPAM is in a hydrated, swollen state whereas above

that temperature, it collapses and releases water to result in a volume phase change transition. [82]

The thermoresponsive behavior originates from hydrophobic (shaded blue in Figure 1.7) and hydrophilic (shaded green in Figure 1.7) segments present in the hydrogel that are dominating at different temperatures. The free solution enthalpy ΔG can be used to explain the thermoresponsive behaviour via the Gibbs-Helmholtz equation, which connects the free enthalpy G, the enthalpy H and the entropy S. [88]

$$\Delta G = \Delta H - \Delta S \cdot T \qquad (1.2)$$

At temperatures below the lower critical solution temperature, ΔG is negative because the binding of water molecules to the amide groups by hydrogel bridge bonds leads to a strong reduction of the enthalpy H. This decrease of enthalpy exceeds the decrease of entropy S, which arises when a highly organised molecular layer is formed and thus, the hydrated, swollen state of the hydrogel is thermodynamically preferred. With increasing temperatures, the hydrogen bonds weaken and the hydrophobic interactions between the isopropyl groups become stronger. The exothermic enthalpy of the hydrogen bonds becomes dominated by the entropy term and at the critical transition temperature, ΔG becomes positive and entropy-driven phase separation occurs. Accordingly, interactions between the hydrophobic isopropyl groups become stronger than the interactions between water molecules and amide groups, which leads to water release from the hydrogel that collapses as the polymer chains aggregate. [89] The response temperature can be fine-tuned and altered by changing the ratio between hydrophilic and hydrophobic moieties, [83] e.g., an increase in the amount of hydrophobic segments lowers the LCST. [90] The response rate of PNIPAM to external thermal stimuli is relatively slow because the formation of impenetrable surface structures slows down the outward water flow. [82] By introducing pores and providing interconnected water release channels, the response rate can be increased. This includes the incorporation of pore forming additives during gel formation like poly(ethylene glycol) (PEG), [91] starch [92] or ethylene triethoxy silane [93] and the formation of macroporous structures with, e.g., freeze drying procedures. [94] Moreover, grafting side chains onto the network [95] or using micellar structures [96] can improve water in- and outtake properties. [94]

The thermoresponsive behavior of PNIPAM makes it a good actuator as reported by many scholars in this field, however most of them are not using pure PNIPAM due to limitations attributed to their fragility as well as the marginal response to external stimuli. [97] Lee *et al.* [98] showed a bilayer-type photoactuator consisting of PAM, PNIPAM with grafted side-chains and magnetic nanoparticles that when heated by absorbed visible light makes the actuator respond rapidly to light stimulation and also recovers quickly. Also, Peng *et al.* [99] demonstrated an actuator based on PNI-PAM/graphene oxide composite hydrogels that is deformable by local electrochemical
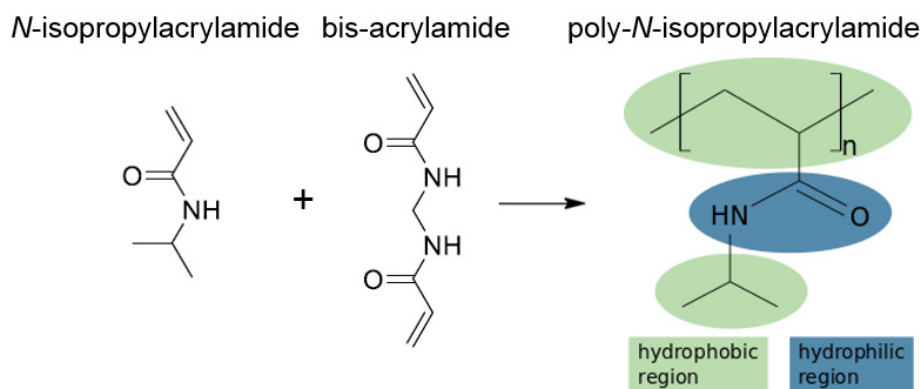
Figure 1.7. *Formation of poly-N-isopropylacrylamide (PNIPAM) by radical polymerization of N-isopropylacrylamide and N, N′-methylenebisacrylamide. The thermoresponsive behavior of PNIPAM originates from the hydrophilic (shaded in green) and hydropobic (shaded in blue) groups, which are dominating at different temperatures.*

reduction. Thus, most approaches chemically alter PNIPAM or use composite structures or nanoparticle filler materials, but this often comes with undesired changes in the hydrogel properties such as stiffness, optical transparency or a change in LCST. [97,100] PNIPAM is also used in cell sheet engineering where 2D cell films can be prepared and can then be potentially integrated into biohybrid devices. [13] Here, cells like cardiomyocytes are cultured on a PNIPAM layer for several days at 37 °C, the temperature at which PNIPAM is hydrophobic and thus promoting cell adhesion. As the temperature drops below the LCST, PNIPAM becomes hydrophilic and cells will then no longer be able to adhere, which leaves an intact cell sheet that can be separated and employed to power, e.g., a microspherical heart pump. [101]

1.2.4. Semisynthetic hydrogel: gelatin methacryloyl

Gelatin, a natural, thermoreversible hydrogel, is one of the most convenient proteins to use in tissue engineering for its biocompatibility, biodegradability and suitability for a wide range of cell types. [102] It is a denaturized form of collagen, which is the major constituent of skin, bone and connective tissue, with analogous bioactivity. It contains abundant cell binding sequences like RGD (a tripeptide sequence consisting of arginine, glycine and aspartic acid) and is therefore an important promoter of cell adhesion, proliferation and differentiation. [48, 103, 104] Gelatin also costs less than other natural materials and is relatively easy to obtain. [102] At body temperature, gelatin has low shape stability and shows rapid degradation [105], thus, scaffolds made from gelatin are not stable under cell culture conditions unless the gelatin is chemically modified such that amino groups are substituted with methacrylate groups to allow for

covalent crosslinking. By free radical polymerization, covalently crosslinked hydrogels are formed, which are stable at elevated temperatures and hence suitable to use in cell culture and as substrates for biohybrid robotics. [21] Additionally, the modification allows for gels stiffness adaption by changing the degree of crosslinking. Skeletal muscle C2C12 cells cultured on GelMA gels with a 1 to 3 kPa stiffness range showed enhanced differentiation with an increase in myotube number and formation rate. [106]

Commonly, GelMA is synthesized by the reaction of gelatin with methacrylic anhydride (MAA) in a carbonate-bicarbonate (CB) buffer at 50 °C for specific reaction times that determine the degree of substitution (DS). The MAA monomers react with the lysine and hydroxyl lysine groups in gelatin to form GelMA (Figure 1.8). The DS is better when the reaction solution pH is kept above the gelatin isoelectric point (normally 8-9 for gelatin type A) to ensure the neutrality of the lysine free amino groups and thus their reaction with MAA. [102]
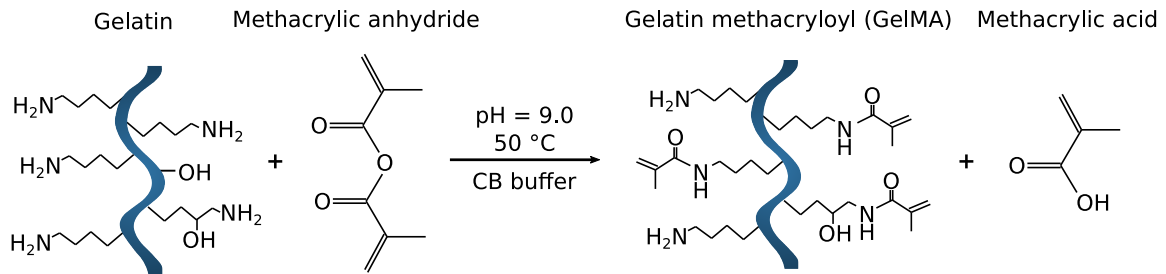
Figure 1.8. *Gelatin methacryloyl (GelMA) is synthesized by the reaction of gelatin with methacrylic anhydride in a carbonate-bicarbonate (CB) buffer at 50 °C for specific reaction times. Adapted from [102].*

1.2.5. Polydimethylsiloxane

The silicone polydimethylsiloxane (PDMS) is a widely used material in biophysical research and soft robotics due to its ease of (micro)fabrication, optical transparency, biocompatibility and molding properties. It also has tuneable mechanical properties [107] that make it an ideal material for use in microfluidics and organ-on-chip devices [108] or as a scaffold after 3D structuring using, e.g., direct laser writing. [109] PDMS is viscoelastic with a stiffness that can be easily tailored through varying the curing agent-to-base ratios as shown in Figure 1.9 a where the Young's moduli were determined in uniaxial compression tests to be in a range between 17 to 145 kPa.[2]

Moreover, PDMS biofunctionalization by coating is a straightforward process, which adds another valuable advantage as it is known to absorb small hydrophobic molecules like, for instance, proteins through physisorption. [108] An example is shown in Fig-

---

[2]Part of this work was published in Dörschmann, Böser, Isik, Arndt *et al.* [110]

ure 1.9 where cells from human retinal pigment epithelium (ARPE-19) were seeded on both uncoated and differently biofunctionalized PDMS substrates and then examined after two days with ARPE-19 cells showing good cell adhesion and proliferation on all coated surfaces that was analyzed in detail in Dörschmann *et al.* [110]
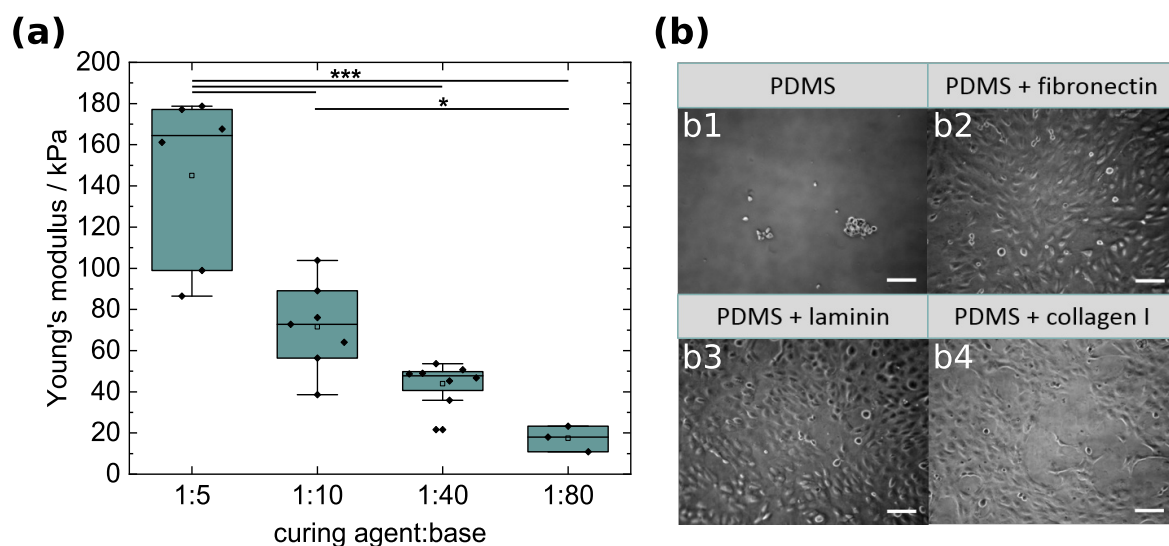
Figure 1.9. *a) Different ratios of curing agent and base in PDMS production lead to different Young's moduli. Values were determined by a uniaxial compression test with a strain rate of $5\,mm\,min^{-1}$ and Young's moduli values were determined by linear fitting of the obtained stress-strain curves. ANOVA one-way with post hoc Tukey test was used for statistical analysis. * $p < 0.5$, *** $p < 0.001$. b) ARPE-19 cells from human retinal pigment epithelium were grown on uncoated PDMS (b1) and PDMS substrates coated with b2) fibronectin, b3) laminin and b4) collagen I. Only cells on coated PDMS substrates show good adhesion and proliferation. Scale bars: $100\,\mu m$. (Own work)*

1.2.6. Mechanical characterization of soft substrates

As cells sense, interact and respond to changes in the underlying substrate through mechanosensing (cf. Section 1.1.5), understanding the physical and mechanical properties of soft substrates is a key factor for developing scaffold materials. The hydrogel mechanical behavior is time dependent when undergoing deformation, i.e., hydrogels show a viscoelastic behavior as they exhibit both elastic and viscous properties. The viscoelastic behavior is a result of the hydrogel's complex polymer network, which attributes to the elastic response, that comprises up to $98\,\%$ water that account for the viscous response to deformation. [73] Various techniques were established to study the mechanical behavior of biomaterials and the most commonly used ones (see Figure 1.10) that will be discussed briefly here are: Uniaxial cyclic compression tests, parallel-plate rheology, atomic force spectroscopy and microindentation.
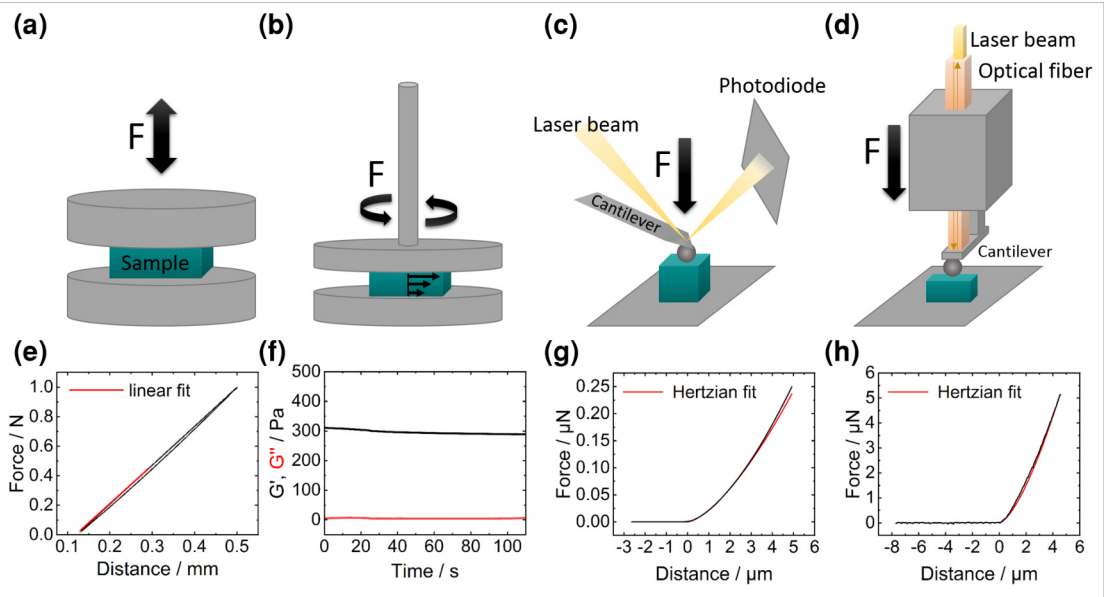
Figure 1.10. *a) - d) Schematic representation of different methods to determine Young's moduli of soft samples. a) Uniaxial cyclic compression tests, b) parallel-plate rheology, c) atomic force microscopy and d) microindentation. e) - h) Exemplary force-distance curves for each measurement methods. e) PDMS (1(curing agent):40(base)) was tested in a 2.5 kN Zwicki equipped with a 5 N force sensor employing a strain rate of 5 mm min^{-1}. A linear fit was used to determine the Young's modulus to be 26 kPa. f) Time sweep of a GelMA (97 % DS, 10 wt%, 0.1 % LAP, 1.5 mJ cm^{-2}) hydrogel tested in a Malvern Kinexus Pro rheometer. g) Force-distance curve recorded with an indentation speed of 10 µm s^{-1} with an applied Hertzian fit used for Young's modulus determination of a PNIPAM-GelMA composite tested with a CellHesion® 200 AFM (Bruker) equipped with a Bruker MLCT-O10 cantilever with an attached 22.82 µm diameter glass bead (SiN). The Young's modulus was determined to be 1.3 kPa. h) Force-distance curve with an applied Hertzian fit of GelMA (97 % DS, 10 wt%, 0.1 % LAP, 5.2 mJ cm^{-2}) tested with a microindenter (Pavone, Optics11; cantilever stiffness 4 N m^{-1}, bead diameter 23 µm, indentation speed 2 µm s^{-1}). The determined Young's modulus is 67 kPa. (Own work)*

A **compression or tensile test** is able to provide information about the overall bulk material properties but comes short at the cellular level. Although this test is easy and quick to perform, the sample is required to be in a certain size and shape that provides proper clamping particularly in a tensile test, which is challenging for very soft specimens. In a tensile or compression experiment, a force-distance curve is recorded while stretching or compressing the sample (Figure 1.10 a) and the stress σ and strain ϵ are calculated from the initial length l_0 and cross-sectional area A_0 perpendicular to the applied force:

$$\sigma = \frac{F}{A_0} \tag{1.3}$$

$$\epsilon = \frac{\Delta l}{l_0} = \frac{l - l_0}{l_0}. \tag{1.4}$$

The linear regime of a calculated stress-strain curve (Hooke's law) defines the elastic and reversible deformation during a uniaxial tensile or compression test, also known as Young's modulus: [77]

$$E = \frac{\sigma(\epsilon)}{\epsilon}. \tag{1.5}$$

Noticeably, Young's moduli obtained by tensile or compression tests of the same material can result in different values, thus a suitable choice of test must be made considering the material structure. [111]

Rheology is a quick and sensitive technique for analyzing viscoelastic material properties. It is based on applying oscillatory shear stresses onto a specimen and requires a perfectly flat sample surface to obtain reliable results (Figure 1.10 b). This test reports differences in degree of crosslinking, molecular weight or structural homo- or heterogeneity between hydrogels and, with a possibility to control the temperature, enables a study of transition states such as glass transition and melting temperatures. The complex shear modulus $G^*(\omega)$ can be determined by the sum of storage (G') and loss modulus (G''), which are the material elastic and viscous properties, respectively, as a function of angular frequency: [111]

$$G^*(\omega) = G'(\omega) + iG''(\omega). \tag{1.6}$$

The shear modulus G can be calculated from the shear stress τ and shear strain γ as follows:

$$G = \frac{\tau}{\gamma}. \tag{1.7}$$

The Young's modulus can then be determined using the calculated shear modulus G and the Poisson's ratio ν, the negative ratio of the transverse to axial strain, with the following equation: [76]

$$E = 2G(\nu + 1) \tag{1.8}$$

The Poisson's ratio for most hydrogels is between 0.45 and 0.5. [76] The viscosity η is defined as the shear stress τ divided by the shear rate $\dot{\gamma}$: [77]

$$\eta = \frac{\tau}{\dot{\gamma}}. \tag{1.9}$$

Both **atomic force microscopy (AFM) and microindentation** provide more accurate Young's modulus measurements at the cellular scale, which is advantageous for studying the local properties and thus the substrate heterogeneity. Using cantilevers as forces sensors, both techniques are non-destructive and can function on irregularly-shaped surfaces with the possibility to operate in liquid. In AFM, a cantilever with a small attached bead is pressed onto a fixed sample immersed in a liquid. A readout system consisting of a laser reflected from the cantilever end onto a photodiode measures the cantilever deflection due to bead interaction with the sample surface. [112] The microindenter used in this work has an analogues working principle to an AFM, however the readout technique consists of a fiber-optic based force sensor where the cantilever deflection is measured by interferometry. Here, the phase of the light is accurately measured so even the smallest cantilever displacement can thus be detected. The optical probe, which consists of the optical fiber, the cantilever and the spherical tip, is auto-aligned and pre-calibrated, thus makes calibration faster and easier than in AFM where beads have to be attached manually prior to measurement. In both methods, a sphere indents into a soft scaffold and the Young's modulus can then be calculated from the resulting force-distance curves. Contact mechanics need to be applied where the Hertz model is used when the indentation depths are small and a non-adhesive contact with no tension force within the contact area is assumed. For a spherical tip, the indentation force F is:

$$F = \frac{4\sqrt{R}}{3} \frac{E}{1 - \nu^2} d^{\frac{3}{2}} \tag{1.10}$$

with R as the indenter radius, E the Young's modulus, ν the Poisson's ratio and d the indentation depth. [113]

However, experimentally, small adhesive forces are always present, which makes the Hertz model applicable only when the loads are higher than the adhesive interactions. If the loads are small, the attractive interactions lead to the formation of a contact zone that is significantly larger than the one predicted by the Hertz model. [114] Ultimately, Young's moduli measurements using these techniques is conducted with strong assumptions about sample homogeneity and isotropy. This concern was addressed in a work performed in the group by Huth and Sindt *et al.* [112] who studied the influence of indentation depth on the Young's modulus value, however this topic is beyond the scope of this thesis.

2 | Microengineered functional hydrogels for biohybrid applications

In this chapter, I introduce a microengineering design for preparing functional hydrogels with electrical conductivity outclassing state of the art attempts using an extremely low filler concentration that imposes a negligible effect on the hydrogel matrix mechanical integrity as scaffolds for cell-based actuation.[1] First, I will present state of the art fabrication methods for conductive hydrogels. Afterwards, I will introduce the microengineering approach (Section 2.2) and the microstructural examination (Section 2.3) as well as the analysis of the conductive (Section 2.4) and mechanical properties (Section 2.5) of various composites of polyacrylamide and exfoliated graphene. The suitability of the microengineered conductive scaffolds for cell culture use is verified in Section 2.6 in addition to the analysis of gelatin methacrylate as a matrix material through biocompatibility tests and stiffness measurements as well as cell adhesion and beating behaviour evaluation of different contractile cell types namely skeletal muscle cells and cardiomyocytes. Moreover, the thermoresponsive hydrogel poly-N-isopropylacrylamide is introduced as an additional matrix material with a great potential for use in soft robotics (Section 2.7). In Section 2.8, the ability of fibroblasts to contract their environment and exert tensile forces is analyzed as possible candidates for actuators in biohybrid robots.

2.1. State of the art

Electrically conductive hydrogels are used in biosensors [1–4], bioelectronics [5–7], scaffolds for nervous [8, 9] or cardiac [10, 11] functional tissue [12], as well as biohybrid robotics [13] where cell contraction causes material actuation. Most of the cells suitable for biohybrid actuation can be electrically stimulated, thus sufficient conductivity of the material is essential to help spread the electrical signals efficiently. [13] Besides electrical conductivity, the material requirements in biohybrid actuators are manifold. For instance, the scaffold is required to be soft to allow robotic actuation yet

---

[1]Part of this work was published in Arndt *et al.*, Nano Letters, 2021. [115]

able to provide structural integrity to support the cells. Also, as cells demonstrate acute mechanosensitivity to their extracellular matrix, the scaffold material stiffness and the physicochemical properties of the matrix material are essential contributing factors. [13, 16]

Conductivity in hydrogels can be achieved by the addition of conductive filler materials in a hydrogel matrix by solution mixing, postpolymerization or *in situ* polymerization. [1, 19] The electrical conductivity in these composites prepared from conducting fillers and insulating polymer matrix is described and modeled by the percolation theory. The theory assumes a statistical filler material distribution and illustrates the dependence of electrical conductivity on filler concentration as shown schematically in a distinctive S-shaped plot (Figure 2.1) that can be divided into three characteristic regimes: (1) The filler is at a low concentration so that the composite is still insulating and no conductive pathways between the fillers are present. (2) With increasing filler content, the conductivity increases with a rapid upshift in conductivity at a particular point that marks the second regime and is denoted as the percolation threshold (V_t in Figure 2.1). Here, no connected network has developed yet but the conductivity is a result of tunneling that takes place between the fillers in close proximity. (3) At higher filler concentrations, the composite turns conductive, as a connected network of filler material has formed. [116]
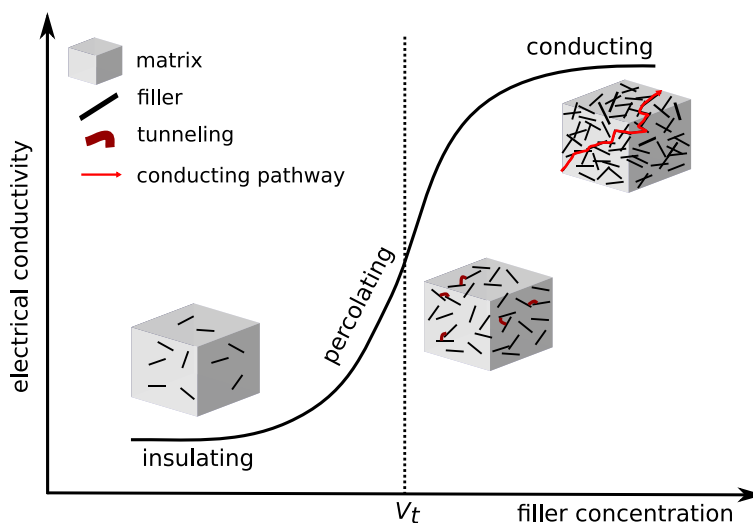
Figure 2.1. *The percolation graph with its three characteristic regimes is shown. With low filler contents, the material is insulating. The rapid change in electrical conductivity indicates the percolation threshold V_t. With high filler contents conducting pathways through the matrix are formed and the composite is conductive. Adapted from [116].*

The amount of filler material plays a crucial role as high filler amounts alter the matrix properties and often lead to matrix reinforcement and hence a change in mechanical properties. [20] To achieve a small percolation threshold filler materials with high aspect

ratios are advantageous and providing smaller volumes for equal filler amount or even predetermining conductive pathways lead to lower percolation thresholds as well.

The three main strategies to incorporate conductivity in hydrogels are solution mixing, *in situ* polymerization and postpolymerization and schematically shown in Figure 2.2. *In situ* polymerization is a one batch strategy to form conductive hydrogels in which the conductive polymer monomers or fillers are required to have compatible functional groups to react with the hydrogel matrix. This results in homogeneous and stable conductivities in the hydrogel, but requires additional processing steps. [19]
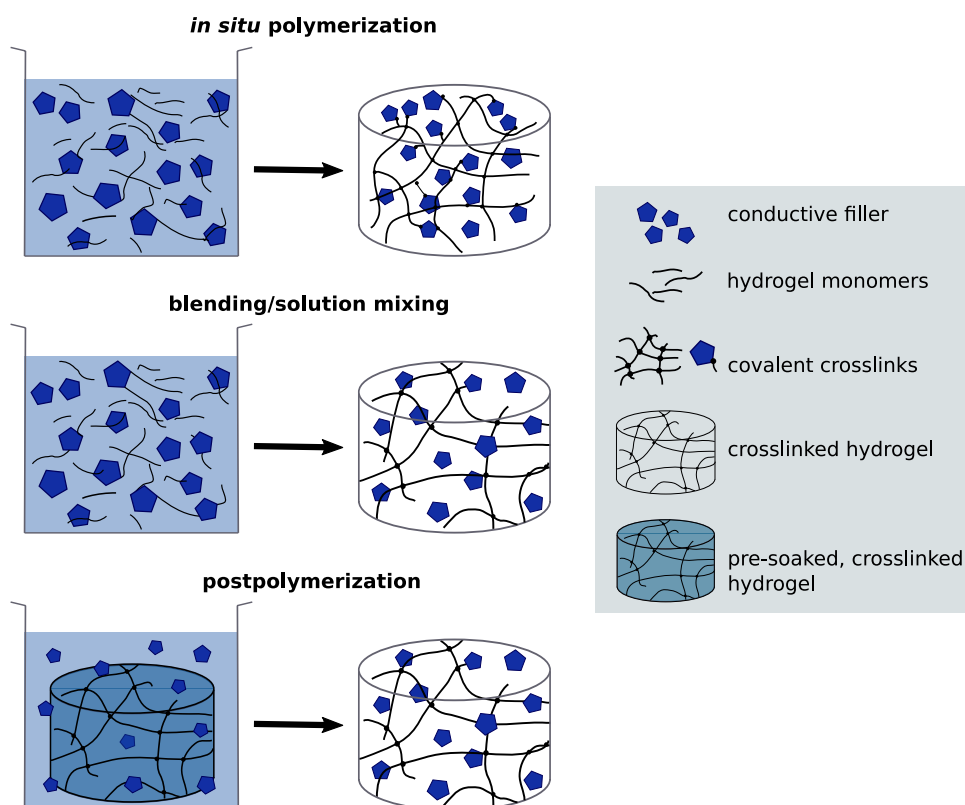
Figure 2.2. *Schematics of different strategies to prepare conductive hydrogels: in situ polymerization, postpolymerization and blending/solution mixing.*

In the postpolymerization approach, preformed hydrogels are immersed in, e.g., a monomer solution of a conductive polymer and the soaked hydrogels are subsequently placed in an oxidant solution to start polymerization where an interpenetrating network of conductive polymer is formed within the hydrogel. As coating procedures can be performed in a similar fashion, this techniques offers great versatility as hydrogels can be prefabricated in addition to the numerous conductive polymers that can be employed to introduce conductivity in subsequent steps. However, one aspect that should be taken into consideration is that the process relies on monomer or oxidant solution diffusibility into the bulk hydrogel so the conductivity is prone to be inhomo-

geneous. [1] A hydrogel example prepared with this method is GelMA soaked in an ammonium persulfate solution followed by incubation in an aniline solution to form a polyaniline-GelMA hydrogel with a $165.5\,\text{k}\Omega$ electrical resistance that was measured by two-point method. [1, 117]

Another method to prepare conductive hydrogels is through solution mixing where hydrogel precursor solutions are directly mixed with a conductive particle dispersion and a hydrogel forms after initializing the polymerization process. The conductivity is provided by virtue of conductive fillers percolating network formation. Prominent filler materials are either carbon-based materials such as carbon nanotubes, graphene and reduced graphene oxide or metal nanoparticles like gold nanorods and MXenes ($\text{Ti}_3\text{C}_2\text{T}_x$), or conductive polymers like polyanilin or PEDOT. [19, 118–120] Over the last decades, graphene has emerged as a very popular material for numerous applications because of its very high Young's modulus (1000 GPa) [121] as well as its high charge carrier density and mobility resulting in an outstanding electrical conductivity of up to $6 \cdot 10^5\,\text{S}\,\text{m}^{-1}$. [116, 122] Graphene is a two-dimensional, carbon-based material with a hexagonal honeycomb structure that consist of sp^2-hybridized carbon atoms. [122] It is transparent when sufficiently thin as a single layer only absorbs $2.3\,\%$ of incident white light, which makes it relevant in hydrogel applications where they are required to be optically transparent. [123] Graphene has been widely used for generating conductive, biocompatible hydrogels for tissue engineering [3], bioelectronics [4] or in biohybrid applications. [21]

One of the shortcomings in directly mixing conductive filler materials is that a large amount of filler material is required to reach the percolation threshold, which in turn increases the chance of filler material aggregation that hinders a homogeneous distribution within the polymeric network and thus results in a lower electrical conductivity. [124] Furthermore, it results in hydrogel matrix stiffening due to the extensive use of filler material, the amount of which is a critical aspect. [20] The main challenge when preparing conductive hydrogels is to maintain the physicochemical properties of the hydrogel matrix such as toughness, stretchability and sustaining multiple cyclic compression.

In this part of my thesis, I employed a novel micro-engineering approach to create a conductive hydrogel with extremely low filler concentration while maintaining the original matrix properties. This was carried out using a sacrificial interconnected zinc oxide network coated with a dispersion of exfoliated graphene flakes which results in a microengineered graphene framework structure that establishes conductive pathways within the hydrogel matrix and thus promotes electrical conductivity. The template dissolution in the hydrogel matrix creates an interconnected system comprising microchannels with channel walls coated with the conductive filler material similar to nerves in the body. By restricting the conductive pathways to the microchannel walls, $99.9\,\%$ [125] of the hydrogel matrix remains filler-free and thus mechanically unaltered in striking contrast to previously published attempts.

2.2. Microengineered conductive hydrogel preparation

The conductive hydrogels were prepared using a template-assisted approach that is schematically shown in Figure 2.3. The sacrificial template was made from tetrapodal zinc oxide microparticles (t-ZnO), which were fabricated with the so-called flame transport synthesis. [126, 127] The latter was conducted as follows: Zinc oxide powder with 1 µm to 5 µm grain size was mixed with poly(vinyl butyral) using a mass ratio of 1:2 and the mixture was heated to 900 °C in a furnace with a 60 °C min^{-1} heating rate for 30 min and the t-ZnO microparticles powder was subsequently harvested.

In the first template preparation step, a defined amount of loose t-ZnO powder was pressed into a template with a defined density (here: 0.3 g cm^{-3}) by using a rigid mold with a specific geometry (here: 6 mm height, 6 mm diameter). This was followed by an annealing step at 1150 °C for 5 hours. The tetrapodal structure and the sintering step resulted in a template with an interconnected arm structure with a high control over porosity (up to 94.7 %), pore-size and geometry. The template and a t-ZnO arm cross-section are schematically shown in Figure 2.3 a. The ZnO template has open pores in the micrometer regime that generates large capillary forces upon contact with aqueous dispersions. In addition with the hydrophilic nature of ZnO surfaces, the template structure thus enables a homogeneous nanomaterial coating upon infiltration with aqueous 2D nanoparticle dispersions using a drop-casting process [128] as shown schematically in Figure 2.3 b, f. Droplets of nanoparticle suspension were gently dropped on ZnO tetrapods until the template is fully soaked and then the water was left to evaporate in a 4-hour drying step at 50 °C. The nanoparticles form a homogeneous layer on the ZnO surface and the layer thickness can be adjusted to up to 10 nm by either adjusting the concentration of the dispersion or tailoring the infiltration frequency. [125] In this work, I employed exfoliated graphene[2] (EG) for its higher conductivity and superior mechanical properties when incorporated in hydrogel matrices in comparison to other commonly used nanomaterial suspensions such as CNTs. This coated template is highly porous with a free volume of approximately 94 %[3] that was subsequently filled completely with a hydrogel precursor solution of polyacrylamide (PAM), shown schematically in Figure 2.3 c. The hydrogel precursor was prepared by mixing acrylamide (Bio-Rad, 40 %, 1250 µL), N, N'-methylenebis(acrylamide) (Bio-Rad, 2 %, 1000 µL), HEPES buffer (Sigma-Aldrich, pH 7.5, 50 µL), 2625 µL ddH$_2$O and ammonium persulfate (APS, Sigma-Aldrich, 10%, aq., 75 µL) and degassing the mixture in a

---

[2]EG dispersion (1.7 or 1.9 mg ml^{-1}) was kindly provided by Sixonia Tech GmbH, Dresden and used without further purification.

[3]The porosity is calculated as follows: a defined amount of ZnO powder (here: 0.051 g) is pressed into a specific shape (here: cylindrical, diameter and height: 6 mm), which equals a volume of approximately 0.170 cm^3 at a density of 0.3 g cm^{-3}. The bulk density of ZnO is 5.61 g cm^{-3} and thus the porosity is ∼94 %.
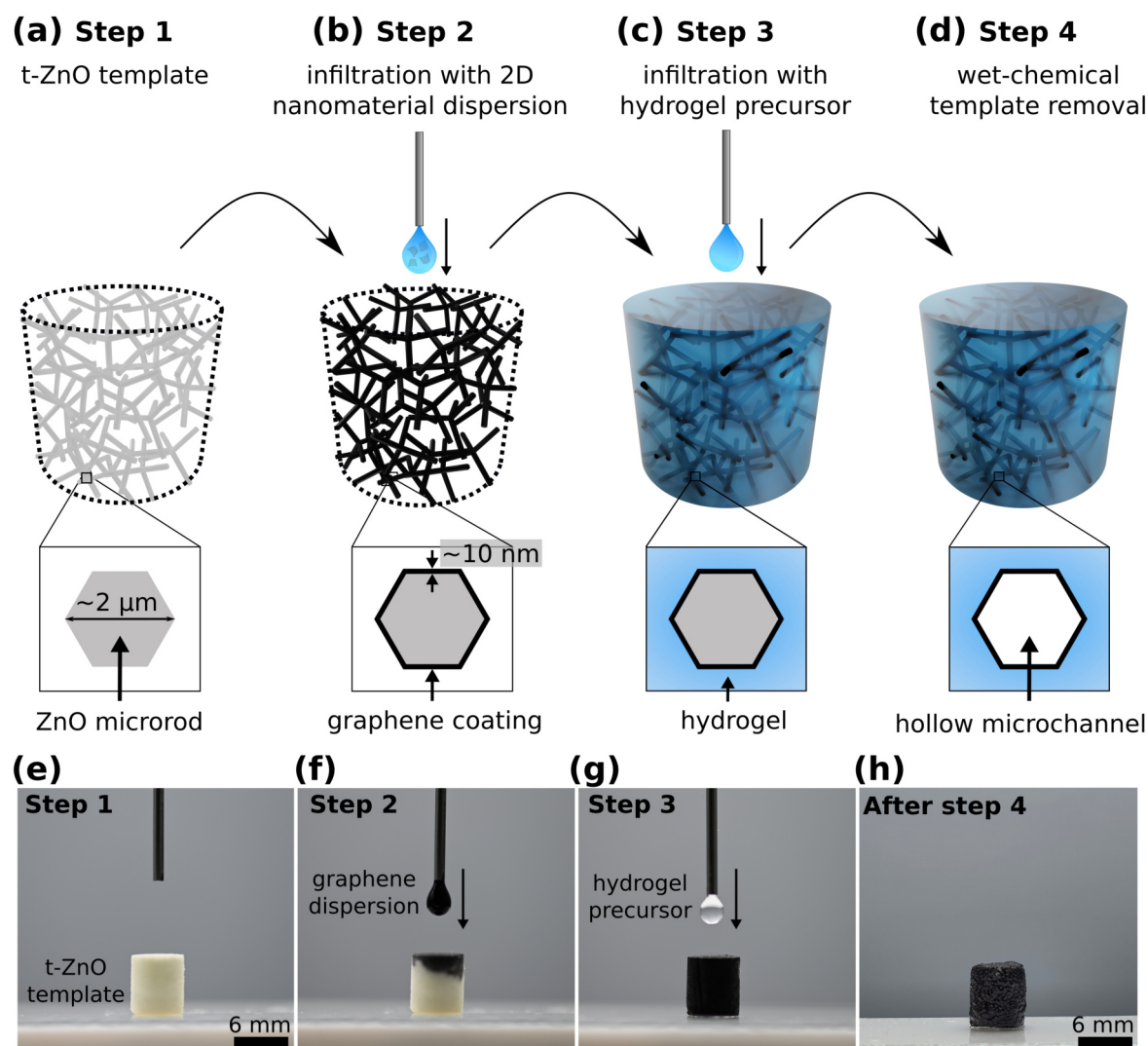
Figure 2.3. *Fabrication route of conductive microchannel-containing hydrogels. a-d) Schematic illustration of the preparation steps for a 3D network composite consisting of a hydrogel matrix and microchannels coated with exfoliated graphene. e-h) Images for the individual infiltration processes: e) t-ZnO template before infiltration, f) drop-casting process with 2D filler material (Step 2), g) after complete infiltration, the hydrogel precursor solution is drop-cast on the template until completely filled (Step 3), h) polyacrylamide-exfoliated graphene (PAM-EG) composite (EG: 0.32 vol%). Reprinted with permission. [115] Copyright 2021, American Chemical Society.*

desiccator for at least 10 minutes. Afterwards, N, N, N', N'-tetramethylethylenediamine (TEMED, Sigma-Aldrich, 10 %, 100 µL) was added and the hydrogel precursor solution was drop-cast onto the t-ZnO templates until their entire free volume was filled. The hydrogel was then left to polymerize for 90 minutes. Subsequently, the ZnO template was removed by wet-chemical treatment with hydrochloric acid (HCl, 0.5 mol L^{-1}) (Figure 2.3 d) and the scaffolds were washed extensively with double distilled water prior to use to remove the acid and unreacted by-products.

The process eventually resulted in a scaffold from PAM pervaded with hollow microchannels where the channel surfaces are covered with graphene as illustrated in the process sequence in Figure 2.3 e-f. The bonding between EG and PAM is based on structural attachment and van der Waals forces rather than covalent bonds as confirmed by Raman spectroscopy.[4] Figure 2.4 shows the Raman spectra of network PAM and a PAM-EG sample with 0.16 vol% EG. The conductive hydrogel reveals additional bands at $\sim 1350\,cm^{-1}$, $\sim 1580\,cm^{-1}$ and $\sim 2700\,cm^{-1}$, which correspond to the D, G and 2D band of graphene, respectively. [125] No further bands are shown, which indicates an absence of covalent bonds and bonding based on structural attachment and van der Waals forces.
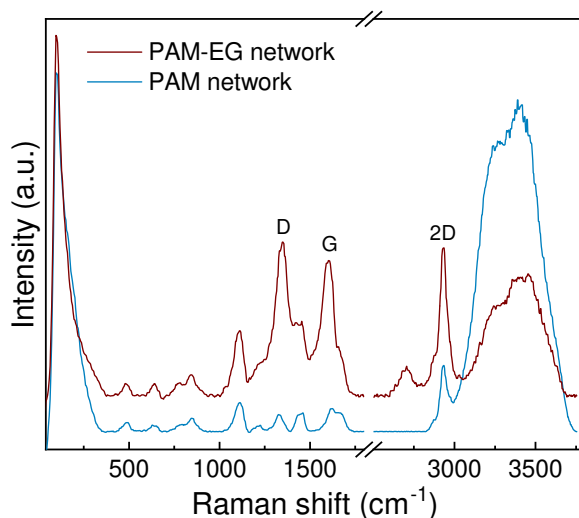
Figure 2.4. *Raman spectra of network PAM and PAM-EG samples. Additional bands at $\sim 1350\,cm^{-1}$, $\sim 1580\,cm^{-1}$ and $\sim 2700\,cm^{-1}$ corresponding to the D, G and 2D band of graphene are visible for the PAM-EG sample. Reprinted with permission. [115] Copyright 2021, American Chemical Society.*

---

[4]Raman spectroscopy was kindly performed by M. Hauck and Dr. F. Rasch, CAU Kiel on a *alpha300 RA* (WITec) microscope with a triple grating spectrometer (600 g mm^{-1}) and a charge-coupled device detector. The excitation wavelength of the laser was 532.2 nm, the spot size on the sample was 1.41 µm and the maximum power was 52 mW.

As the use of microengineered scaffolds is intended for *in vitro* applications, their biocompatibility was determined using an indirect MTT extraction test performed according to ISO-10993[5] using rat embryonic fibroblasts (REF52 wt) as a model system and culture medium as a control (Figure 2.5). In an MTT assay, methylthiazolyldiphenyl-tetrazolium bromide (MTT) is converted into a purple-colored crystalline formazan product by viable cells with active metabolism. Since dead cells are unable to convert the dye, the color formation can be assumed to be directly proportional to the number of viable cells. [129] The network PAM samples demonstrated higher biocompatibility than 90 % for undiluted extracts. A diminished fibroblast proliferation transpired when cells were exposed to extracts of PAM-EG samples, yet still with biocompatibility values above 70 % for undiluted extracts, which the ISO norm regard as biocompatible.

This microengineering approach is very versatile and can be adapted to different matrix materials and nanoparticle dispersions. Besides PAM, other matrix materials like gelatin methacryloyl (GelMA) and mixtures of PAM and GelMA (cf. Section 2.6) as well as the thermoresponsive hydrogel poly-*N*-isopropylacrylamide (PNIPAM, cf. Section 2.7) were also analyzed in this work as suitable scaffold matrices in cell culture.
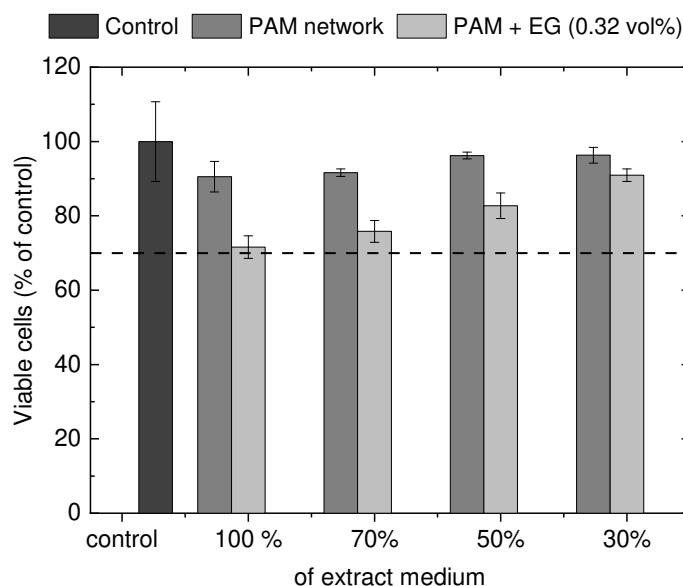
Figure 2.5. *Cell viability of rat embryonic fibroblasts (REF52 wt) exposed to medium extracts of network PAM and microchannel-containing PAM with 0.32 vol% EG determined with an indirect MTT extraction assay. Error bars depict standard deviations, N = 3. Dashed line marks a cell viability of 70 %. Reprinted with permission. [115] Copyright 2021, American Chemical Society.*

---

[5]Experimental details are provided in Appendix A.3.

2.3. Microstructural analysis

The microstructure of the conductive hydrogel scaffolds was analyzed by scanning electron microscopy (SEM) and X-ray microtomography (micro-CT). SEM images of t-ZnO and graphene coated t-ZnO were kindly provided by Dr. Florian Rasch from the group of Prof. Rainer Adelung at Kiel University. Figure 2.6 shows SEM images for the different stages of the conductive microchannel-containing hydrogel fabrication. The tetrapodal ZnO template structure is shown before (Figure 2.6 a) and after coating with EG (Figure 2.6 b) with the insets showing macroscopic images of the respective samples. The figure demonstrates that the drop-casting process generated a uniform coating of ZnO with EG.
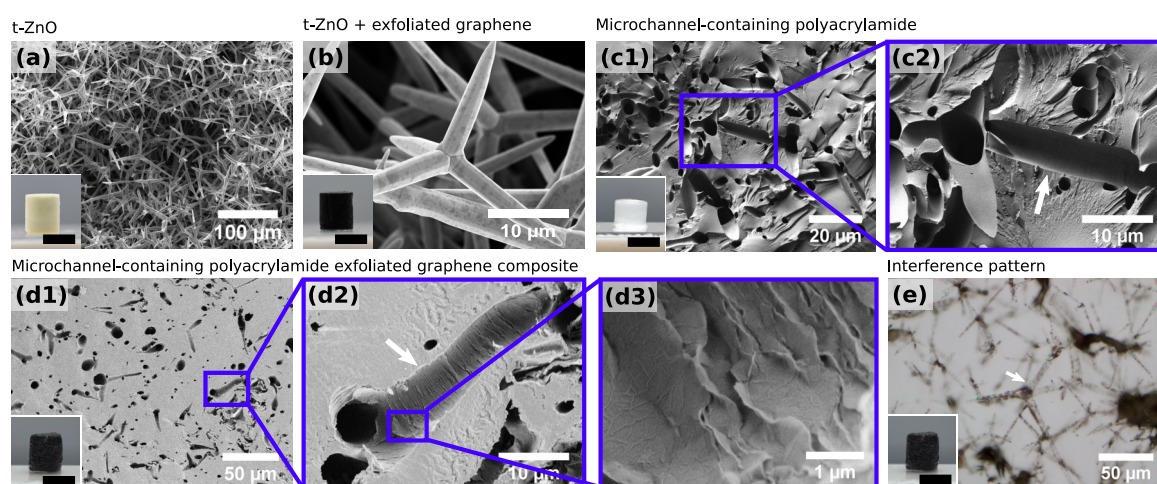
Figure 2.6. *Representative microstructure scanning electron micrographs of a) a t-ZnO template, b) t-ZnO template coated with exfoliated graphene, c) microchannel-containing polyacrylamide (network PAM) and d) microchannel-containing polyacrylamide-exfoliated graphene (PAM-EG) composites. The white arrows in c) and d) mark a channel cut in half. The channel surfaces in network PAM are smooth while the PAM-EG composite channels are uneven and rippled, which indicates EG coverage. The characteristic wrinkled structure of multilayered graphene is visible in high magnification (d3). e) A thin layer of PAM-EG composite on a SiO$_2$ wafer imaged with light microscopy shows interference pattern (arrow) of multi-layered graphene assembled on tetrapod arms. Scale bar insets: 6 mm. Adapted with permission. [115] Copyright 2021, American Chemical Society.*

SEM analysis of the hydrogel samples has been kindly performed by Dr. Irene Wacker in the group of Prof. Rasmus R. Schröder at the Center of Advanced Materials (CAM) at Heidelberg University. The SEM analysis of highly hydrated biomaterials was challenging as the water removal from specimen is required prior to placing it in high vacuum chambers. Freezing the samples by conventional methods like "flash freezing" in liquid nitrogen followed by lyophilization [130] may not lead to accurate ultrastructural features while other techniques like high-pressure freezing are limited to small

sample sizes. [131] The ice crystal formation upon freezing the hydrogels is in particular problematic due to formed artifacts that subvert the outcome. Hence, a quantitative assessment of the swollen hydrogel channel size is not possible via SEM analysis but the channel structure as well as the homogeneity of the graphene coating on the channel surface can be studied. The scaffolds were dehydrated with a series of steps using graded ethanol with a final exchange to acetone followed by air drying and cutting in an ultramicrotome.

Figure 2.6 c and d show a microchannel-containing polyacrylamide hydrogel (network PAM) and a polyacrylamide-exfoliated graphene composite (PAM-EG) with conductive microchannels, respectively, where the tetrapodal structure that originates from the sacrificial ZnO template is clearly visible. The arrows in Figure 2.6 c, d indicate a microchannel that has been halved. The figure demonstrates a significant difference between microchannel-containing PAM and PAM-EG samples in the topography of the channel surfaces. While the channel surface of the network PAM seems very smooth, it appears uneven and rippled in PAM-EG. Especially in Figure 2.6 d3, the characteristic wrinkled structure of multi-layered graphene [132, 133] is distinctive. The images evidently illustrate that graphene is only present inside the channels on the channel walls and did not diffuse into the hydrogel matrix. To confirm that multi-layered graphene was present, a dehydrated PAM-EG sample was cut with an ultramicrotome, mounted on a Si-wafer and was visually inspected with a light microscope in epi-illumination mode (Figure 2.6 e) as multilayered graphene shows interference pattern on SiO_2 due to strong scattering centers. [134] The arrow indicates one example of the visible interference pattern on a tetrapod arm.

The interconnectivity of the channels and the network was analyzed with micro-CT and the imaging and analysis were kindly performed by Dr. Berit Zeller-Plumhoff at the P05 microtomography beamline operated by the *Helmholtz-Zentrum Geesthacht* at the PETRA III storage ring at *Deutsches Elektronen-Synchrotron* (DESY), Hamburg. Details about the analysis can be found in [115]. In Figure 2.7, rendered micro-CT 3D images of a t-ZnO-EG and a network PAM scaffold are shown, where similar colors designate connected networks. The t-ZnO scaffold coated with EG has a calculated connectivity of 97.1 % compared to the 70.6 % in the network PAM sample. As the latter contains water, it is more prone to movement during the measurement as the beam scans the sample that results in image artefacts and lower contrast, both of which impact the calculated connectivity. The decrease of about 30 % in connectivity can be attributed to the hydrogel system itself as it swells and eventually leads to a destruction of the original connections and conductive pathways. In Figure 2.7 b the ROI used for the PAM network analysis has a dimension of $1.6 \times 1.2 \times 0.36 \, mm^3$ and one connected component (purple color) extends over the entire samples.

MicroCT: t-ZnO + exfoliated graphene

MicroCT: microchannel-containing polyacrylamide

(a)

(b)

1 mm

1 mm
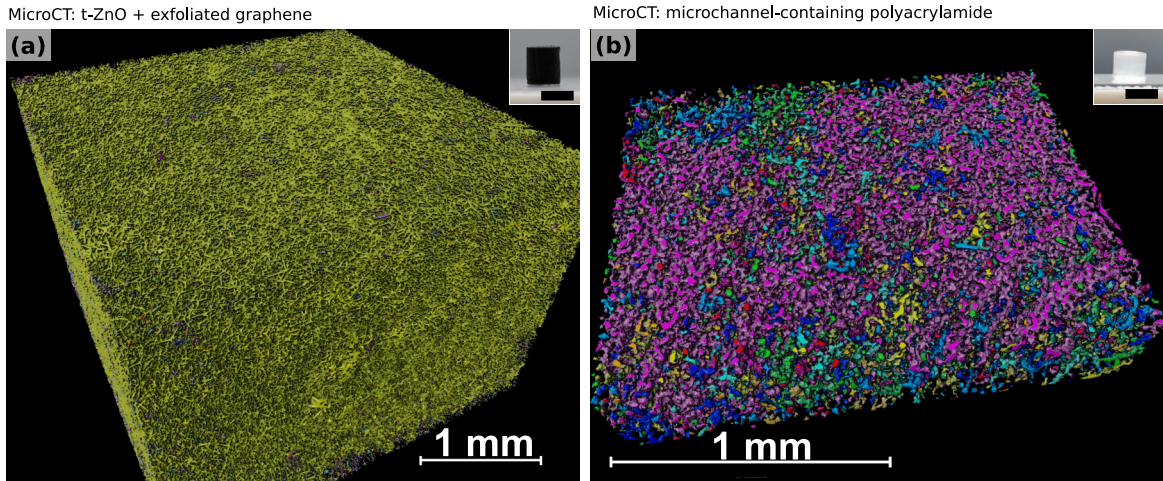
Figure 2.7. *Rendered X-ray microtomographies of a) t-ZnO-EG and b) network PAM. Connected components are denoted with the same colors. Scale bar insets: 6 mm. Adapted with permission. [115] Copyright 2021, American Chemical Society.*

2.4. Conductive properties

As the DC conductivity of heart muscle tissue is $0.1\,\mathrm{S\,m^{-1}}$ [48], the use of cardiomyocytes in biohybrid applications necessitates the employment of scaffolds with even higher conductivity than the tissue so that cell-to-cell signals can be transmitted via the scaffold. To examine the scaffolds electrical properties, the conductivity was analyzed using a two-wire sensing method with the setup shown in Figure 2.9 a. Prior to infiltrating it with the hydrogel solution, the template was mounted between two brass plates using silver paste to ensure a good electrical contact and the measurement on triplicates of samples were conducted in double distilled water. The double distilled water has a negligible ionic conductivity and thus no impact on the conductivity measurement. The microchannel-containing samples were measured in water firstly to prevent the composites from drying during the measurement and secondly because they should be later used in aqueous environments. The current was measured while the voltage was increased from -1 V to +1 V in 0.05 V step sizes.[6] All samples showed a linear relationship between current and voltage (Figure 2.8) thus Ohm's law (Equation (2.1))

$$R = \frac{V}{I} \tag{2.1}$$

can be applied to calculate the specific resistivity ρ:

---

[6] The current-voltage curves were recorded using a Keithley 2400 sourcemeter and a customized *LabView* program developed in the group of Prof. R. Adelung, CAU Kiel.

$$\rho = R \cdot \frac{w \cdot h}{l} = R \cdot \frac{q}{l} \qquad (2.2)$$

with R being the resistance and l, w, h being the length, width and height of the sample, respectively. q thus equals the cross section of the sample.

The specific electrical conductivity σ is the inverse of the specific electrical resistance:

$$\sigma = \frac{1}{\rho}. \qquad (2.3)$$

The specific electrical resistance is calculated using the cross section of the whole template including the hydrogel cross sections, conductive filler material and incorporated water. Due to the high resistivities of polyacrylamide and water in comparison to the conductive filler, the conductivity can here be attributed to the latter.
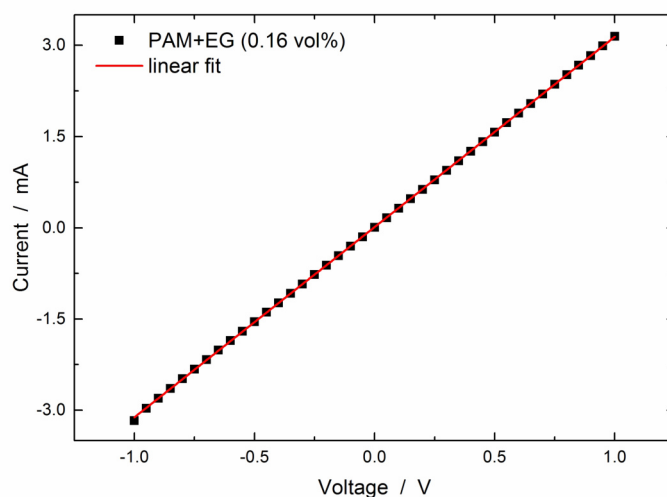
Figure 2.8. *Exemplary current vs. voltage curve of PAM-EG (0.16 vol%). The measured current was plotted as a function of the applied voltage. The sample shows ohmic behavior and the specific conductivity was obtained from the linear fit (red). Reprinted with permission. [115] Copyright 2021, American Chemical Society.*

In Figure 2.9 b, the specific electrical conductivity is illustrated as a function of filler concentration and the network PAM samples show a conductivity of $0.006\,\mathrm{S\,m^{-1}}$ (red dashed line). An increase of filler material from 0.04 to $0.32\,\mathrm{vol\%}$ leads to an increase in specific conductivity by more than three orders of magnitude, which indicates the presence of percolating pathways consisting of graphene. In general, electrical signals

can be transmitted by either tunneling or direct contact between graphene flakes. [116] Thus, the higher conductivity can be explained by the formation of more direct contacts when more exfoliated graphene is added to the system. Using a filler fraction of only $0.04 \, \text{vol}\%$ EG, an increase of 50% in conductivity compared to pure network PAM samples was achieved while a $0.32 \, \text{vol}\%$ filler fraction increased the conductivity from $0.012 \, \text{S} \, \text{m}^{-1}$ for the lowest tested filler amount to $1.8 \, \text{S} \, \text{m}^{-1}$.

Figure 2.9 c shows a comparison of the conductivity values achieved with this new microengineering method with state of the art approaches to generate conductive hydrogels. Remarkably, the method requires more than one order of magnitude less amount of filler material yet still delivers better electrical properties than previously reported values with a conductivity that exceeds the $0.1 \, \text{S} \, \text{m}^{-1}$ in heart tissue. This shows that pervading the material with conductive pathways similar to an artificial nervous network is a very efficient way to achieve high conductivities at very low filler concentrations. With a potential use in, e.g., 3D cell culture or biohybrid robotics applications, it is important that the material properties remain stable over extended time periods. Figure 2.9 d shows the conductivity values normalized to the starting conductivity measured over a time period of 12 days for a PAM-EG composites with $0.32 \, \text{vol}\%$ EG. After nine days, the conductivity remains on a stable level but decreased by 31% compared to the conductivity measured on day one, which is presumably due to a perpetual hydrogel swelling and EG redispersion in water. A Raman spectroscopy investigation (see Section 2.3) showed that EG is not covalently bound to the PAM but rather linked via Van der Waals forces, structural attachment or electrostatic interactions which are ill-suited for keeping the integrity of the conductive pathways up to a certain point that eventually leads to deterioration of electrical conductivity. The decrease in conductivity ceased after nine days.

Resistance measurements during cyclic compressions are shown in Figure 2.9 e. A PAM-EG ($0.32 \, \text{vol}\%$) composite was compressed by 35% for 15 consecutive cycles while current vs. voltage curves were recorded in a customized micromanipulator setup.[7] The samples were compressed in water and fixed with silver paste in the setup prior to measurement to ensure a good electrical contact. The normalized change in resistance $\Delta R/R$ was calculated with

$$\frac{\Delta R}{R} = \frac{R_0 - R}{R_0} \tag{2.4}$$

with R_0 as the initial measured resistance and is depicted in dependence of the compressive strain up to 35%. The change in resistance increases upon compression, which implies that more conductive pathways are formed.

---

[7]Micromanipulator setup was developed in the group of Prof. R. Adelung, CAU Kiel. The current-voltage curves were recorded using a Keithley 2400 sourcemeter and a customized *LabView* program.
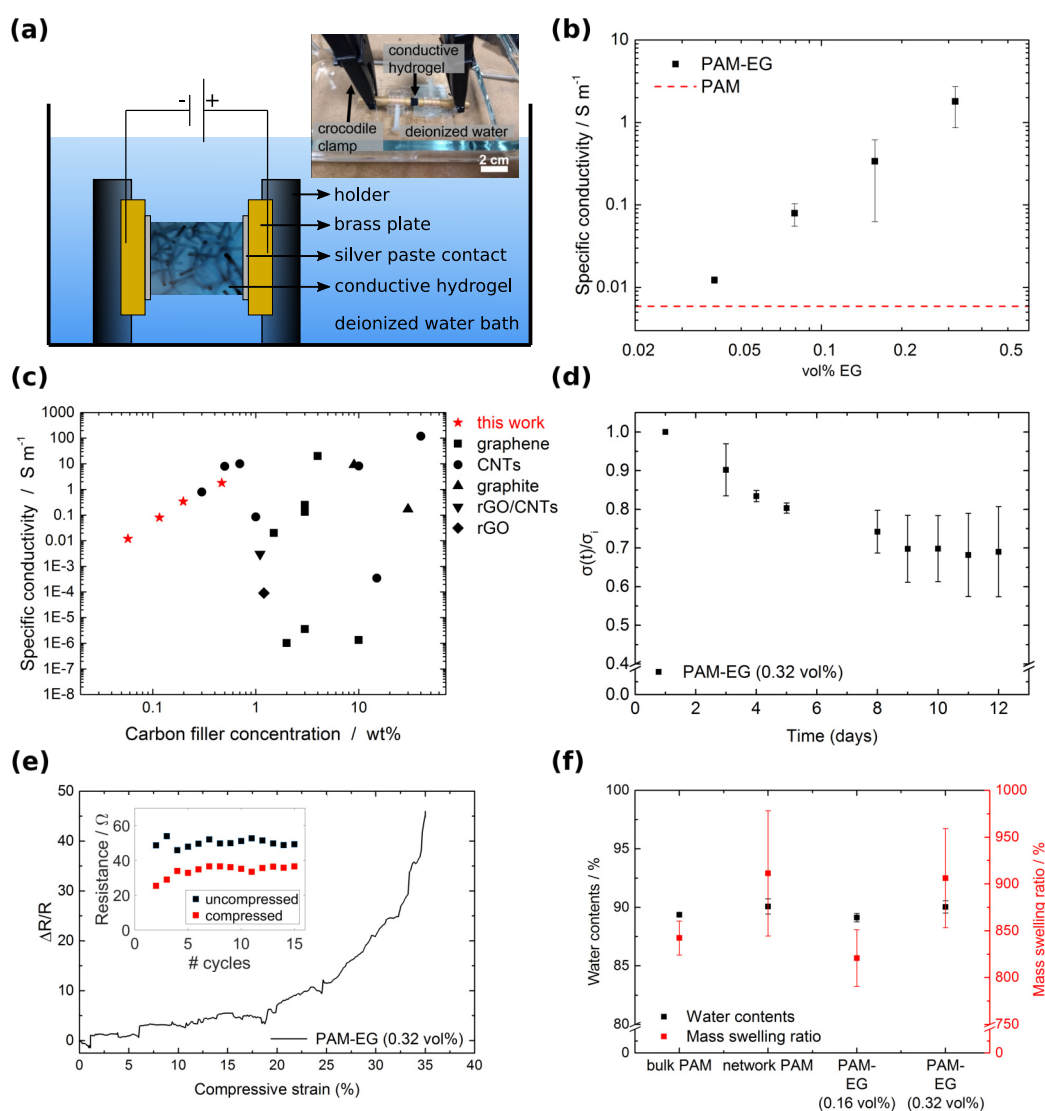
Figure 2.9. *Electrical properties of microchannel-containing conductive hydrogel composites. a) Image and schematic illustration of the electrical conductivity measurement setup in water. The samples are fixed to brass plates using silver paste in a customized sample holder. b) Specific electrical conductivity as a function of filler concentration. Error bars depict standard deviation, N = 3. c) Comparison of the specific electrical conductivity of conductive hydrogels prepared using carbon-based filler materials. The red stars signify the results from microengineered PAM-EG composites. In Table B.2 in Appendix B.6, the list of conductive hydrogels with information and references is available. d) Conductivity of PAM-EG composites with 0.32 vol% EG was measured over a 12 days period. The normalized conductivity ($\sigma(t)/\sigma_0$) is displayed as a function of time. Error bars depict standard deviation, N = 3. e) Normalized change in resistance ($\Delta R/R$) during cyclic compression up to 35 % compressive strain. The inset shows the resistance values of compressed and uncompressed states for 15 consecutive cycles. f) Water content and mass swelling ratio of different sample types. Reprinted with permission. [115] Copyright 2021, American Chemical Society.*

The inset in Figure 2.9 e shows electrical resistance values for the compressed and uncompressed state during 15 consecutive cycles. After the first compression cycle, the resistance value of the uncompressed state increased by approximately 30 % but remained unchanged in the subsequent cycles. The increase in resistivity after the first cycle is likely due to a partial destruction of conductive pathways, e.g., by the rearrangement of graphene sheets as a result of the compression.

In Figure 2.9 f, the results of swelling tests are shown. Swelling tests are used to obtain information about water content and the mass swelling ratio of hydrogel samples. Therefore, the samples are weighed in their hydrated and dried state. The initial weight (W_i) is determined by blotting hydrated samples with paper to remove excess water and weighing them. Afterwards, the samples are dried in an oven at 50 °C until there is no further change in weight (W_d).

The water content W_c is determined with

$$W_c = \frac{(W_i - W_d)}{W_i} \cdot 100 \,\%\tag{2.5}$$

and the mass swelling ratio (W_m) is calculated with

$$W_m = \frac{(W_i - W_d)}{W_d} \cdot 100 \,\%.\tag{2.6}$$

All sample types have a high water content of approximately 90 % and a mass swelling ratio of around 870 %, which further shows that the influence of the filler material on the matrix properties is negligible.

2.5. Mechanical properties

Scaffolds in contractile cells and biohybrid applications need to withstand several hundreds of contraction cycles and thus the material is required to be flexible enough to recover after deformation, to be within a suitable stiffness range to provide optimum cell proliferation and cellular functions and to be soft enough for cells to deform the material. To visualize the compression at a macroscopic scale, a microchannel-containing PAM-EG hydrogel with 0.32 vol% EG was compressed multiple times and the image sequence of deformation is demonstrated in Figure 2.10. As seen in the figure, the sample immediately recovered its original shape and dimensions after approximately 25 % deformation.

In order to analyze the mechanical properties of the samples in more detail, cyclic compression tests on a *ZwickRoell 2.5 kN Zwicki* equipped with a *Xforce P* 5 N force sensor were performed. The samples were compressed in water to avoid drying them
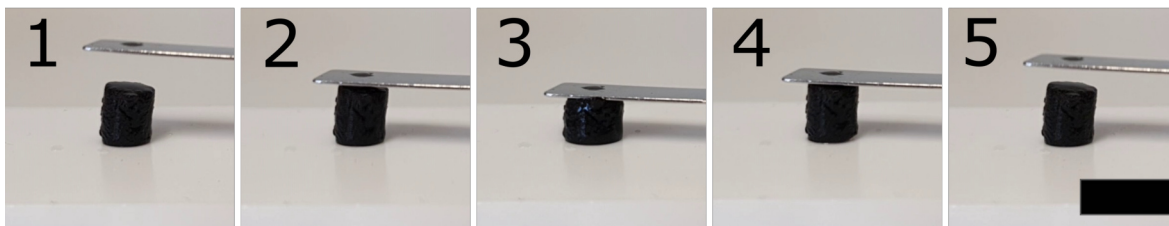
Figure 2.10. *Image sequence for macroscopic deformation of a microchannel-containing PAM-EG composite (0.32 vol% EG). The sample instantly recovers shape after deformation of around 25 % upon force removal. Scale bar: 10 mm.*

during the experiment and to avoid matrix alterations when water is squeezed out during compression. Samples from bulk polyacrylamide, microchannel-containing PAM without graphene (network PAM) and microchannel-containing PAM with 0.16 and 0.32 vol% EG were compressed by 33 % with a speed of 10 mm min^{-1} for 100 consecutive cycles and a pre-load of 30 mN. From the recorded force-distance curves, stress σ and strain ϵ were calculated using the initial length l_0 and cross section A_0 of the sample according to equation Equation (1.3) and Equation (1.4).

Representative stress-strain curves of each sample type are shown in the left column of Figure 2.11 a, c, e, g. All samples show a viscoelastic behaviour, which is attributed to the viscoelastic properties of the hydrogel matrix. PAM-EG composites also show a distinctive hysteresis to the initial cycle which is likely due to graphene flakes re-arrangement that transpires during the first compression cycle. Moreover, material interaction and breaking of Van der Waals forces might take place as the material is adapting to the applied force in a phenomenon known as *preconditioning.* [135] In all subsequent cycles, the stress-strain curves show no further significant change, thus after the initial cycle and the material's adaption to force, the system is in an equilibrium state.

The Young's modulus E is defined as the elastic, reversible deformation during a tensile or compression test and is the initial slope in the stress-strain curves. Thus, the Young's modulus was calculated by linear fitting the initial slope up to a specific compression strain mark for all 100 cycles and taking the mean values. Representative linear fits up to a strain rate of 10 % are shown in Figure 2.11 b, d, f, h. For most applications of conductive hydrogels such as biohybrid robotics, a strain rate of 5 % is sufficient, thus the Young's moduli were determined from the linear fit up to a 5 % strain rate. After 100 cycles with 33 % compression, the samples showed a slight reduction in height as shown in Figure 2.12 where the relative recovery in % as a function of the cycle number for every sample type is given. During the first few cycles the samples deform but, as the material adapts to the applied force, the deformation remains unchanged at a level higher than 94 % for all sample types, which implies a very good mechanical stability. Bulk PAM showed the least deformation after 100 cycles with ~97.7 % recovered height
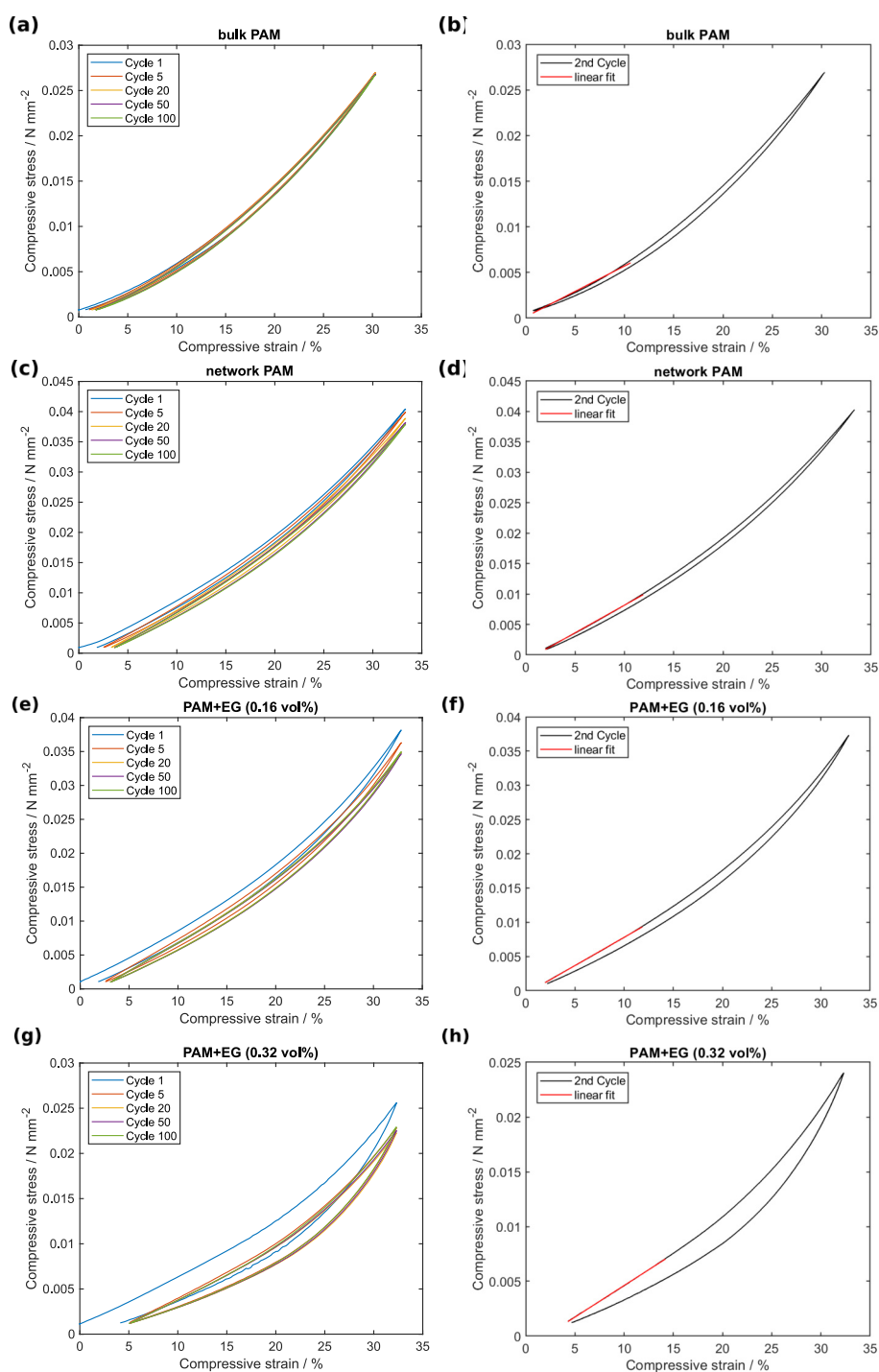
Figure 2.11. *Stress-strain curves of bulk PAM, microchannel-containing PAM and PAM-EG composites with 0.16 and 0.32 vol% EG filler content measured in cyclic compression up to 33 % strain. a, c, e, g) Representative cyclic stress-strain curves of the different sample types. b, d, f, h) Representative linear fits up to a 10 % strain mark in the second cycle for every sample type. Young's modulus was determined with a linear fit to the slope up to 5 % strain. Adapted with permission. [115] Copyright 2021, American Chemical Society.*

while network PAM and PAM-EG with 0.16 vol% EG underwent similar deformation at approximately 96 % recovered height. Hence no noticeable influence of filler material amount at this low concentrations is demonstrated. However, with higher filler content, the relative recovery decreases to 94 % (PAM-EG with 0.32 vol% EG). The results are summarized in Figure 2.13 b. As addressed earlier, the preconditioning phenomenon might lead to graphene flakes rearrangement and therefore a decrease in the composite samples height recovery.
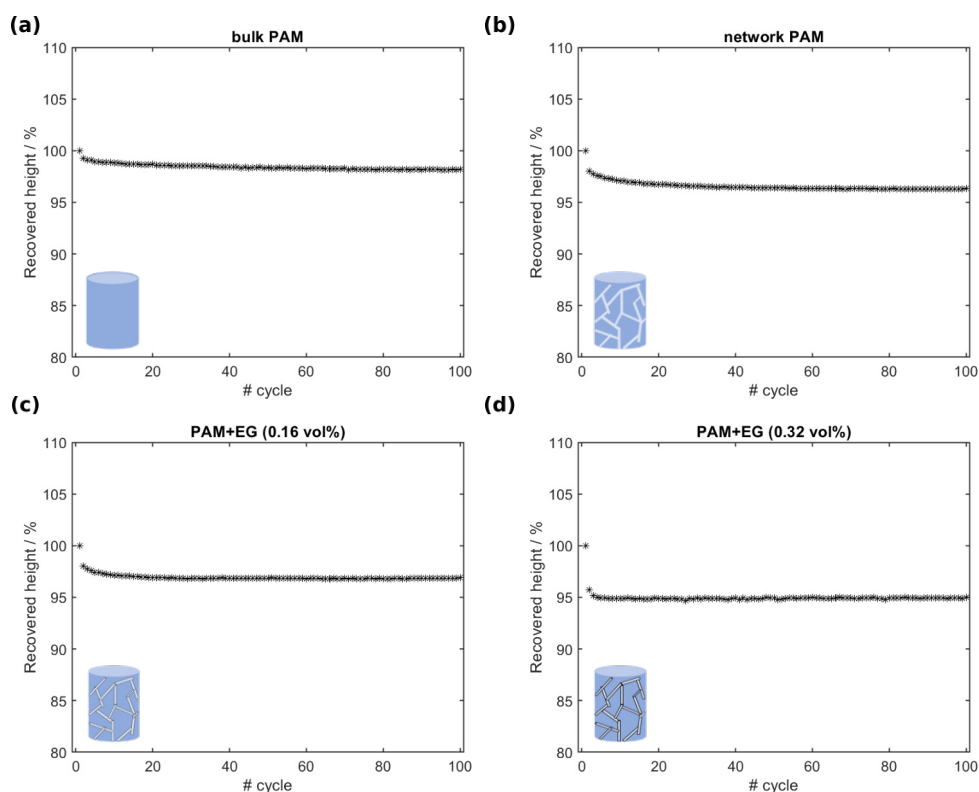
Figure 2.12. *Representative graphs for the relative height recovery in % as a function of cycle number for a) bulk PAM, b) network PAM, c) PAM-EG (0.16 vol%), d) PAM-EG (0.32 vol%). Samples deform in the first few cycles but the deformation remains constant in subsequent cycles (> 95 % for all sample types), indicating high mechanical stability with a 33 % compression strain. Reprinted with permission. [115] Copyright 2021, American Chemical Society.*

In Figure 2.13 a, the compressive Young's moduli of the different sample types are shown. Bulk PAM has a Young's modulus of 45 kPa, whereas network PAM has a Young's modulus of 83 kPa. The introduction of a microchannel network almost doubled the material stiffness due to the fact that microchannels are filled with water that has a high compressive bulk modulus of 2.25 GPa. [136] On the other hand, the Young's modulus of microchannel-containing PAM-EG composite with 0.16 vol% exfo-

liated graphene is 91 kPa, which is not significantly different from the network PAM results. This implies that introducing exfoliated graphene into the matrix neither induce material reinforcement nor alter its mechanical properties as suggested in this work's hypothesis.
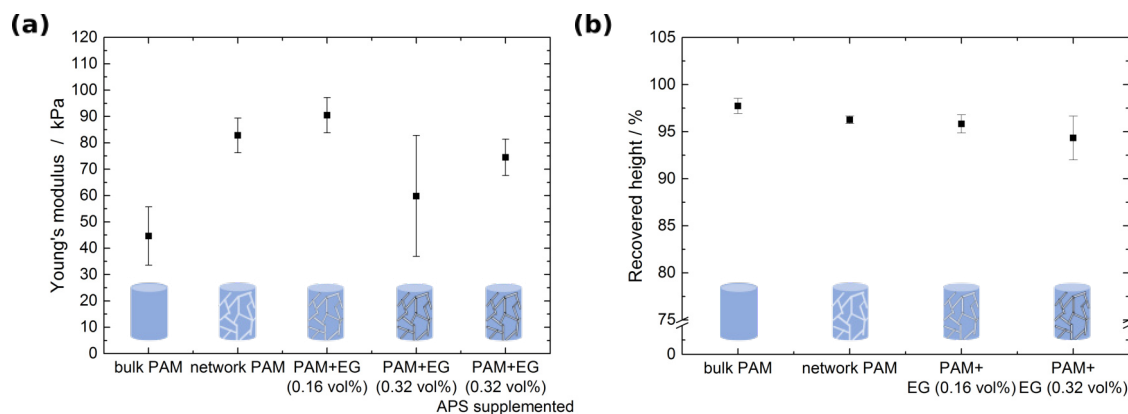
Figure 2.13. *a) Initial Young's modulus up to 5 % strain of different sample types. b) Recovered height after 100 cycles for the different sample types. Error bars depict standard deviation, N = 3. Reprinted with permission. [115] Copyright 2021, American Chemical Society.*

However, PAM-EG composites with 0.32 vol% filler content exhibited a Young's modulus of 60 kPa, which represents a 33 % increase to the bulk PAM and a 34 % decrease to the values from composites with 0.16 vol% filler material. Although a decrease in Young's modulus with an increase in filler material appears counterintuitive, it is likely due to the interactions of exfoliated graphene with ammonium persulfate (APS), which is used as the initiator in the PAM synthesis. In the production of graphene oxide sheets, APS is used to enhance the oxidation of the graphite flakes. [137] Consequently, the decomposition of APS by the exfoliated graphene might lead to a reduced number of formed free radicals available for the polymerization process. Therefore, the polymer chains become longer in length, which in turn leads to a higher elasticity and can thus explain the reduced Young's modulus. To this end, and to show that it is possible to tailor the Young's modulus by changing the polymerization parameters, the amount of APS and the catalyst N, N, N', N'-tetramethylethylenediamine (TEMED) were adjusted and tested. Instead of 10 % solutions, 20 % solutions of APS and TEMED were used and the amount of TEMED in the precursor solution was doubled.[8] As shown in

---

[8]The modified hydrogel precursor consists of acrylamide (Bio-Rad, 40 %, 1250 µL), N, N'-methylenebis(acrylamide) (Bio-Rad, 2 %, 1000 µL), HEPES buffer (Sigma-Aldrich, pH 7.5, 50 µL), 2625 µL ddH$_2$O, ammonium persulfate (APS, Sigma-Aldrich, 20 %, aq., 75 µL) and N, N, N', N'-tetramethylethylenediamine (TEMED, Sigma-Aldrich, 18.2 % aq., 200 µL). A comparison of both recipes is shown in Table B.1 in Appendix B.1.

Figure 2.13 a, the Young's modulus could be restored to $74.5\,\mathrm{kPa}$.

Furthermore, the samples ultimate compressive strengths were analyzed through applying a compression force at $10\,\mathrm{mm\,min^{-1}}$ speed until the samples collapsed and representative stress-strain curves are shown in Figure 2.14 a-d. The ultimate compressive strain of all samples is around $67\,\%$ with an ultimate compressive stress of approximately $0.1\,\mathrm{N\,mm^{-2}}$ (Figure 2.14 e).
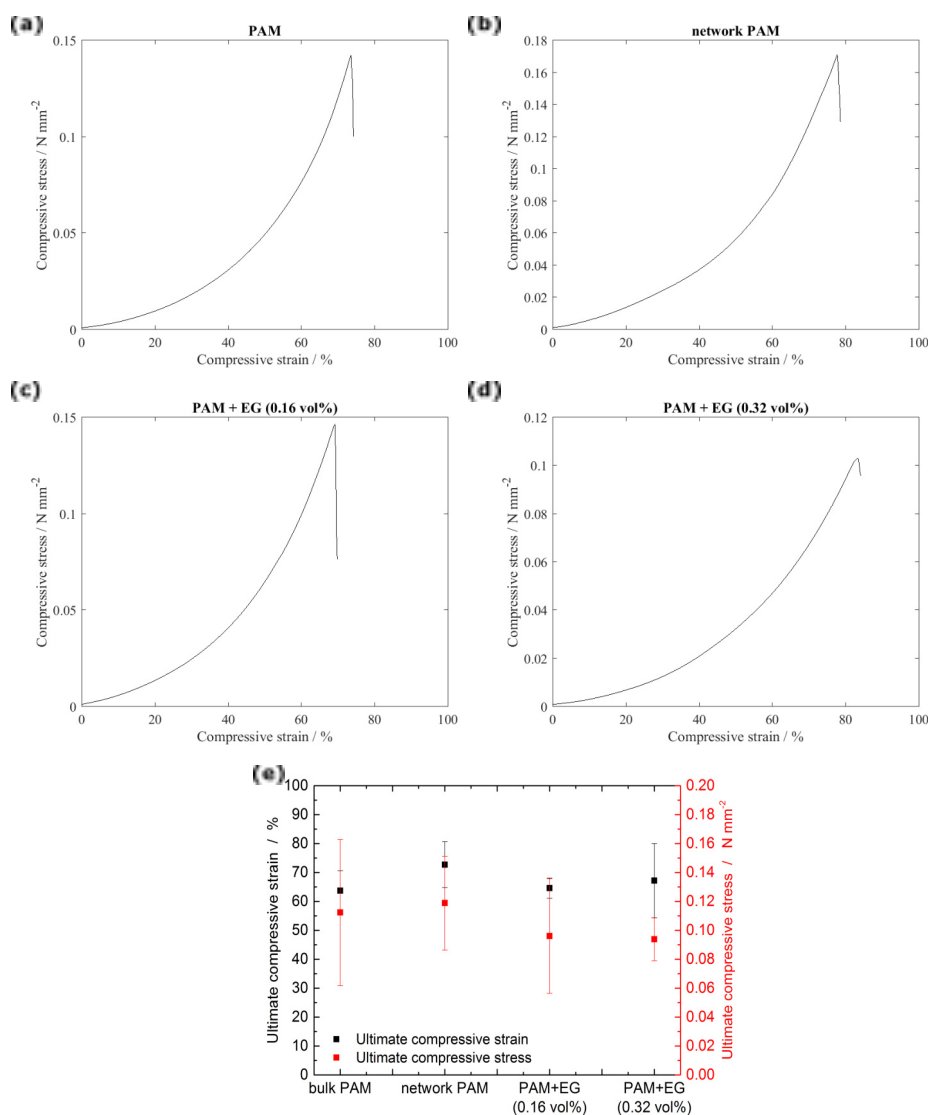
Figure 2.14. *Representative ultimate compressive stress-strain curves of a) bulk PAM, b) network PAM, c) PAM-EG (0.16 vol%), d) PAM-EG (0.32 vol%). e) Overview of ultimate compressive stress and strain values for all sample types. Error bars depict standard deviation, $N \geq 3$. Reprinted with permission. [115] Copyright 2021, American Chemical Society.*

Taken together, this method permits filler concentrations as low as $0.16\,\text{vol}\%$ EG to yield an electrical conductivity as high as $0.34\,\text{S}\,\text{m}^{-1}$ together with a negligible impact on the hydrogel matrix' mechanical integrity with a mere 10% increase in Young's modulus. This is an unprecedented success in achieving that high level of conductivity with such a low filler material to hydrogel ratio as evidenced in Figure 2.15 that highlights state of the art attempts at producing conductive hydrogels in comparison to this work. In the figure, the weight-percent normalized conductivity was depicted as a function of the Young's modulus increase in different conductive hydrogel systems.
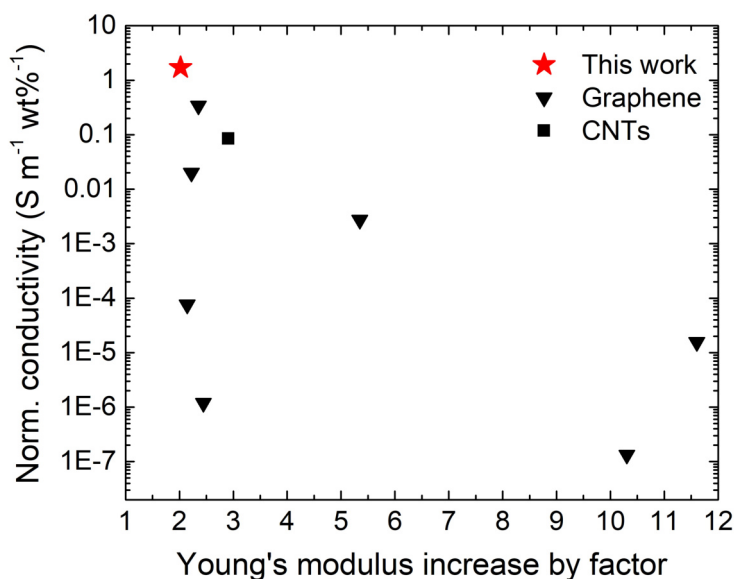
Figure 2.15. *Ashby plot showing the weight-percent normalized conductivity as a function of Young's modulus for various electrically conductive hydrogel systems based on carbon filler material incorporation. The red star indicates the results for a PAM-EG composites with $0.16\,\text{vol}\%$ from this work. The list of electrically conductive hydrogels with corresponding references are shown in Table B.3 in Appendix B.6. Reprinted with permission. [115] Copyright 2021, American Chemical Society.*

2.6. Biofunctional conductive scaffolds

The microengineered conductive hydrogels based on PAM and EG are promising candidates in a wide variety of applications. From bioelectronics and biosensing (cf. Figure 2.9 e) to biohybrid soft robotics, liquid transport and drug delivery [138], all of which can benefit from the interconnected channel system that enhances diffusion as seen in Figure B.1 in the appendix. The microchannel system can also be advantageous for creating 3D cell scaffolds where vascularization for sufficient nutrient and oxygen

transport is crucial when exceeding scaffold thicknesses of 500 µm. In terms of biohybrid robotics, tailoring the hydrogel matrix system is necessary in, e.g., PAM, which though well-known and widely used as a biocompatible (cf. Figure 2.5) hydrogel in literature, is naturally inert to cell adhesion. However, this inherent impedance to cell adhesion can be overturned after coupling biofunctional groups via covalently-binding adhesion promoting proteins [76] that can be achieved through modifying the PAM precursor by either adding, e.g., sulfo-SANPAH[9] or *N*-hydroxysuccimide (NHS) groups and then incubate the scaffold in, e.g., a fibronectin solution after sample preparation. [139]. One of the drawbacks in the first strategy is a necessary UV radiation step of the sample in order to bind sulfo-SANPAH to the PAM gel. In this work, the EG might hinder sufficient UV light penetration to the bulk sample that makes biofunctionalization hard to control. In general, an adequate functionalization and a uniform adhesion proteins dispersion throughout the scaffold is a prerequisite. Additionally, to avoid a subsequent biofunctionalization protocol after material preparation, which in turn also depends on proteins diffusion within the material, a different strategy based on gelatin methacryloyl (GelMA) was pursued in this work. GelMA inherently accommodates RGD[10] motifs that mediate cell adhesion. [140] Besides pure GelMA, various combinations of PAM and GelMA were analyzed as potentially suitable solutions for a facile scaffold biofunctionalization procedure with substantial mechanical properties.

2.6.1. Gelatin methacryloyl as a matrix material

Gelatin methacryloyl (GelMA) was synthesized following a protocol published by Shirahama *et al.* [102] 2.5 mL of methacrylic anhydride (MAA, Sigma-Aldrich) was added to 250 mL of 10 %(w/v) gelatin in carbonate-bicarbonate buffer (CB, 0.25 mol L^{-1}) and the solution was stirred at 50 °C for a predefined time before adding hydrochloric acid to adjust the pH to 7 and stop the reaction. Various reaction times (15 min, 30 min or 3 hours) resulted in different degrees of substitution (DS), i.e., the percentage of amino groups that has been substituted with methacrylate groups. The solution was then dialyzed (12 - 14 kDa molecular weight cut-off) against double distilled water for more than three days to remove salts and unreacted by-products and then subsequently lyophilized.

The synthesized GelMA polymers were examined by proton nuclear magnetic resonance (^{1}H NMR)[11] as shown in Figure 2.16 a. In comparison to the gelatin backbone spectra, the GelMA spectra shows two new peaks at 5.4 and 5.6 ppm that correspond to the methacrylamide grafts acrylic protons of both lysine and hydroxyl lysine groups (peaks a and b), which indicate that the gelatin was successfully modified with methacryl groups. The other distinctive peak (peak c) around 3 ppm is correlated to the methylene

---

[9]Sulfosuccinimidyl-6-(4′-azido-2′-nitrophenylamino)hexanoat

[10]RGD is a tripeptide sequence consisting of arginine, glycine and aspartic acid.

[11]Bruker Avance 200, Otto Diels Institute of Organic Chemistry, CAU Kiel

protons of unreacted lysine groups that do not appear in spectra of GelMA with a high DS and are thus indicating a complete conjugation of lysine with MAA. Additionally, methyl protons of methacrylamide around 1.9 ppm (peak d) are more apparent in GelMA with high DS. [102]
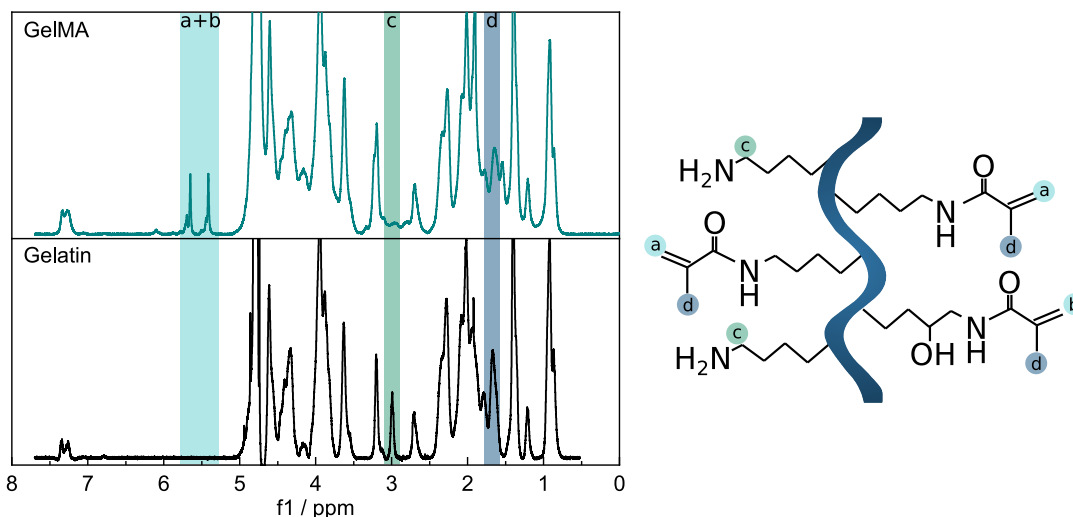
Figure 2.16. ^1H *NMR spectra of pristine gelatin (black) and synthesized GelMA (blue). The peaks correspond to acrylic protons (2H) of methacrylamide grafts of (a) lysine groups and (b) hydroxyl lysine groups, (c) methylene protons (2H) of unreacted lysine groups and (d) methyl protons (3H) of methacrylamide grafts.*

The degree of substitution (DS) of the synthesized GelMA was determined by a TNBS assay (details in Appendix B.3) and the influence of different DS and light doses[12] on GelMA stiffness was analyzed with a microindentation device (Pavone, Optics11 Life). The microindentation tests were conducted in water using a $4\,\mathrm{N\,m^{-1}}$ spring constant cantilever with an attached sphere with $23\,\mu m$ radius. Bulk samples with approximately $1\,mm$ height were fixed on silanized glass slides[13] and indented for $5\,\mu m$ at $2\,\mu m\,s^{-1}$ indentation speed at different positions. A Hertzian fit was used to determine the Young's modulus of the recorded force-distance curves using the DataViewer software[14]. GelMA with DS of $78\,\%$, $85\,\%$ and $97\,\%$ at $10\,\%$ $(^w/_v)$ in PBS containing $0.1\,\%$ $(^w/_v)$ phenyl-2,4,6-trimethylbenzoyl-phosphinate (LAP) as photoinitiator were prepared and exposed to doses of 1.5, 5.2 and $35.2\,\mathrm{mJ\,cm^{-2}}$, respectively. Samples were measured at $20\,°C$ and $37\,°C$ and the results are shown in Figure 2.17. The Young's modulus did not change significantly when the light dose changed in GelMA with 78 and $85\,\%$ DS, whereas with $97\,\%$ DS the difference was significant between samples illuminated with

---

[12]Further information about the LED system and light doses are available in Appendix B.4.
[13]Experimental details are provided in Appendix B.5.
[14]V.2.4.0, Optics11. Fits with a $R^2 \leq 0.97$ were excluded and the Poisson's ratio ν was assumed with 0.5. An exemplary force-distance curve with Hertzian fit is shown in Figure B.4
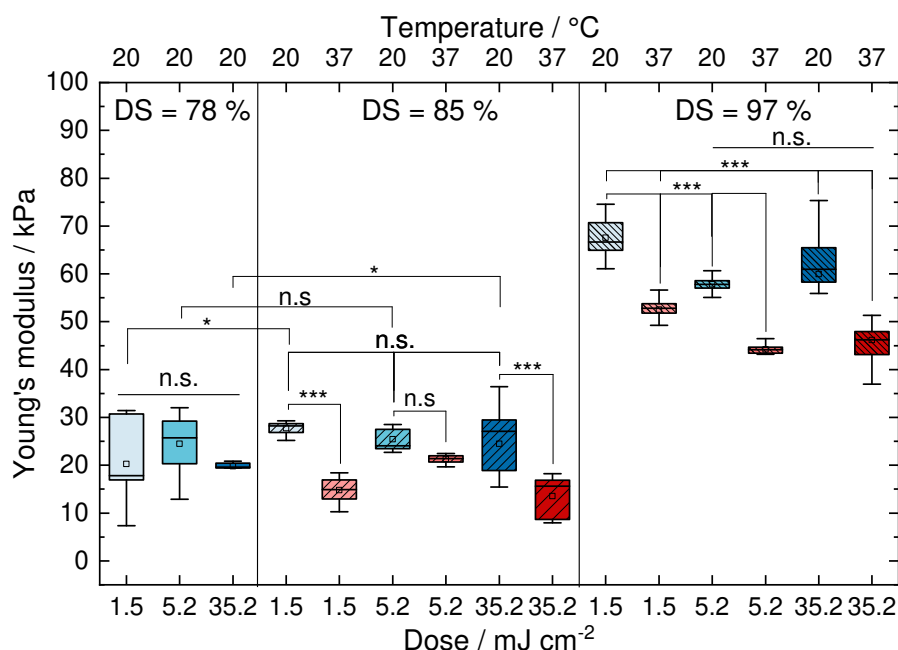
Figure 2.17. *Young's modulus of bulk GelMA samples with different degree of substitution (DS) exposed to different light doses and measured at different temperatures. Young's modulus was determined with microindentation using a Hertzian fit. ANOVA one-way with post hoc Tukey test was used for statistical analysis. *** p < 0.001, * p < 0.05, n.s. = not significant.*

$1.5 \, \text{mJ cm}^{-2}$ and 5.2 or $35.2 \, \text{mJ cm}^{-2}$, respectively. Interestingly, the Young's modulus decreases with higher doses. The difference between Young's moduli of 78 % DS and 85 % DS GelMA for a dose of $1.5 \, \text{mJ cm}^{-2}$ and $35.2 \, \text{mJ cm}^{-2}$, respectively, was significant (p = 0.0047; p = 0.01009) but not significant for an intermediate dose. As the difference between varying doses for GelMA with the same DS is not significant as well, this leads to the conclusion that a dose of $1.5 \, \text{mJ cm}^{-2}$ is already high enough to crosslink the samples completely. Additionally, the difference in DS of 78 and 85 % is apparently not large enough to yield different Young's moduli. Nonetheless, 97 % DS GelMA has significantly higher Young's moduli than those with lower values. At room temperature, the Young's modulus for GelMA with 78 and 85 % DS is between 25 and 30 kPa, whereas at 97 % DS it is around 55 to 68 kPa, and at physiological temperatures Young's moduli decreases noticeably to around 16 kPa for GelMA with 85 % DS and to around 45 to 58 kPa for GelMA with 97 % DS.

In conclusion, only GelMA with a DS higher than 95 % was employed in cell experiments for its reliability and batch-to-batch stability as well as for having a Young's modulus around 50 kPa at physiological temperatures. This stiffness is within a suitable range for biohybrid devices as reported in previous works such as in Lee *et al.* [22] where a gelatin body with a stiffness of 56 kPa was employed.

2.6.2. Polyacrylamide - gelatin methacryloyl matrices

GelMA can either be used in its pure form or combined with polyacrylamide to facilitate the infiltration process during scaffold preparation as the gelatin, and consequently GelMA, has thermoresponsive properties. [88] Figure 2.18 shows the changes in both storage and loss modulus as well as the viscosity change as a function of temperature for gelatin and GelMA hydrogels[15]. The viscosity in bulk GelMA samples decreased with increasing temperature and showed slight fluctuations at around 32 °C, gelatin's melting temperature (Figure 2.18 b). This fluctuation is most likely attributed to a sudden break of physical crosslinks, e.g., hydrogen bonds and triple helices, that form when aqueous gelatin solutions solidify below 25 °C. [88] At physiological temperatures, the GelMA viscosity is around 84 Pa s and increases to around 267 Pa s at 20 °C, which represents a 68.5 % gain. Therefore, the GelMA solutions as well as the templates need to be kept at around 40 °C to enable the infiltration process that is necessary for preparing microengineered conductive scaffolds.
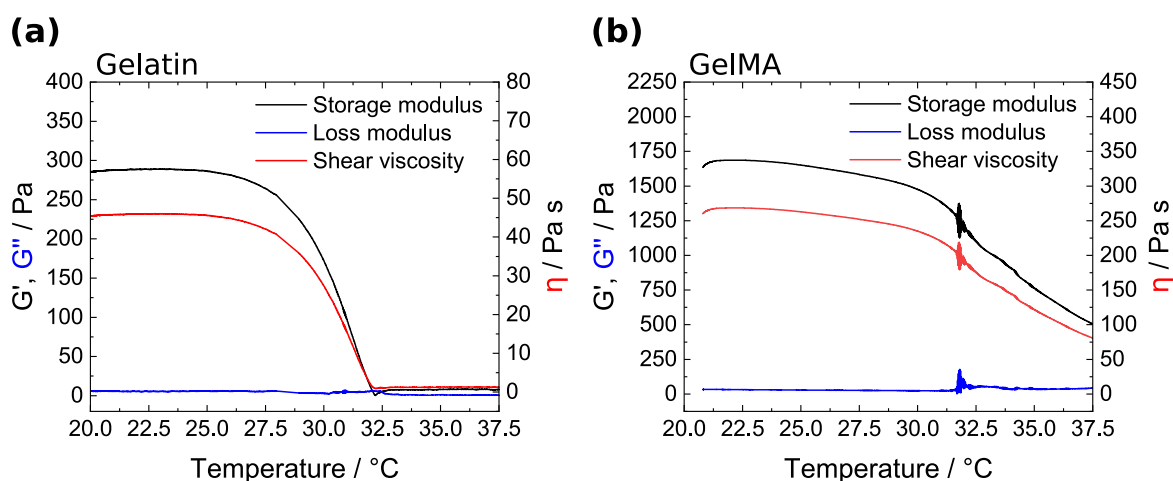
Figure 2.18. *Rheological analysis of a) gelatin and b) GelMA bulk hydrogels. Storage modulus G', loss modulus G'' and viscosity η as a function of temperature are shown. Gelatin melts at 32 °C and remains in liquid state at physiological temperatures. GelMA's viscosity decreases from 267 Pa s to 84 Pa s with increasing temperature but maintains its solid state.*

An additional challenge in the preparation of microengineered conductive hydrogels is the UV light absorption of ZnO [141] that impedes the light-induced polymerization of GelMA, which is the state of the art fabrication method. Moreover, the radical starter system consisting of APS and TEMED becomes more sensitive at elevated temperatures and thus accelerates polymerization time, therefore it is necessary to operate

---

[15]Gelatin and GelMA solutions at 10 % (w/v) in PBS containing 0.1 % (w/v) LAP as photoinitiator were prepared, placed in teflon molds, irradiated with 1.5 mJ cm^{-2}, allowed to gelate at room temperature and stored in water until the experiments.

Table 2.1. Components for the synthesis of polyacrylamide-gelatin methacryloyl hydrogels.

	PAM	PAM0.75 GelMA0.25	PAM0.5 GelMA0.5	PAM0.25 GelMA0.75	GelMA
Component		**Quantity (μL)**			
PAM precursor (Recipe B)	1000	750	500	250	0
GelMA, DS > 97 %, 10 wt%	0	250	500	750	1000
APS, 20 wt%	30	30	30	30	30
TEMED, 10 wt%	40	40	40	40	40

APS = ammonium persulfate; GelMA = gelatin methacryloyl; PAM = polyacrylamide; TEMED = N, N, N', N'-tetramethylethylenediamine

Recipe B: acrylamide (40 %, 1250 µL), N, N'-methylenebis(acrylamide) (2 %, 1000 µL), HEPES buffer (pH 7.5, 50 µL), 2625 µL ddH$_2$O, APS (20 %, aq., 75 µL)

with concentrations that maintain appropriate polymerization times but yield stable hydrogels. Nevertheless, this issue can be addressed with the hypothesis that mixing PAM with GelMA would alleviate the thermoresponsive sensitivity in a mixed hydrogel matrix throughout which the GelMA would provide the necessary adhesion motifs for cell attachment. This was shown in an *in vitro* and *in vivo* study using chondrocytes for cartilage repair. [142] Each of these two hydrogels have methacrylate groups that are responsible for covalent crosslinking during polymerization. The compositions and individual amounts for hydrogel preparation are shown in Table 2.1 where the numbers next to PAM and GelMA indicate their respective proportions.

The Young's modulus of different PAM-GelMA bulk scaffolds with varying ratios were tested at room temperature using a microindenter (Pavone, Optics11 Life). In a similar setup to what was described in the previous section, a 4 N m^{-1} spring constant cantilever with a 23 µm radius attached sphere was used on approximately 1 mm height samples that were indented for 5 µm at 2 µm s^{-1} indentation speed at different positions. A Hertzian fit was employed to calculate the Young's modulus from the acquired force-distance curves using the DataViewer software[16] and the results are shown in Figure 2.19 a. Bulk PAM generated a Young's modulus of around 45 kPa, which coincides with values determined from compression tests (cf. Section 2.5, Figure 2.13). Albeit an initial increase in the PAM Young's modulus to around 55 kPa when 25 % GelMA was added, an additional increase in GelMA concentration led to a drop in the composite's Young's modulus to a mean value of approximately 25 kPa for bulk samples

---

[16]V.2.4.0, Optics11. Fits with a $R^2 \leq 0.97$ were excluded. The Poisson's ratio ν is assumed with 0.5.

with 25 % PAM and 75 % GelMA. The Young's modulus of pure GelMA bulk samples was measured to be around 55 kPa.

Figure 2.19 b displays phase contrast images of skeletal muscle cells (C2C12) grown on pure PAM and GelMA as well as on PAM-GelMA composite surfaces for three days. Cells on pure bulk PAM scaffolds cells show round morphology that indicates poor cell adhesion, whereas on 25 % GelMA bulk scaffolds they already exhibit a significantly enhanced cell spreading and adhesion that continues to improve with increasing GelMA content.
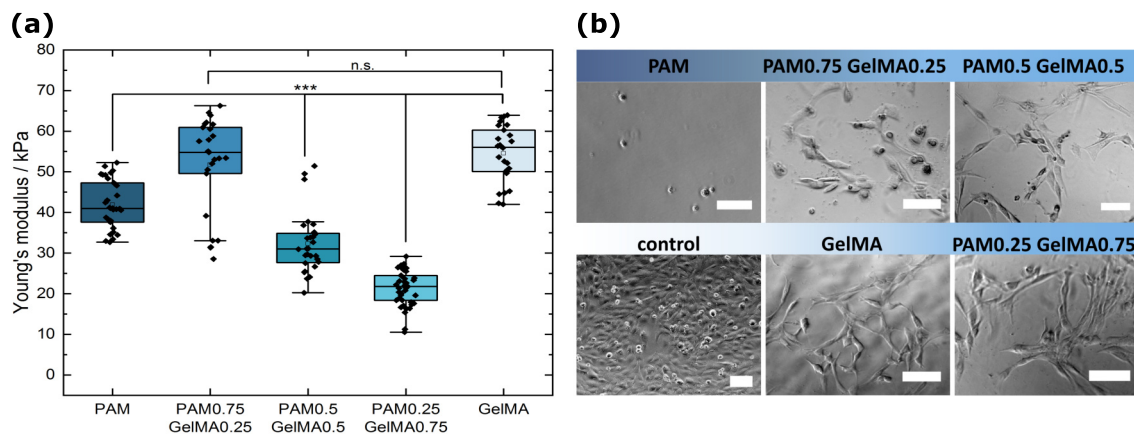
Figure 2.19. *a) Young's modulus of different compositions of polyacrylamide (PAM) and gelatin methacryloyl (GelMA) bulk hydrogels as determined by microindentation method using a Hertzian fit. ANOVA one-way with post hoc Tukey test was used for statistical analysis. *** p < 0.001, n.s. = not significant. b) C2C12 skeletal muscle cells grown for three days on bulk PAM, PAM-GelMA and GelMA scaffolds. On pure PAM scaffolds, cells show a round morphology and poor cell adhesion while cells on PAM-GelMA samples are well spread. The blue color saturation indicates PAM concentration. Scale bars: 100 μm.*

Incidentally, the poor cell adhesion on PAM samples is not the result of low biocompatibility as the cytotoxicity of microchannel-containing polyacrylamide composites was analyzed using an indirect MTT extraction test (cf. Figure 2.5 in Section 2.2) with PAM samples demonstrated higher biocompatibility than 90 % for undiluted extracts, thus regarded as biocompatible. GelMA's biocompatibility is extensively studied in literature for *in vitro* and *in vivo* applications [86, 143], thus PAM-GelMA composites are expected to be biocompatible as well, which is further confirmed by the normal morphology of muscle cells grown on these composites.

Taken together, as small amounts of GelMA added to PAM improve cell adhesion, the precursor solutions are still facile to infiltrate, and the mechanical properties do not change significantly, this makes such mixtures suitable matrix materials for microengineered conductive scaffolds.

2.6.3. Contractile cells on microengineered conductive scaffolds

Skeletal muscle cells (C2C12) were used to analyze cell adhesion on the surface of thin conductive hydrogel scaffolds based on exfoliated graphene and GelMA. The preparation procedure follows similar steps to those presented in Section 2.2 apart from exchanging the polyacrylamide solution with a pure GelMA precursor solution (cf. Table 2.1) that was infiltrated to result in a GelMA-EG scaffold with a 0.16 vol% EG concentration.

Figure 2.20 shows C2C12 cells cultured on flat, microengineered GelMA-EG scaffolds five days after changing to starvation medium[17] immunofluorescently stained[18] with Hoechst (nucleus, DAPI), anti-myosin heavy chain 7 (myosin, Alexa Fluor® 488) and rhodamine-phalloidin (actin filaments). In the bright field images, dark regions are areas with exfoliated graphene on which more myotube formation can be observed.
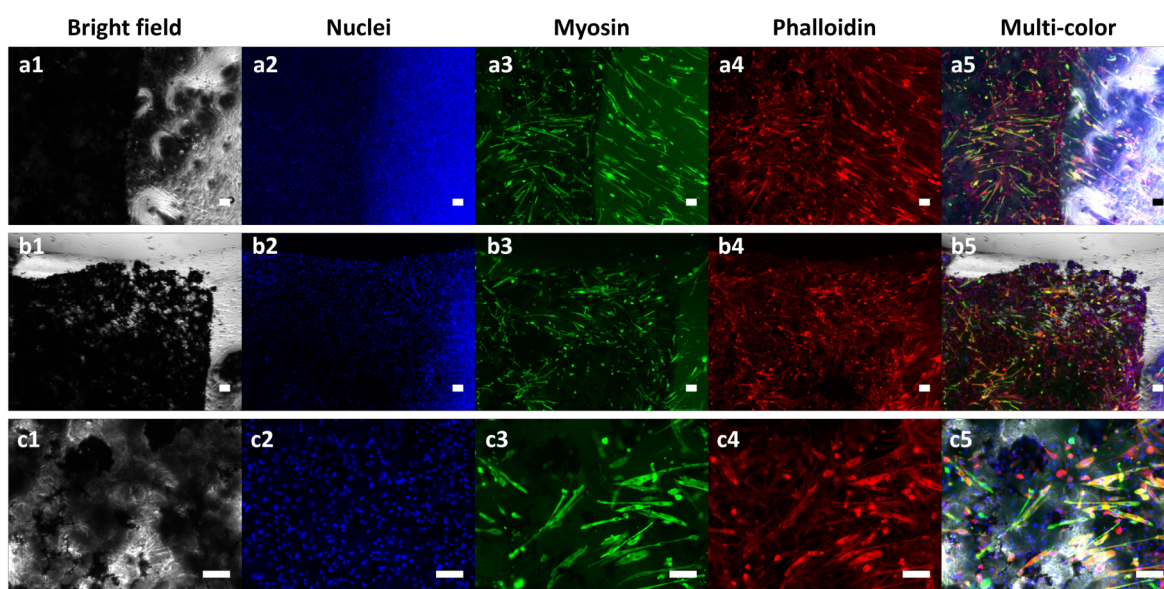
Figure 2.20. *Immunofluorescent staining of C2C12 skeletal muscle cells on GelMA-EG composite scaffolds (200 000 cells/sample) five days after differentiation against Hoechst (nuclei, blue), myosin-heavy chain (green) and phalloidin-rhodamine for actin filaments (red). Scale bars: 100 μm.*

One of the remaining challenges is the alignment of muscle cells on the scaffold's surface, which is crucial for orientating the forces cells exert on their environment. In a perspective study to help organize skeletal muscle cells and align the myotubes, the scaffold surface is microstructured using a grooved stamp given that t-ZnO templates

---

[17]Dulbecco's modified Eagle medium + 2 % FBS + 1 % Penicillin/Streptomycin.
[18]Experimental details are provided in Appendix A.4.2.

themselves are easy to mold and model in various shapes and forms. [125] One critical aspect in this procedure is to keep the stamp on the scaffold while the hydrogel precursor is infiltrated in order to avoid filling the microstructure's grooves with aqueous hydrogel precursor. The microstructured stamp can either be prepared using PDMS stamps molded by stereolithographic structuring of Si-wafers or by additive manufacturing processes, e.g., SLA (stereolithographic) printing where resolutions of less than $100\,\mu m$ are possible, or possibly through two-photon polymerization with which even finer resolutions of around $500\,nm$ in xy and $1000\,\mu m$ in z are achievable. Microstructuring the hydrogels surfaces for aligning skeletal muscle cells or cardiomyocytes is a common strategy that is regularly employed in biohybrid robotic research. [21,22] Typical groove width for aligning muscle cells are around $10\,\mu m$ to $100\,\mu m$ [38,140,144], and a schematic representation of a proposed preparation scheme is displayed in Figure 2.21. The microstructured stamp with an SLA printed example for creating pockets in the hydrogel (Figure 2.21 a2) is used to either structure t-ZnO templates before (Figure 2.21 b) or after (c) infiltration with a conductive filler dispersion besides a subsequent infiltration step with the hydrogel precursor. After the wet-chemical etching of t-ZnO, the hydrogel is detached from the stamp and can be used for cell culture after sufficient washing with PBS. A similar technique was already successfully employed for creating pockets in microengineered conductive scaffolds from exfoliated graphene and polyacrylamide for embedding retinal fish organoids and is still ongoing work for contractile cell types. As other works showed successful alignment of skeletal muscle cells on grooved hydrogels [140], this strategy should be pursued for orienting the forces cells exert on their environment to enable cell-induced contraction of scaffold material.
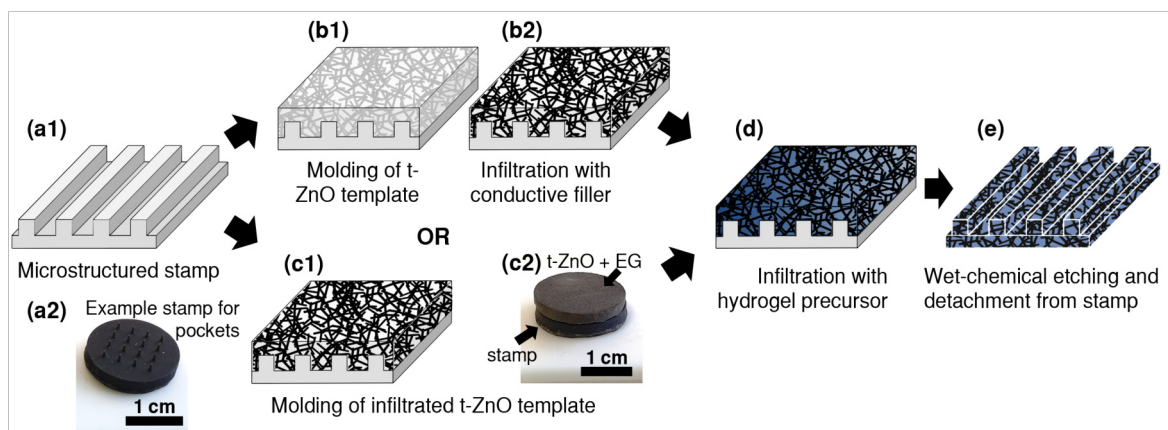
Figure 2.21. *Schematic representation of a conductive hydrogel surface micropatterning strategy prior b) or after c) infiltration with a conductive filler dispersion, followed by subsequent infiltration with both a hydrogel precursor (d) and wet chemical removal of t-ZnO e) and detachment from the stamp. a1) and c2) show an example of a 3D printed stamp to generate pockets and t-ZnO-EG template molded on top of the stamp.*

In contrast to skeletal muscle cells, **cardiomyocytes** require neither a specific alignment on the scaffold surface nor electrical stimulation as they contract spontaneously. However, this advantage is partly cancelled out by the fact that no cardiomyocyte cell line able to generate enough forces are commercially available [13], hence primary neonatal cardiomyocytes are commonly used, albeit animals are sacrificed, which raises ethical questions. Therefore, induced pluripotent stem cells (iPSCs) can serve as a good alternative as they are differentiated into cardiomyocytes, a time-consuming yet valuable process to prepare cardiomyocytes (iPSC-CM) with all original features. In this work, I tested iPSC-CM cell adhesion and beating behavior on microengineered GelMA-EG scaffolds. The cells and media were kindly provided by Dr. Ayca Seyhan Agircan and Prof. Dr. Johannes Backs from Heidelberg University Hospital. Figure 2.22 shows iPSC-CMs cultured on fibronectin-coated cell culture plastic (a) and microengineered, conductive GelMA-EG scaffolds (b) after being immunofluorescently stained with Hoechst (nucleus, DAPI), anti-myosin (myosin heavy chain, Alexa Fluor®488) and rhodamine-phalloidin (actin filaments). Cells in the control sample are well spread and show discernible actin stress fibers and myosin filaments whereas those on microengineered GelMA-EG scaffolds have a rather round morphology and demonstrate no apparent actin stress fibers, which signifies poor cell adhesion.

(a) Control + FN   **(b) GelMA-EG + FN**
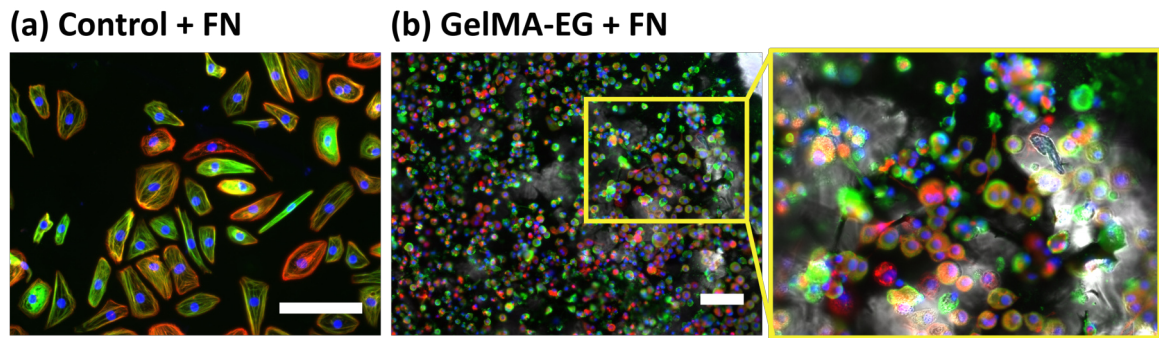
Figure 2.22. *iPSC-CM cultured on a) fibronectin (FN)-coated glass slides and b) FN-coated microengineered, conductive GelMA-EG scaffolds (20 µg/sample). Cells were stained with Hoechst (nucleus, blue; anti-myosin (myosin heavy chain green and rhodamin-phalloidin (actin filaments, red). The cells in the control are well spread and show distinct actin stress fibers and myosin filaments. Cells on microengineered GelMA-EG scaffolds have a more round morphology and show little actin stress fibers. Scale bars: 100 µm.*

Embryonic myocardium is rich with fibronectin [145] so iPSC-CMs are more likely to bound to fibronectin than to collagen and RGD motifs widely present in GelMA. However, with the lack of reactive groups that provide covalent bonding, the microengineered scaffolds coating with fibronectin was based on physisorption that was presumably insufficient for supporting an overall good cell adhesion. Nevertheless, some iPSC-CMs were able to adhere well enough on GelMA-EG scaffolds to exercise concentric contractions that translates into deformation of the underlying thin scaffold.

This phenomena can not be observed when these cells are cultured on solid surfaces where they do not show any change in their length and therefore isometric contraction as demonstrated in Figure 2.23 a.
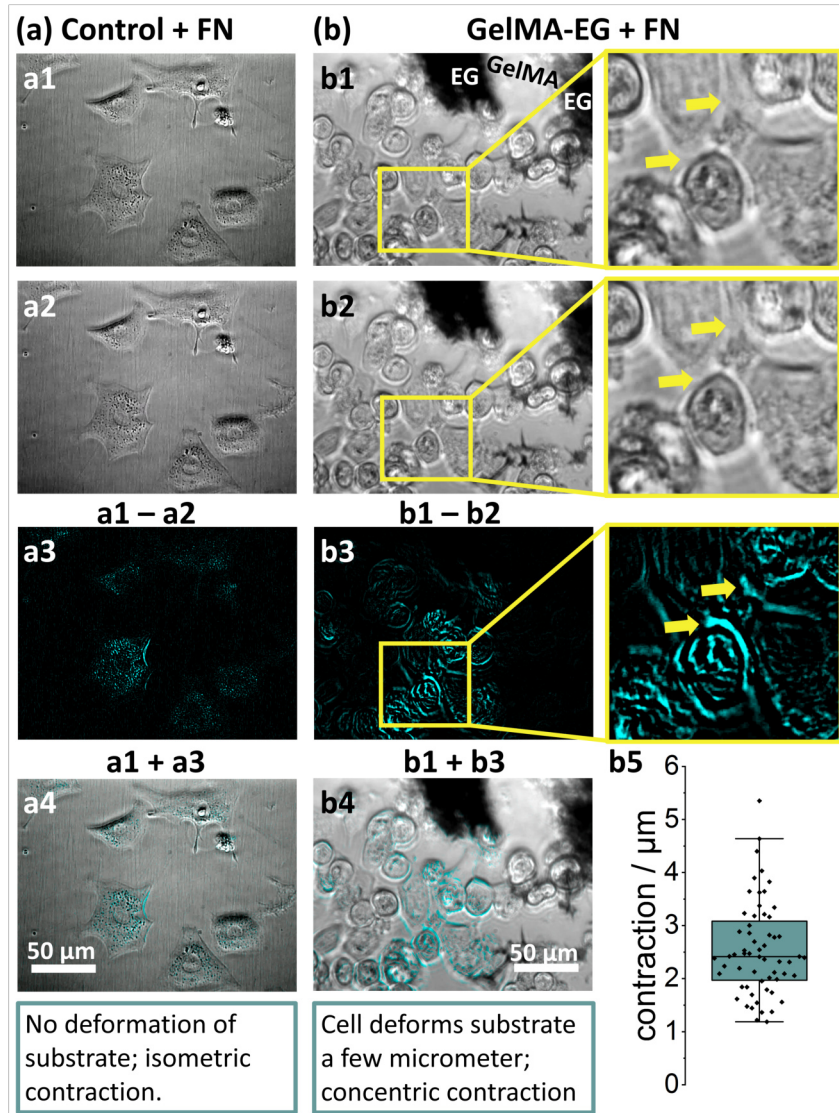
Figure 2.23. *iPSC-CM cultured on a) fibronectin (FN)-coated cell culture plastic and b) FN-coated, flat, microengineered, conductive GelMA-EG scaffolds ($20\,\mu g$/sample). a1, a2, b1, b2) show cells at two different time points during a contraction. The yellow arrows in b) highlight areas where contraction is particularly visible. a3, b3) shows the difference between images in a1 and a2 or b1 and b2, respectively. a4, b4) shows an overlay of a1/b1 with a3/b3, respectively, highlighting the changes (cyan) during a contraction. Cells on cell culture plastic show isometric contraction, i.e., no change in their length during a contraction, whereas cells on GelMA-EG show concentric contraction deforming the underlying GelMA substrate. b5) shows measurements of how much the GelMA substrate was deformed during cell contraction.*

Figure 2.23 a1 and a2 show the beating behaviour on cell culture plastic at two different time points during a contraction. To examine the change in between the two stages, the two images were subtracted from each other using the Image Calculator function in the ImageJ [146] software to excerpt the difference (a3), which was then superimposed onto the original image (a4) to elucidate the transformation (displayed in cyan color) upon contraction in both the cell and scaffold. A similar analysis procedure was followed for cells grown on GelMA-EG (b). The analysis show that cells cultured on plastic did not alter their length as the change was only visible within the cell itself, i.e., isometric contraction, whereas cells on GelMA-EG were able to perform concentric contraction and impose scaffold deformation that is particularly visible in the areas marked with arrows in (b). This visible shift in length was measured using ImageJ, analyzed in Figure 2.23 b5 and suggests approximately $2.5\,\mu m$ substrate deformation, which when compared with the cell's original length yields about $5\,\%$ change.

For an overall contraction of the scaffold material, Lee *et al.* [22] reported a cell density of $2.2 \cdot 10^5\,cm^{-2}$ on each of the two sides of a hydrogel backbone to power an artificial biohybrid fish. Using a comparable cell density on microengineered GelMA-EG is a purposeful aspect, but equally important is the cell adhesion that needs to be enhanced in order to enable concentric contractions of cardiomyocytes using biofunctionalization strategies that promote chemical linking of fibronectin to GelMA like an EDC-sulfo-NHS[19] coupling strategy. [22]. Such strategies could lead to the necessary increase in density of well-adhered cells that are required for the cell-induced macroscopic scaffold actuation. For aligning the cardiomyocytes on the hydrogel surface, a fibronectin micropatterning strategy [145] could be also taken into consideration.

2.7. Thermoresponsive scaffolds

Poly-N-isopropylacrylamide (PNIPAM) is a well-known temperature-responsive polymer that is used as a stimuli-sensitive material in drug delivery systems [81, 89], for studying cellular responses to cyclic forces *in vitro* [65] and has recently evolved as a commonly used hydrogel in soft robotics. As a thermoresponsive hydrogels, PNIPAM is in a hydrated, swollen state below the lower critical solution temperature (LCST, $32\,°C$), whereas when exceeded, the hydrophobic functional groups in the polymer chains become dominant and thus cause the chains to collapse. This leaves the hydrogel in a contracted, dehydrated state, which is usually too stiff to be used as a mechanically-apt scaffold in biohybrid robotics. Nonetheless, this effect is exploited in a process called cell sheet engineering through which 2D cell films can be prepared and potentially used in, e.g., biohybrid robotics to power a microspherical heart pump. [13, 101] The temperature-induced changes in hydrophilicity and the associated

---

[19]EDC = 1-ethyl-3-(3-dimethylaminopropyl)carbodiimide hydrochloride, sulfo-NHS = N-hydroxy-sulfosuccinimide

strong shrinkage when heated above its LCST can be utilized for actuation in soft robotics as demonstrated in Figure 2.24. When a macroscopic PNIPAM[20] structure was anisotropically heated by a heating rod (Figure 2.24 a), it bent because the hydrogel structure collapsed due to the localized temperature increase above PNIPAM's LCST. This process is accompanied by a change in opacity and the transparent parts in the figure were kept at a temperature below the LCST whereas opaque parts are those heated above the LCST.

(a)

(b)
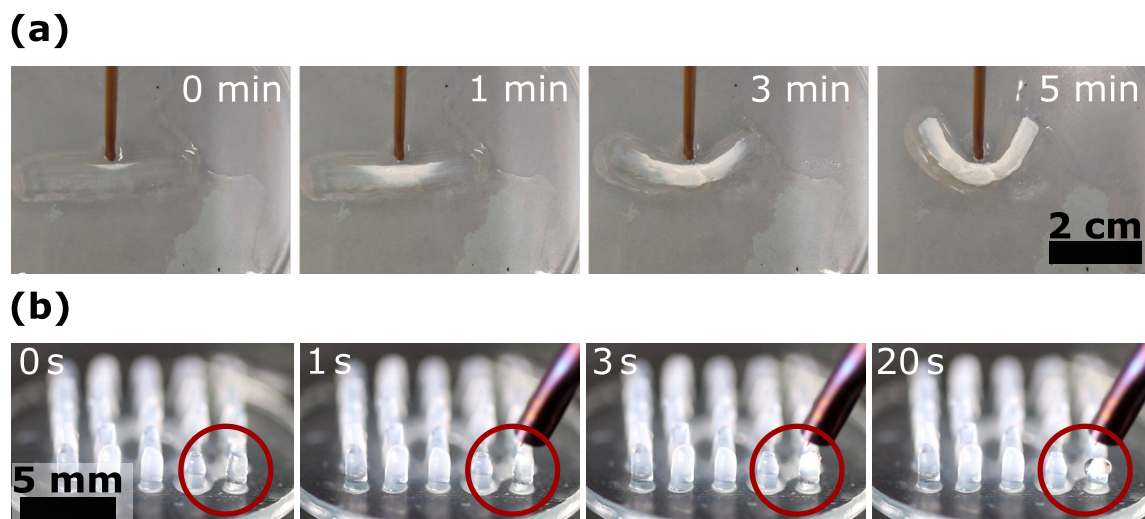
Figure 2.24. *a) Bending of a macroscopic PNIPAM structure in response to anisotropic heating by a heating rod. Transparent parts of the material still at a temperature below the LCST, whereas the opaque parts of the material are heated above the LCST. b) A single micropillar (highlighted by the red circles) in a micropillar structure from PNIPAM is heated by a heating rod and shrinks within 20 s by expelling water.*

In Figure 2.24 b, a single micropillar (highlighted with red circles in the image sequence) in a micropillar structure was heated by a heating rod that led to its shrinkage whereas the neighboring micropillars remained mostly unaffected. The water expulsion due to the temperature-induced change in hydrophilicity is clearly visible by the water droplet at the micropillar side after 20 s. This micropillar structure resembles a macroscopic version of a microfluidic bumper array used for sorting beads according to their sizes, [147] thus a miniaturized version of this system could potentially serve as a

---

[20]PNIPAM precursor solution for experiments shown in Figure 2.24 and Figure 2.25 consisted of 600 mg N-isopropylacrylamide, 10 mg N,N'-methylenebis(acrylamide), 10 mg ammonium persulfate and 4500 µL water. After degassing the solution, 46 µL of N,N,N',N'-tetramethylethylenediamine (TEMED) was added and the solution was filled in suitable teflon molds for preparing bulk samples in a specific form, or drop-cast on a t-ZnO templates, and afterwards left to polymerize for two hours at room temperature. For experiments shown in Figure 2.26, the PNIPAM precursor solution consisted of 600 mg N-isopropylacrylamide, 15 mg N,N'-methylenebis(acrylamide), 10 mg ammonium persulfate, 4600 µL water and 23 µL TEMED.

cell sorting device. Such setup would also benefit from adding a dynamic component to an otherwise static, rigid device via introducing channels that could open and close in response to temperature changes. Also, incorporating gold nanoparticles in the hydrogel would enable optical heating and allow a spatial control. [65] As the PNIPAM biocompatibility when used in a cellular environment is an important aspect, it was determined using an indirect MTT extraction test that was performed according to ISO-10993[21] using rat embryonic fibroblasts (REF52 wt) as a model system and culture medium as a control (Figure 2.25 d). The PNIPAM samples demonstrated higher biocompatibility than 88 % for undiluted extracts and can thus be used in *in vitro* applications.
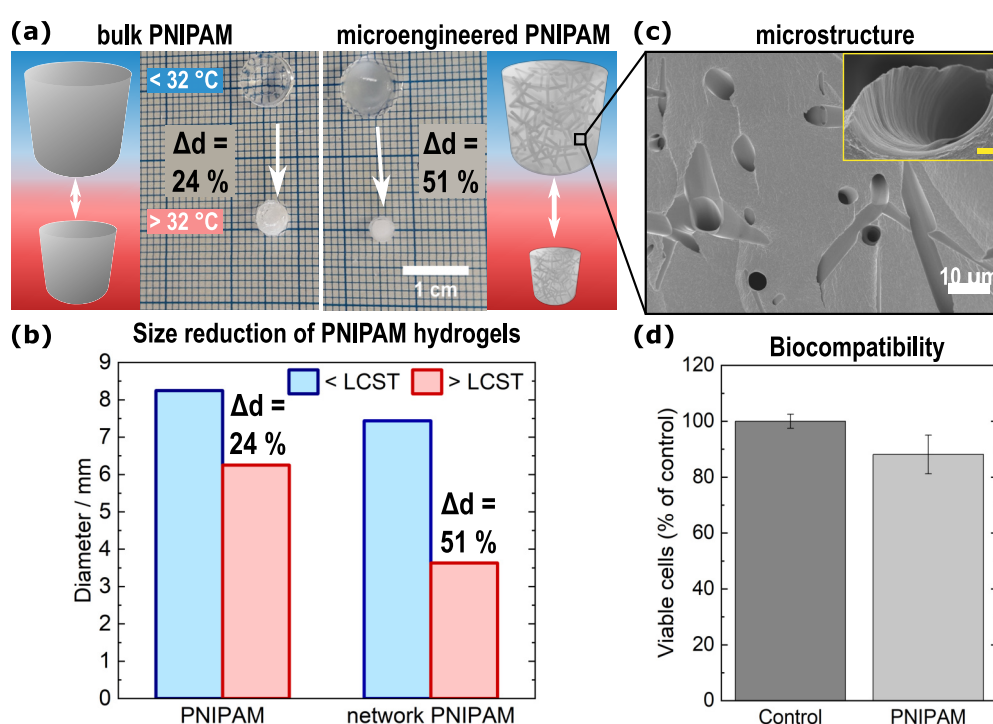
Figure 2.25. *a) Response to temperature changes of PNIPAM structures and microchannel-containing PNIPAM structures. Upper row: samples at temperatures lower than LCST (32 °C), lower row: samples at temperatures above LCST. b) Microchannel-containing PNIPAM structure (network PNIPAM) response to temperatures above LCST is more apparent (51 % size reduction in diameter) than for bulk PNIPAM (24 % size reduction in diameter). c) Microstructural analysis with scanning electron microscopy showing the microchannels originating from the tetrapodal ZnO structure in PNIPAM. The inset shows a channel surface. Inset (yellow) scale bar: 1 µm. d) Cell viability of rat embryonic fibroblasts (REF52 wt) exposed to medium extracts of bulk PNIPAM with an indirect MTT extraction assay. Error bars depict standard deviations, N = 6.*

---

[21]Experimental details are provided in Appendix A.3.

The PNIPAM response rate in both presented examples is slow, with the first example on a several minutes scale as the flow of water in and out of the hydrogel is restricted due to passing through the hydrogel's small pores. Hence, tuning the porosity of the hydrogel will positively impact the rate of water transport as the pore structure influences the phase transition rate. [89] Therefore, it is hypothesized that introducing a microchannel-system in the hydrogel[22] will lead to a higher water flow rate and a greater stored quantity as water can then pass through the microchannels and does not need to pass solely through the hydrogel's small pores. Figure 2.25 a shows a comparison of bulk and microchannel-containing PNIPAM[23] above and below the LCST, with both samples having similar initial sizes. Samples in the hydrated state at a temperature below $32\,°C$ are shown in the upper row, whereupon the microchannel-containing PNIPAM sample appears milky due to light scattering by the channel walls. Above $32\,°C$, the bulk as well as the dehydrated and collapsed microchannel-containing samples demonstrate a diameter reduction of approximately 24 and $51\,\%$, respectively (Figure 2.25 b). This nearly twice as much shrinkage is a result of introducing the microchannel-system that only makes up approximately $6\,\%$ of the sample volume. Figure 2.25 c shows a microstructural SEM image displaying the tetrapodal ZnO structure present in the hydrogel matrix and the channel surface in the inset. SEM imaging was kindly performed by Dr. Irene Wacker in the group of Prof. Rasmus R. Schröder at the Center of Advanced Materials (CAM) at Heidelberg University.

In a work carried out in the group by Tobias Spratte and published in Spratte, Arndt *et al.* [97], the actuation capabilities of microengineered PNIPAM were tested with a simple temperature-controlled gripper as demonstrated in Figure 2.26 a for bulk PNIPAM and in Figure 2.26 b for microengineered PNIPAM. The gripper was made from two 3D-printed polylactic acid (PLA) parts connected by a joint, with the sample acting as an artificial muscle between the two arms. When the gripper was transferred from a water bath at $22\,°C$ to one at $42\,°C$, the sample dehydration caused a contraction of the artificial muscle that was significant enough in the microengineered hydrogel to close the gripper and hold and deform a piece of sponge positioned between the lower arms ends. The microengineered hydrogel caused the gripper's lower ends to deform by approximately $4.7\,mm$, which corresponds to roughly a $54\,\%$ deformation. On the other hand, the contraction of bulk hydrogels was not sufficient for neither closing the gripper arms nor holding the sponge as the gripper opening was shut by approximately $0.7\,mm$ that translates to a mere $5.3\,\%$ deformation. This small deformation is attributed to the small volume change and weak force generation. In contrast, the considerable potential to change the microengineered hydrogel dimensions substantially makes it ideal for implementation in soft robotic designs to move and transport objects underwater.

---

[22]Part of this work was published in Spratte, Arndt, *et al.*, *Advanced Intelligent Systems*, 2021. [97]

[23]The preparation procedure follows the same steps as explained in Section 2.2 except for the infiltration steps with the nanoparticle dispersion.
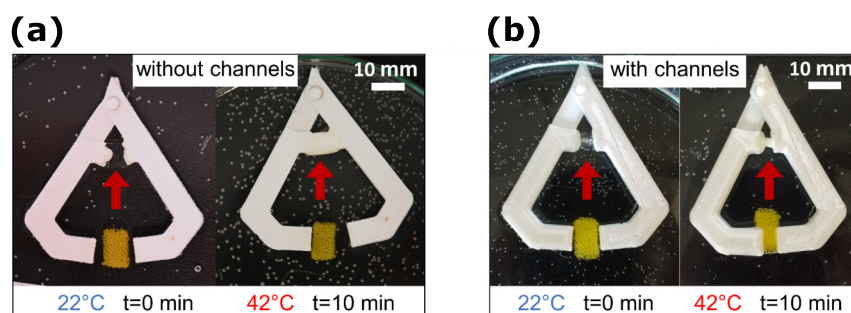
Figure 2.26. *Temperature-controlled grippers driven by a) bulk or b) microengineered hydrogel (with 5 vol% microchannels) as an artificial muscle (see red arrows), respectively. Bulk hydrogel is not able to move the gripper arms while the microengineered sample can close the gripper opening halfway to hold and deform a piece of sponge. The experiment was performed by Tobias Spratte. The image is reproduced under the terms of the CC-BY Creative Commons Attribution 4.0 International License (`http://creativecommons.org/licenses/by/4.0/`). [97] Copyright 2021 The Authors, Advanced Intelligent Systems published by Wiley-VCH GmbH.*

2.8. Fibroblast contraction in soft scaffolds

In addition to secreting extracellular matrix proteins, fibroblasts are able to exert tensile forces in the form of contraction that plays an important role in wound healing upon injury as tissue lose their mechanical integrity. [31] The storage of tensile forces in the ECM has a significant contribution to macroscopic tissue tension. [148] As a non-contractile mammalian cell type, fibroblasts were employed as motor cells for biohybrid actuation in an ongoing and pioneering study that, to the author's best knowledge, has not been conducted before.

The work is based on exploiting the tensile forces exerted by fibroblasts on the underlying substrate and the ability to release those stresses after cell detachment by chemical cues such as trypsin or Accutase® that unbind focal adhesion points. The actin inhibitor jasplakinolide could be an alternative chemical cue that promotes aggregation of G-actin monomers and suppresses depolymerization of actin filaments. [149] However, one of the drawbacks in both approaches is that they function globally and lack any spatial or temporal control. Borowiak and Küllmer *et al.* [149] have successfully synthesized photoswitches for jasplakinolides that they called optojasps, which are a family of azobenzene-based small molecules that can provide direct optical control of actin cytoskeleton. Azobenzenes are photoswitches that change their diazene configuration upon UV irradiation (*trans* → *cis* at 390 nm) and at 470 nm (*cis* → *trans*) or thermal relaxation. This system allows direct spatiotemporal control at single-cell scale as jasplakinolide can be activated and deactivated by light pulses, which makes the process also reversible. Figure 2.27 a presents the idea schematically.
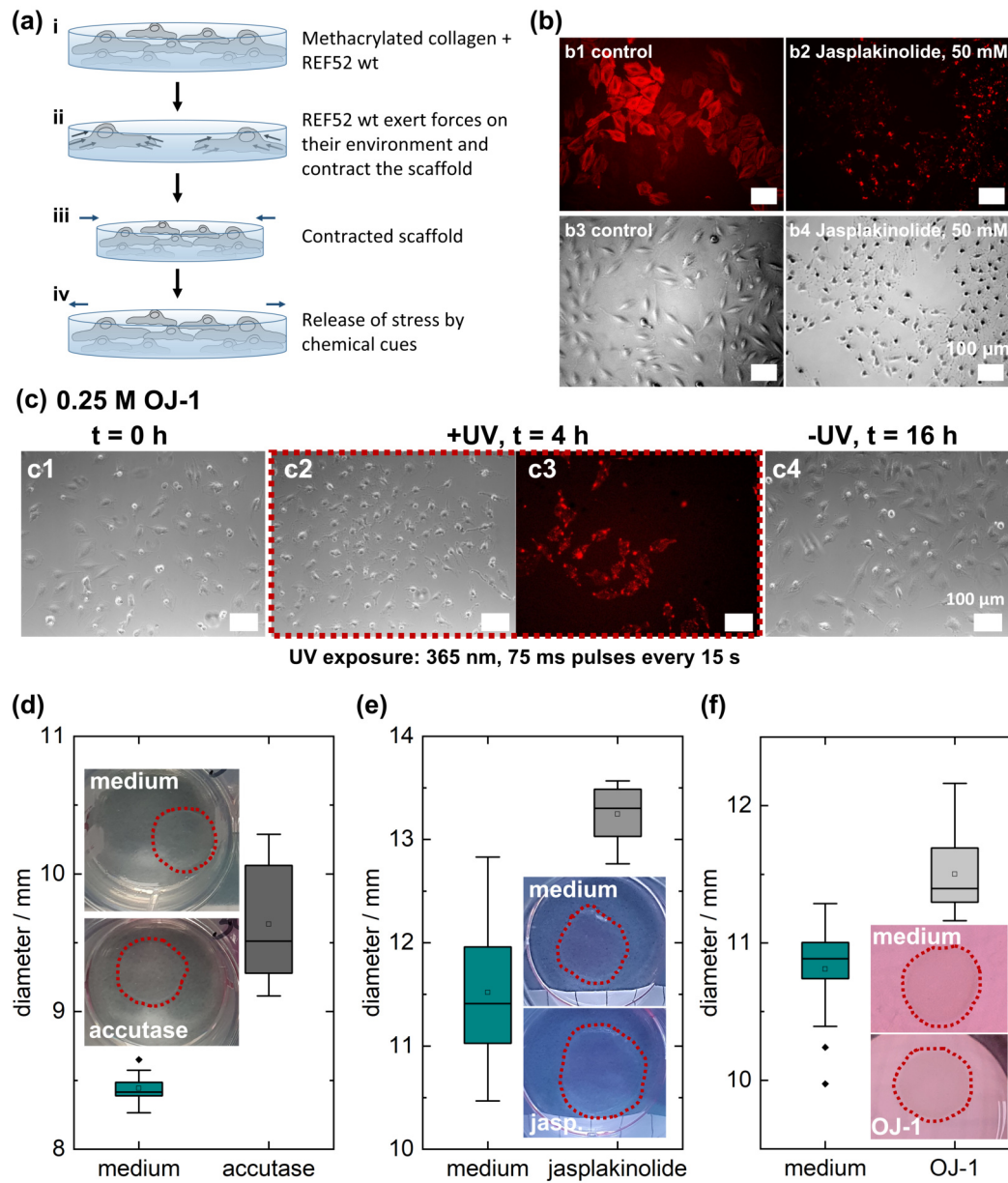
Figure 2.27. *a) Schematic of the idea of using fibroblasts for scaffold contraction. b) Influence of the actin inhibitor jasplakinolide on REF52 wt fibroblasts stained with SiR-actin. Cells in medium exhibit prominent stress fibers (b1, b3) whereas cells exposed to jasplakinolide showed aggregation of G-actin (b2, b4). c) Influence of optojasp-1 (OJ-1) on REF52 wt fibroblasts before (c1) and after expose to pulses of UV light (c2, c4) and after 12 hours in the dark (c3). d) Diameter of methacrylated collagen discs with incorporated REF52 wt fibroblasts when cultured in medium and after exposure to Accutase®, e) jasplakinolide (1 mmol L^{-1}) or f) OJ-1 (5 μmol L^{-1}; 4 h UV exposure, 75 ms pulses every 15 s).*

Fibroblasts (e.g., REF52 wt[24]) are incorporated in a very soft collagen matrix (i) and start over time to exert forces on their surroundings, which leads to scaffold contraction (ii and iii). When chemical cues (e.g., Accutase® or jasplakinolide) are applied, either the cell's focal adhesion points are detached from the matrix or the depolymerization and aggregation of actin filaments is promoted, which releases the stress on the matrix and allows the scaffold to expand again (iv). The effect of jasplakinolide on REF52wt cells is presented in Figure 2.27 b. REF52 wt fibroblast cells are stained with SiR-actin, a silicon-rhodamine (SiR) conjugate that is cell permeable and visualizes F-actin dynamics in living cells. [149] The cells are imaged before and 80 minutes after adding jasplakinolide with Cy5 filter units (b1, b2) and in phase contrast (b3, b4) on an inverted IX81 Olympus microscope. The chemicals and drugs (Jasplakinolide, SiR-actin and optojasp-1) used in this section were kindly provided by Prof. Hans-Dieter Arndt from Friedrich-Schiller-University Jena. Cells cultured on glass in normal culture medium[25] exhibit prominent stress fibers that span the cells (b1, b3). After adding jasplakinolide ($50\,\mathrm{nmol\,L^{-1}}$), the cells collapse due to aggregation of G-actin and formation of large actin aggregates, hence no stress fibers are visible (b2, b4). The same process can be observed when using optojasp-1 (OJ-1, $0.25\,\mathrm{mol\,L^{-1}}$), as shown in Figure 2.27 c. OJ-1 is added in the beginning of the experiment but shows no effect on the cells (c1) until illuminated with UV light ($\lambda = 365\,\mathrm{nm}$) in 75 ms long light pulses every 15 seconds for 4 h upon which azobenzene switches from $trans \rightarrow cis$ to induce actin polymerization into amorphous clumps in the cells. The cells were illuminated with UV light pulses instead of a constant illumination to avoid cell toxicity. [149] The illumination setup consists of an LED (from Sahlmann Photochemical solutions) that can be controlled via an Arduino Mega2560 and a customized software. After 4 hours, OJ-1 caused an increase of actin nucleation, resulting in actin aggregates formation (c2, c3) that led to a very similar cellular phenotype as caused by jasplakinolide (b2). After 12 hours, the OJ-1 switched back to the $trans$-state by thermal relaxation and the cells showed no abnormalities in the F-actin network anymore and recovered their stress fibers (c4). The REF52 wt fibroblast cell's ability to contract their surrounding was analyzed by incorporating fibroblasts in a methacrylated collagen matrix (ColMA; Advanced BioMatrix) under sterile conditions. ColMA was dissolved in acetic acid at a concentration of $4\,\mathrm{mg\,mL^{-1}}$ following the supplier's instruction and $1000\,\mathrm{\mu L}$ of ColMA solution was mixed with photoinitiator dissolved in PBS ($10.9\,\mathrm{\mu L}$ phenyl-2,4,6-trimethylbenzoyl-phosphinate, $1\,\mathrm{mg\,mL^{-1}}$) and $90\,\mathrm{\mu L}$ of neutralization solution (Advanced Biomatrix) then chilled on ice. A cell suspension containing approximately one million cells per milliliter was prepared and shortly chilled on ice, then added and mixed with the ColMA solution. 113 or $154\,\mathrm{\mu L}$ were placed on sterile coverslips with 12 or 14 mm diameter, respectively. The solution was then covered with

---

[24]REF52 wt cells were kindly provided by PD Dr. Dr. Ada Cavalcanti-Adam from the Max Planck Institute for Medical Research in Heidelberg.

[25]Dulbecco's modified Eagle's medium (DMEM) supplemented with 10 % fetal bovine serum (FBS) and 1 % penicillin/streptomycin.

a second coverslip to obtain collagen discs with approximately $1\,\mathrm{mm}$ height, followed by blue light irradiation ($405\,\mathrm{nm}$, $12\,\mathrm{mJ\,cm^{-2}}$). Afterwards, cell culture medium was added and the samples were stored at $37\,°\mathrm{C}$ for some time before carefully removing the coverslips. To measure the change in diameter, the medium was removed before images were taken (shown in insets in Figure 2.27 d - e) and the circumference of the collagen discs are highlighted by the red dashed line. The collagen samples appear in an imperfect circular shape and the diameter was measured using ImageJ by taking at least ten measurements in various directions of the disc to obtain an average value. To analyze the relaxation behavior of the collagen disc, Accutase® (d), jasplakinolide (e) and OJ-1 (f) were used to release the stresses exerted by cells. Samples were immersed completely in Accutase® for approx. $30\,\mathrm{minutes}$ or in jasplakinolide at $1\,\mathrm{mmol\,L^{-1}}$ concentration in cell culture medium for $2\,\mathrm{h}$, then imaged (see insets) to demonstrate a diameter change of approximately $12\,\%$ in both cases. As the drugs have to penetrate the collagen scaffold, higher concentrations were chosen than when cells were simply growing in 2D. OJ-1 was used at a concentration of $5\,\mathrm{\mu mol\,L^{-1}}$ and was activated by UV light ($\lambda = 365\,\mathrm{nm}$) for 4 hours in $75\,\mathrm{ms}$ long light pulses every 15 seconds to switch the azobenzene state from $trans \rightarrow cis$, which induced a change in diameter of approximately $6\,\%$ that is only half of what was achieved using Accutase® or jasplakinolide. This limited change might be due to the collagen matrix light absorption capacity or an insufficient illuminated area by the LED light source. Nevertheless, this approach shows suitability for application in biohybrid robotics with a potential to speed up the process using optojasps with faster kinetics. [149]

2.9. Conclusion and Perspective

In this chapter, I presented a highly versatile microengineering approach to prepare conductive hydrogels through incorporating an exfoliated graphene (EG) framework into a hydrogel matrix to generate conductive pathways that are pervading the hydrogel matrix similarly to an artificial nervous system. This method permits filler concentrations as low as $0.16\,\mathrm{vol\%}$ EG to yield an electrical conductivity as high as $0.34\,\mathrm{S\,m^{-1}}$ together with a negligible impact on the hydrogel matrix' mechanical integrity with a mere $10\,\%$ increase in Young's modulus. The results represent an unprecedented success in achieving that high level of conductivity with such a low filler material-to-hydrogel ratio compared to other state of the art attempts. The approach introduced here is very versatile and offers a great control over matrix size, shape, porosity, conductivity and mechanical behavior as well as the freedom to adjust matrix features through various means such as t-ZnO template density, infiltration number and conductive filler dispersion concentration. Also, it is possible to use other 1D or 2D nanomaterials such as reduced graphene oxide, CNTs, MXenes ($Ti_3C_2T_x$) or gold nanorods.

The functionality and beating behaviour of assorted contractile cell types such as mammalian skeletal muscle cells (C2C12) and cardiomyocytes derived from induced pluripo-

tent stem cells (iPSC-CM) were also tested on conductive hydrogels. To this end, biofunctional groups were incorporated into the matrix using combinations of PAM and GelMA hydrogel to activate cell binding through adhesion proteins that allowed for a good C2C12 cell spreading albeit an imperfect myotubes alignment, which could potentially be improved by a proposed scaffold microstructuring strategy. In contrast to C2C12, iPSC-CM illustrated ill-suited adhesion on GelMA-EG composites and thus requires a more suitable biofunctionalization technique. Yet, sufficient concentric contraction to deform the GelMA substrate a few micrometers, which translates to 5 % change in cell length was observed and thus can be potentially useful in biohybrid applications.

Taken together, the conductive hydrogels presented here promise a wide range of applications that spans bioelectronics and biosensing as well as biohybrid soft robotics and drug delivery, all of which can benefit from the interconnected channel system that promotes diffusion. This microchannel system is also advantageous for creating 3D cell scaffolds where vascularization for sufficient nutrient and oxygen transport is essential when exceeding scaffold thicknesses of 500 µm.

Furthermore, I demonstrated alternative hydrogel systems based on poly-N-isopropyl-acrylamide (PNIPAM), gelatin methacryloyl (GelMA) and combinations of GelMA and polyacrylamide. The thermoresponsive PNIPAM hydrogel is a prominent material in soft actuators despite its slow response rate and the relatively weak forces it can apply. This shortcoming was addressed through microengineering that significantly increased response rate and volume change even without employing conductive filler materials. In a perspective work, integrating these finding with added conductive fillers would enable heating up a hydrogel via applied electrical or light pulses instead of heating the whole hydrogel surrounding.

Finally, fibroblasts as a non-contractile mammalian cell type were employed in a novel study as motor cells for biohybrid actuation. Photoswitchable drug optojasps were exploited as means to release the tensile forces exerted by fibroblasts that generated a collagen scaffold contraction and result in a 6 % change in specimen diameter.

3 | Conductive, fibrous scaffolds for biohybrid applications

In this chapter, I present a fibrous, soft, conductive scaffold made from poly(3,4-ethylenedioxythiophene):polystyrene sulfonate (PEDOT:PSS) that is suitable for culturing contractile cells and as a scaffold material for biohybrid soft robotics. After an introduction to state of the art studies (Section 3.1), the fabrication method and material properties will be presented in Section 3.2. This will be followed by biofunctional studies (Section 3.3) including biocompatibility tests and the assessment of appropriate biofunctionalization with cell adhesion promoting motifs, which were tested with fibroblast and skeletal muscle cells (Section 3.4). The electrical stimulation of cells and the beating behavior of cardiomyocytes that are induced from pluripotent stem cells and rice fish are analyzed in Section 3.5.

3.1. State of the art

Nerve, cardiac and skeletal muscle cells rely on electrical signals to function and communicate among themselves, [8, 10, 136] so the electrical conductivity of artificial cell scaffolds is a prerequisite. [13] In biohybrid robotics where cardiac or skeletal muscle cells are often used, the scaffold is additionally required to be soft in order to accommodate for material actuation due to cell contraction yet strong enough to provide structural integrity to support the adhering cells. As cells demonstrate acute mechanosensitivity to their extracellular matrix, the scaffold material stiffness is an essential contributing factor. [13] Besides adding conductive filler materials to hydrogels as discussed in Chapter 2, another means to generate conductive cell scaffolds is through the use of intrinsically conductive polymers like poly(3,4-ethylenedioxythiophene):polystyrene sulfonate (PEDOT:PSS; Figure 3.1).

During polymerization, overlapping p-orbitals form π-bonds throughout the polymer backbone along which the charges are able to move by intra- and inter-chain charge transfer and hopping [1] and thus the freely moving π-electrons serve as mobile carriers. By doping with anions they counterbalance the positively-charged holes in the
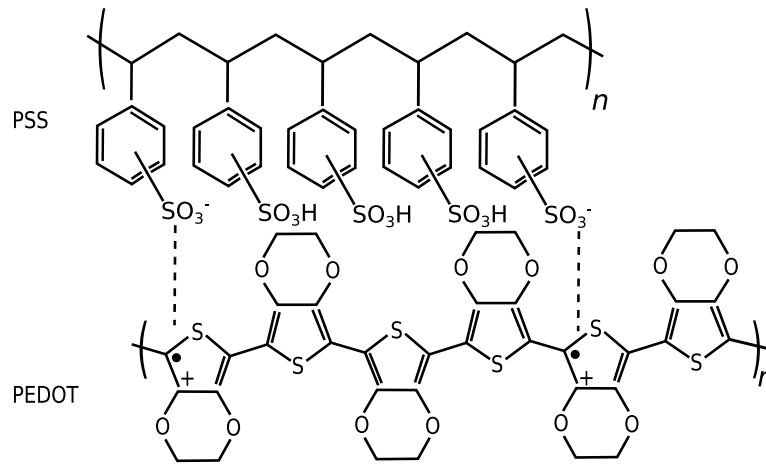
Figure 3.1. *Chemical structure of PEDOT:PSS. Adapted from [150].*

conjugated backbone chain of, e.g., PEDOT, which enables electrical conductivity. Hence, the dopant amount and the anion chemical nature determine the PEDOT physical and chemical properties. Polystyrenesulfonate (PSS) is a preferably used dopant for its chemically-inert polyanionic structure that enables water solubility and yields stable composites [151] of PEDOT:PSS (Figure 3.1) with a high conductivity ($4600\,S\,cm^{-1}$ [152]) achieved after further processing, like, e.g., the addition of organic solvents, acid or heat treatment. [153] PEDOT:PSS, which is used in this work, enables water dispersibility and provides a good electrical conductivity and hence, is used for organic electronic applications such as bioelectronic devices and biosensors. [154,155] PEDOT:PSS is furthermore a highly attractive polymer in cell scaffold research for its stability, conductivity [156] and cytocompatibility with various cell types [9,151,157,158] in addition to promoting cell adhesion and proliferation. [158] However, 3D scaffolds prepared with pure PEDOT:PSS rarely exist due to the PEDOT's inherent rigidity by virtue of its extended π-electron-system that renders the polymer brittle. [158] Dry $0.5\,mm$ thick PEDOT:PSS thin films have a very wide range of reported Young's moduli that begins from $9.3 \pm 0.7\,MPa$ [159] to between 0.9 and $2.9\,GPa$, [160] whereas $6.5\,GPa$ for air-dried fibers was reported. [161] PEDOT:PSS in a film form is commonly used as a conductive surface in 2D cell culture to, e.g., modulate the proliferation of human glioblastoma multiforme cells and human dermal fibroblasts, [151] although the stiffness is not compliant with human tissue stiffness ranges, especially not with electrically-excitable cells such as muscle or nerve cells. Still, electrically excitable PC12 neural cells cultured on PEDOT:PSS demonstrated enhanced cell differentiation [157] and higher neurite expression [9] whereas primary neurons showed long-term survival and growth. [162] Additionally, another common application for PEDOT:PSS is the use as a conductive filler material in hydrogels. Cardiomyogenic differentiation of human induced pluripotent stem cells on alginate-collagen hydrogels in the presence of PEDOT:PSS (conductivity of $0.35\,S\,m^{-1}$) was studied, e.g., by Roshanbinfar *et*

al. [14] and cells showed improved maturation and beating properties without external mechanical or electrical stimulation.

The brittle and hydrophobic nature as well as the high rigidity makes the preparation of 3D macroporous PEDOT:PSS scaffolds a great challenge. One strategy is the so-called ice-templating method, [156, 163, 164] where dispersions are frozen at -26 or -80 °C and subsequently lyophilized and afterwards annealed at elevated temperatures. Ice templating, or generally speaking freeze casting, is a common technique used for preparing 3D scaffolds not only from conductive polymers but also from hydrogels and a variety of other materials like ceramics, metals and biomacromolecules. [165] The scaffold final architecture in terms of porosity and pore morphology can be tuned by a number of chemical or physical parameters such as the solution composition, solvents used as well as freezing rate and temperature. Although this flexibility in procedure parameters renders the process versatile, alterations in process conditions may lead to drastic changes in scaffold microstructure as well. [164, 165] For example, Guex *et al.* [156] fabricated 3D PEDOT:PSS scaffolds with a pore diameter above 50 µm, a conductivity between $0.61 \, \mathrm{mS \, m^{-1}}$ and $14 \, \mathrm{mS \, m^{-1}}$ and an elastic modulus of 37 kPa (wet state) and 69 kPa (dry state) that is suitable for bone tissue engineering as evidenced by the osteogenic precursor cells (MC3T3-E1) differentiation into osteoblasts. Also, Wan *et al.* [164] generated macroscopic PEDOT:PSS scaffolds with pore sizes between 30 and 100 µm through the ice-templating method by varying freezing rate, crosslinker amount and PEDOT:PSS concentration to yield a 4.5 kPa elastic modulus measured in an aqueous environment. Moreover, PEDOT:PSS-based conductive scaffolds can also be used as a live-cell monitoring platform to analyze cell growth *in situ* by measuring the impedance that changes when cells are growing within the scaffold. [166] An additional 3D PEDOT:PSS scaffold prepared by freeze drying in combination with gelatin and bioactive glass showed 13 to 35 MPa Young's modulus, $0.17 \, \mathrm{mS \, m^{-1}}$ conductivity and around 60 % porosity with a 50 to 300 µm pore size. [163]

However, the fundamental shortcoming in all the above mentioned approaches is that the scaffold conductivity is much smaller than the DC conductivity of heart tissue ($0.1 \, \mathrm{S \, m^{-1}}$ [48]). In this work, I applied a microengineering method analogous to that addressed in Chapter 2 to generate reproducible scaffolds with a fibrous structure that resembles the cell's extracellular matrix while having a high specific conductivity of $22.6 \, \mathrm{S \, m^{-1}}$ even after two weeks of storage in water. The aero-PEDOT:PSS' Young's modulus is approximately 15 kPa when samples are immersed and measured in an aqueous environment.

3.2. Microengineered scaffold properties

Fibrous, conductive PEDOT:PSS scaffolds were successfully prepared using a similar strategy to the one introduced in Section 2.2 for fabricating microengineered conductive hydrogels that is based on employing a sacrificial template. The aero-PEDOT:PSS

preparation method was developed by Igor Barg in the group of Prof. Franz Faupel at Kiel University and the preparation procedure is schematically shown in Figure 3.2.
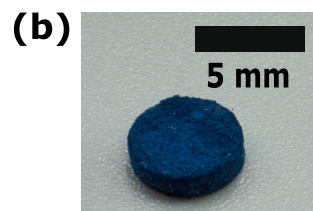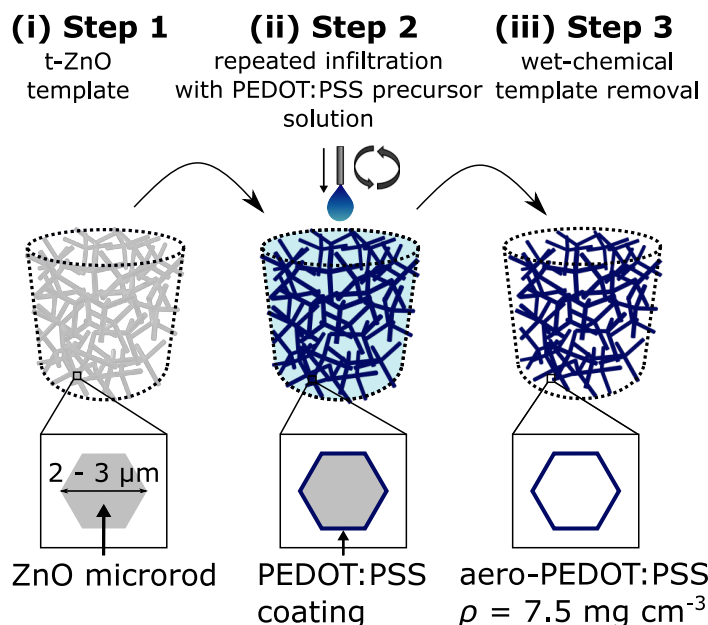
Figure 3.2. *Aero-PEDOT:PSS scaffold preparation and properties. a) Schematic presentation of the preparation route of fibrous, conductive PEDOT:PSS scaffolds. i) Highly porous t-ZnO template infiltrated with a PEDOT:PSS precursor dipersion. ii) Multiple repetitions of the process during which the solvent evaporates and the polymer crosslinks. iii) In the last step, the sacrificial t-ZnO template is removed by hydrochloric acid treatment to yield a fibrous aero-PEDOT:PSS structure with a 7.5 mg cm^{-3} density. Adapted from [115]. b) A fibrous PEDOT:PSS scaffold image with 37.7 S m^{-1} and 22.6 S m^{-1} specific conductivities measured in water shortly after preparation and after 14 days, respectively, and a 15 kPa Young's modulus in an aqueous environment.*

An aqueous PEDOT:PSS precursor dispersion that consists of PEDOT, PSS, divinyl sulfone (DVS; acts as a crosslinker), ethylene glycol and ethanol[1] was drop-cast onto highly porous tetrapodal zinc oxide (t-ZnO) templates to form a homogeneous polymer assembly on the ZnO arms. After repeating this process several times and allowing the solvent to evaporate at 55 °C for a period of time during which crosslinking was taking place, the ZnO template was eventually removed by a wet-chemical etching step with hydrochloric acid. An image of the resulting macroscopic sample termed aero-PEDOT:PSS is shown in Figure 3.2 b. The microstructure of the sacrificial t-ZnO template (Figure 3.3 a) and aero-PEDOT:PSS (b) was analyzed by scanning

---

[1]The chemical structure of aero-PEDOT:PSS is shown in Figure C.1.

electron microscopy. The aero-PEDOT:PSS' structure shows some sail formation of PEDOT:PSS between the tetrapod arms that is an effect arising from the assembly process of aqueous nanomaterial dispersion on the ZnO by means of water meniscus formation between ZnO arms during the drying process. [167]
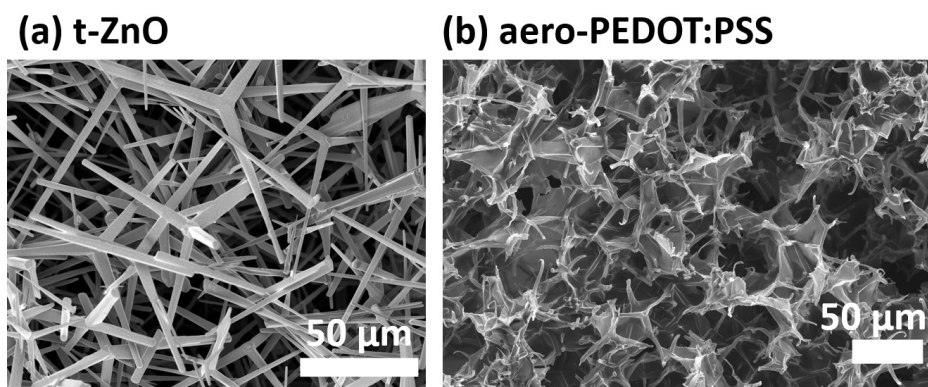
Figure 3.3. *Representative microstructure scanning electron micrographs of a) a t-ZnO template and b) aero-PEDOT:PSS.*

As a potential scaffold material in biohybrid soft robotics and for culturing electrically excitable cells, the samples Young's modulus measurements is prompted to be performed in an aqueous environment given the fact that PEDOT:PSS absorbs water and swells and thus changes its mechanical properties, [156] even though no swelling of the samples was observed. PEDOT:PSS is commonly used as a thin film with reported stiffness in the MPa and low GPa region, [159–161] which is not compliant with electrically excitable cells where a stiffness of a few tens kPa is necessary to mimic their natural ECM. The Young's modulus of aero-PEDOT:PSS samples with a $7.5\,\mathrm{mg\,cm^{-3}}$ density were measured in cyclic compression using a *ZwickRoell 2.5 kN Zwicki* equipped with a *Xforce P* 5 N force sensor. Prior to the test, the samples were stored in water for at least 24 h to ensure full swelling. The samples were compressed by 20 % with a $5\,\mathrm{mm\,min^{-1}}$ speed for 50 consecutive cycles and a 20 mN pre-load.[2] From the recorded force-distance curves, the stress σ and strain ϵ were calculated using the initial length l_0 and the samples cross section A_0 according to equation Equation (1.3) and Equation (1.4). A representative stress-strain curve is shown in Figure 3.4 a that displays a viscoelastic behaviour with a distinctive hysteresis to the initial cycle which might be attributed to the preconditioning phenomenon [135] as explained in Section 2.5. The Young's modulus E is defined as the elastic, reversible deformation during a tensile or compression test that can be deduced from the initial slope in a stress-strain curve and here was calculated by linear fitting the initial slope up to a 1 % compression strain mark for all 50 cycles (Figure 3.4 b). The Young's modulus drops drastically

---

[2]Compression tests were kindly performed by Dr. Mohammadreza Taale.

after the initial cycle but remains at a stable level after approximately 10 cycles. The Young's moduli of cycle 10 to 50 were averaged for every sample to result in an aero-PEDOT:PSS mean Young's modulus of $14.9 \pm 5.8\,\text{kPa}$ (Figure 3.4 b1) and thus making it an ideal candidate for cardiomyocytes or skeletal muscle cells culturing.
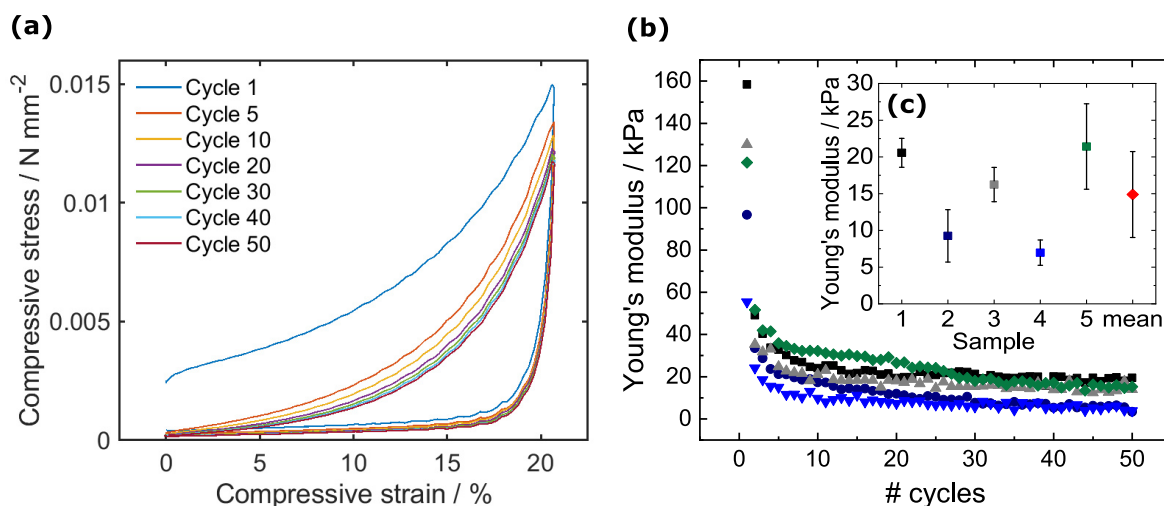
Figure 3.4. *Mechanical properties of aero-PEDOT:PSS samples measured in cyclic compression for 50 consecutive cycles up to 20 % strain. a) Representative cyclic stress-strain curve. b) Young's modulus determined with a linear fit to the slope up to 1 % strain for every cycle. After the first cycle the Young's modulus drops but remains stable after approx. 10 cycles. c) Mean Young's moduli averaged from cycle 10 to 50 for every sample that results in a $14.9 \pm 5.8\,\text{kPa}$ mean Young's modulus (red).*

The aero-PEDOT:PSS specific conductivity was measured in water using the two-point method presented in Section 2.4 that yielded an initial value of $37.7 \pm 6.9\,\text{S}\,\text{m}^{-1}$. The measurements and analysis were kindly done by Igor Barg from the group of Prof. Franz Faupel at Kiel University. After 7 and 14 days, the specific conductivity decreased to $24.2\,\text{S}\,\text{m}^{-1}$ and $22.6\,\text{S}\,\text{m}^{-1}$, respectively, which is four orders of magnitude larger than, to my knowledge, previously reported 3D PEDOT:PSS structures that showed maximum conductivities of $0.014\,\text{S}\,\text{m}^{-1}$. [156, 163] As aero-PEDOT:PSS demonstrates a conductivity that exceeds the $0.1\,\text{S}\,\text{m}^{-1}$ [48] heart tissue DC conductivity threshold, it is thus suitable for use with contractile cells. PEDOT:PSS thin films show conductivities as high as $4600\,\text{S}\,\text{cm}^{-1}$ [152], though they are highly dependent on the process, added solvents, temperature or morphology [156, 168]. The reduced conductivity in 3D structures can be explained by the scaffolds high porosity that leads to reduced accessible surface area and material thickness that are necessary for electricity transport. [156]

3.3. Biofunctional studies

In this section, the aero-PEDOT:PSS scaffold's suitability with various cell types was studied and the cytocompatibility using different biofunctionalization prospects was analyzed.

3.3.1. Biocompatibility tests

The cytotoxicity of fibrous aero-PEDOT:PSS scaffolds was determined by an indirect MTT extraction test that was performed following ISO-10993-5[3] and using rat embryonic fibroblasts (REF52 wt) as a model system (Figure 3.5). Culture medium served as a control and was set as 100 % cell viability. Undiluted extracts taken from aero-PEDOT:PSS samples showed a high cell viability of around 80 % that increased to around 90 % after decreasing the extract medium concentration to 30 %. The ISO norm regards samples with biocompatibility values above 70 % for undiluted extracts as biocompatible, thus aero-PEDOT:PSS can be employed as scaffold materials in cell culture.
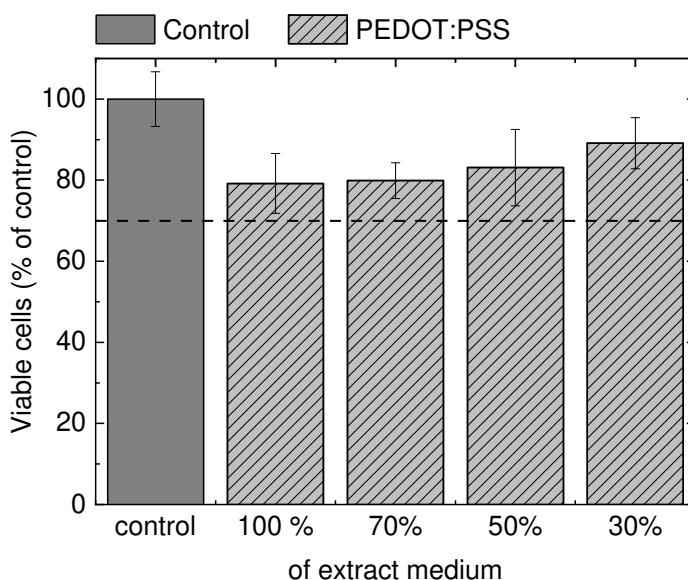
Figure 3.5. *Cell viability of rat embryonic fibroblasts (REF52 wt) exposed to medium extracts of PEDOT:PSS scaffolds determined with an indirect MTT extraction assay. Error bars depict standard deviation of three independent experiments each with N = 3. Dashed line marks a cell viability of 70 %.*

---

[3]Experimental details are provided in Appendix A.3.

3.3.2. Biofunctionalization of aero-PEDOT:PSS

The protein adsorption capacity of the PEDOT:PSS scaffolds was tested using bovine serum albumin (BSA) in a colorimetric detection assay with bicinchoninic acid (BCA; Thermo Scientific™ Pierce™ BCA Protein Assay Kit). PEDOT:PSS samples were incubated in $200\,\mu L$ bovine serum albumin solution (BSA, $2\,mg\,mL^{-1}$) for 5, 10 and 30 minutes and 1, 2, 4, 8 and 24 hours. Afterwards, the supernatant was removed, mixed with $200\,\mu L$ working reagent (Thermo Scientific™ Pierce™ BCA Protein Assay Kit) and then incubated for 30 minutes. Next, the protein concentration in the supernatant was quantified by absorbance measurements at $570\,nm$ (Epoch 2, BioTek) and then compared to a control (BSA solution, $2\,mg\,mL^{-1}$) tested without any sample. By subtracting the measured protein concentration from the $2\,mg\,mL^{-1}$ initial protein concentration, the protein amount that was adsorbed by the samples was calculated and is shown in Figure 3.6 a. The experiments have been kindly performed by Dr. Mohammadreza Taale. After 24 hours, about $1.3\,mg$ of protein ($\sim 66\,\%$ of protein present) was absorbed by the sample.
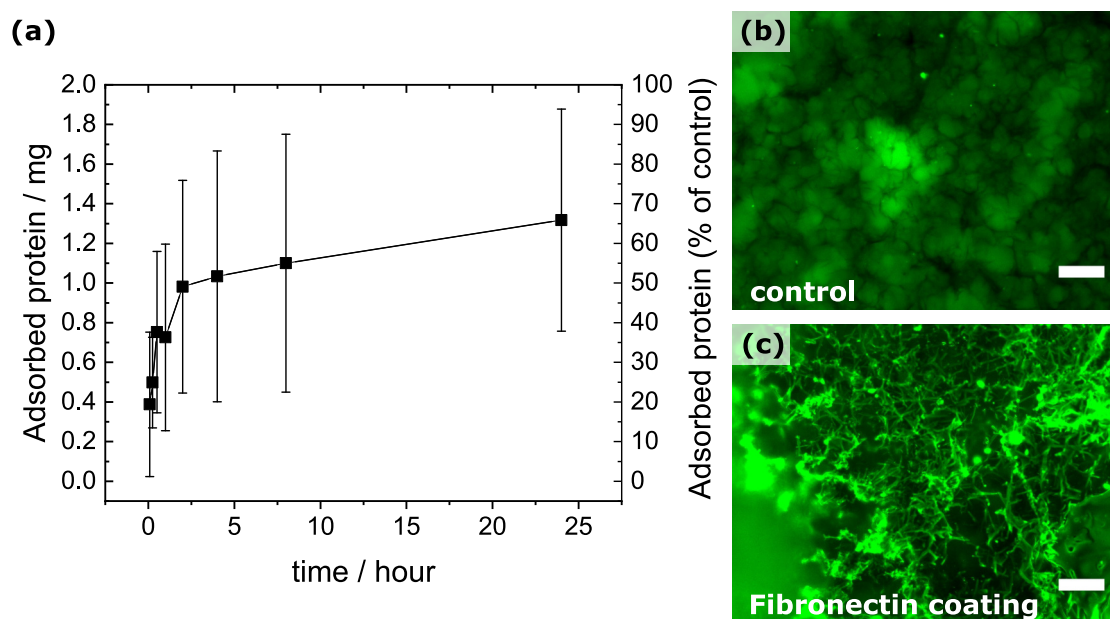
Figure 3.6. *Biofunctionalization of PEDOT:PSS. a) BSA adsorption by PEDOT:PSS scaffolds measured with a BCA colorimetric assay in three independent experiments each with 5 replicates. Error bars depict standard deviation. b, c) NHS-Fluorescein staining (green fluorescence) was used to visualize adsorbed proteins in PEDOT:PSS specimens. Samples were immersed in PBS (b) or in a fibronectin solution ($0.1\,mg\,mL^{-1}$ in PBS) (c) over night, stained, cut and then imaged using a GFP filter unit. c) shows a successful and homogeneous biofunctionalization with stained fibronectin of a sample's cross section.*

Proteins can bind to a biomaterial surface through van der Waals, hydrophobic or electrostatic forces. [158, 169] The PEDOT positive charge allows it to interact elec-

trostatically with the negatively charged PSS and due to the PEDOT's hydrophobic nature, it permits protein adsorption that improves significantly as was shown when mixing PEDOT in, e.g., alginate scaffolds. [158] For the aero-PEDOT:PSS used in this study, divinyl sulfone (DVS) was added as a crosslinking agent with the chemical structure shown in Figure C.1 in the appendix. Because the scaffold fabrication process requires an etching step with hydrochloric acid to eliminate the sacrificial t-ZnO template, parts of anionic PSS as well as its DVS crosslinked form were removed as confirmed by X-ray photon spectroscopy (XPS; XPS spectra shown in Appendix C.2). The PEDOT:PSS precursor solution initially had a ratio of 1:2.5 that decreased to 1:0.85 after the etching step, thus it is likely that the overall sample has a slightly positive net charge. Given the fact that BSA is negatively charged under physiological conditions by virtue of its isoelectric point that is around 4.7 [170], the high protein adsorption can potentially be influenced by local electrostatic interactions and other electrical charges present in the conjugated polymer. Fibronectin has a $-5.7\,\text{mV}$ ζ-potential [171] and thus carries a small net negative charge that enhances binding by electrostatic interaction and thus attributes to the good protein adsorption, which is why the samples were incubated in a fibronectin solution ($20\,\mu\text{g}$ fibronectin/sample) over night at $4\,°\text{C}$ for biofunctionalization.

To investigate the feasibility of this approach, *N*-hydroxysuccinimide-fluorescein (NHS-Fluorescein) was used in order to label the proteins as it reacts efficiently with primary amino groups and form stable amide bonds with *N*-hydroxysuccinimide released during the reaction. [172] PEDOT:PSS samples, incubated over night at $4\,°\text{C}$ in PBS with and without fibronectin, were washed with $50\,\text{mmol}\,\text{L}^{-1}$ borate buffer and then incubated in NHS-Fluorescein ($1\,\text{mg}\,\text{mL}^{-1}$ in DMSO) in $1\,\mu\text{L}\,\text{mL}^{-1}$ borate buffer concentration for 2 hours at room temperature. After a thorough wash with borate buffer, the samples were cross-sectioned and analyzed using an Olympus IX81 microscope with GFP filter unit and the results are shown in Figure 3.6. The control sample (Figure 3.6 b) shows no green fluorescence whereas the cross-sectioned sample that is incubated in fibronectin (c) demonstrate homogeneous staining. Hence, incubation in a fibronectin solution over night is sufficient to biofunctionalize the samples efficiently.

3.4. Cell adhesion and function

Rat embryonic fibroblasts (REF52 wt) adhesion and function were analyzed upon culturing on aero-PEDOT:PSS scaffold samples immersed in either a fibronectin solution ($20\,\mu\text{g}$/sample) or in cell culture medium supplemented with FBS (full medium) over night. Fibroblasts are the most common cells in the connective tissue and are essential for tissue development. They are responsible for secreting extracellular matrix (ECM) precursors and thus preserve the structural integrity of the connective tissue. [173] Fibroblasts were chosen as a model system in this work for their ability to create an ECM environment best suited to their function.

The aero-PEDOT:PSS samples were placed in transwells, $5 \cdot 10^4$ cells per scaffold were seeded and then cultured for 7 or 14 days before immunofluorescently staining[4] their actin filaments and nuclei as shown in Figure 3.7.
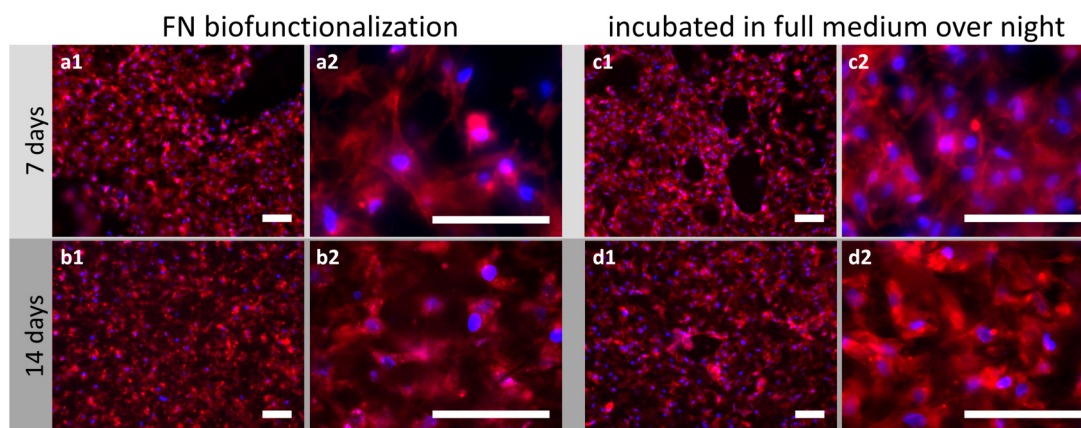
Figure 3.7. *REF52 wt on aero-PEDOT:PSS structures (50 000 cells/scaffold) functionalized with fibronectin (FN, 20 μg/sample, a, b image series) or incubated over night in full medium for biofunctionalization (c, d image series). The staining for nuclei (Hoechst, blue) and actin filaments (Phalloidin-Rhodamine, red) was done after 7 and 14 days. Scale bars: 100 μm.*

The figure shows that the cells demonstrated good adhesion, distinct actin stress fibers and an ability to span well between the PEDOT:PSS arms on all biofunctionalized and medium-incubated samples. Furthermore, the cells density appeared to grow higher after 14 days, which acutely indicate cell proliferation.

To study cell adhesion on PEDOT:PSS in more detail, the REF52 wt were additionally immunofluorescently stainedfor paxillin and zyxin (see Figure 3.8), which are proteins present in the focal adhesion clusters that regulate, e.g., mechanical force transmission to the extracellular matrix. [174] Images were acquired with an Nikon A1R confocal microscope and a z-stack (145 μm) projection is shown in Figure 3.8. The results show no noticeable difference between cells grown on biofunctionalized (Figure 3.8 a) or unfunctionalized (b) aero-PEDOT:PSS samples in terms of cell distribution (a1, b1) or actin stress fibers development (a2, b2). On both sample types, cells spanned between the PEDOT:PSS arms and were able to develop focal adhesion clusters, which elucidate a suitable adhesion to the substrate as indicated by the zyxin and paxillin expression (a3/4, b3/4). The similar cell adhesion and functionality on both biofunctionalized and unfunctionalized scaffolds confirm the PEDOT:PSS high protein adsorption capacity.

Moreover, the aero-PEDOT:PSS scaffolds biocompatibility was studied with **mouse skeletal muscle cells** (C2C12) as they can be used as actuators in biohybrid soft

---

[4]Experimental details are provided in Appendix A.4.2.
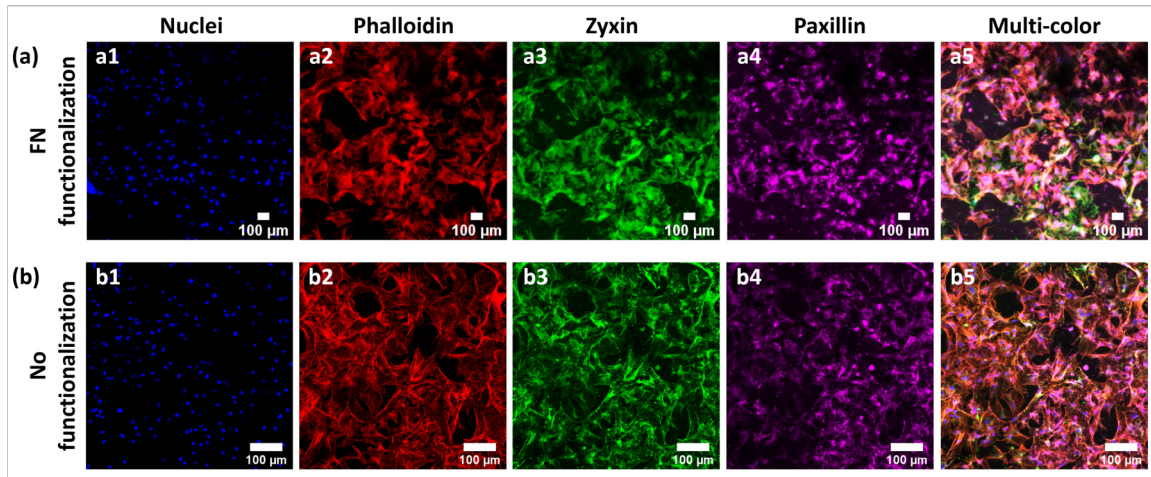
Figure 3.8. *REF52 wt on aero-PEDOT:PSS structures (150 000 cells/scaffold) a) biofunctionalized with fibronectin (FN, 20 µg/sample) or b) incubated in medium. Staining was done after 14 days for nuclei (Hoechst, blue), actin filaments (Phalloidin-Rhodamine, red), zyxin (green) and paxillin (violet).*

robotics when fused into myotubes, which are able to contract and exert forces on their surrounding matrix. Cell adhesion and myotube formation were examined using fluorescence imaging and scanning electron microscopy (SEM) (Figure 3.9) and the cell cytoskeleton structure was analyzed through immunofluorescence staining for the actin cytoskeleton, nuclei and myosin heavy chain (Figure 3.9 a). The results demonstrate skeletal muscle cell growth throughout the scaffold as well as steady spreading and adhesion that are accounted for by the apparent actin stress fibers development especially visible in Figure 3.9 a3. Myosin is expressed once myogenesis starts at the onset of myoblasts fusion into multi-nucleated myotubes and the development of the sarcomeric structure where myosin is widely present. This process typically starts three days after cells reach a sufficient confluency, which was not met yet in Figure 3.9 a2 and thus myosin is not expressed. Myoblasts grown for 14 days on aero-PEDOT:PSS scaffolds show high cell density (b1) and myotube formation (b2). Figure 3.9 b3 shows an overlay of b1 and b2 that is displayed in high magnification in (c). Myotube formation appears to be in a directed fashion on the surface of aero-PEDOT:PSS samples and is similar to those grown on a control sample, i.e., on cell culture plastic (Figure 3.9 e), except that the myotubes have spread shorter and thinner as compared in Table 3.1. Though, it has to be taken into account that imaging samples in 3D might result in projection errors due to myotubes growth in multiple layers, and as myotube formation depends on cell number and density, cells growing on a 2D control sample will predictably be longer and thicker than on a 3D aero-PEDOT:PSS.

Figure 3.9 d shows SEM images of myotubes forming on the surface (d1) and inside (d2) the fibrous structure of aero-PEDOT:PSS scaffolds after the sample was cut in
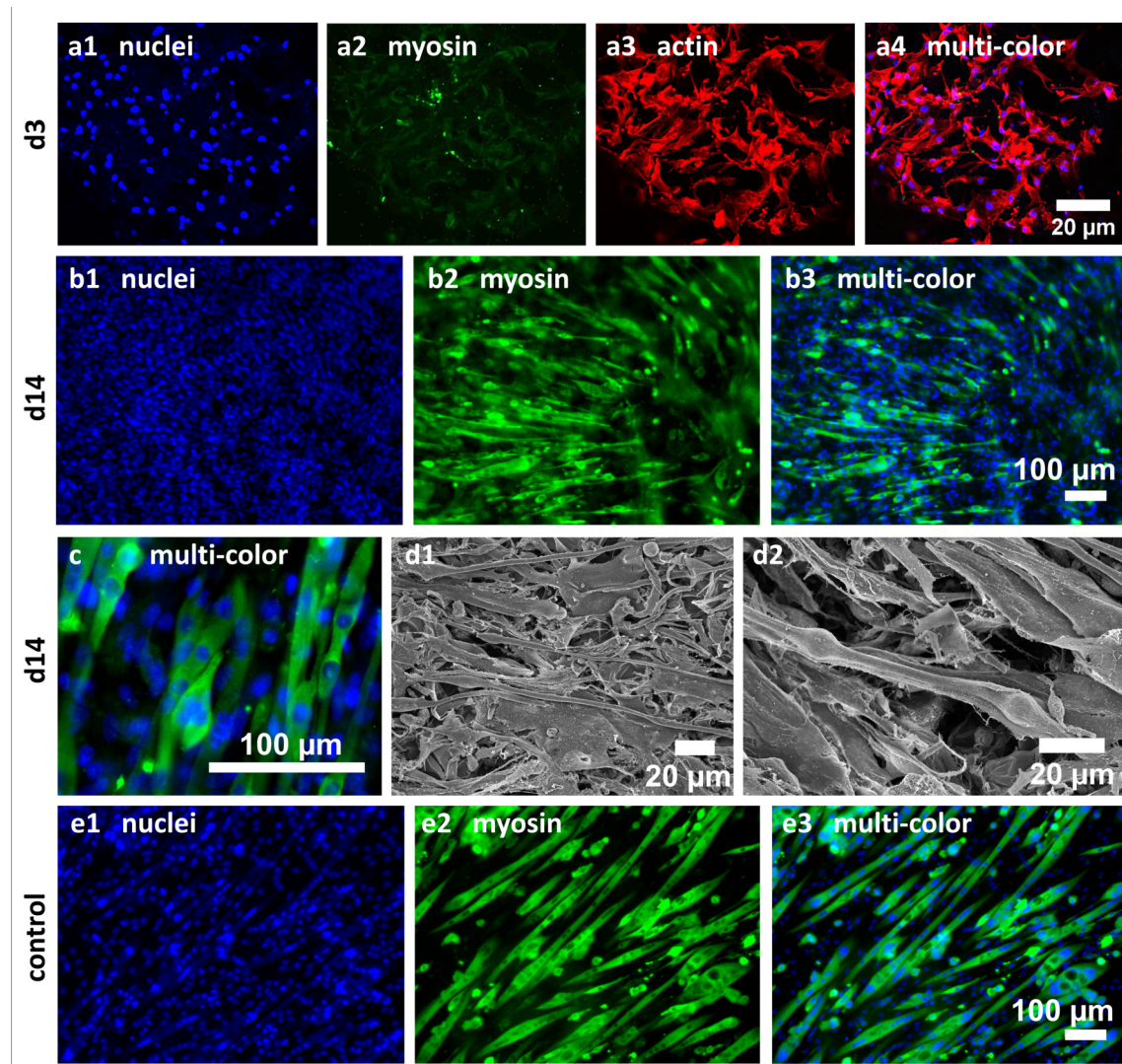
Figure 3.9. *Myotube formation of C2C12 skeletal muscle cells in aero-PEDOT:PSS scaffolds immunofluorescently stained for nuclei (Hoechst, blue), actin filaments (Phalloidin-Rhodamine, red) and myosin (anti-myosin heavy chain, green) Image series a) After 3 days, myoblasts were spreading with visible actin stress fibers (a3) but no sign of myogenesis and thus no myosin expression (a2). Image series b) After 14 days, myotubes have developed within the scaffold and shown in higher magnification in c). Image series d) SEM micrographs of myotubes formed after 14 days. Image series e) C2C12 skeletal muscle cells grown on cell culture plastic imaged after 14 days.*

half with more details demonstrated in Figure 3.10. To obtain the SEM micrographs, the cells in the scaffold were fixed with paraformaldehyde (PFA, 4 %, Sigma-Aldrich) for 20 minutes at room temperature followed by an ascending ethanol concentration sequence (50, 70, 80, 90, 95, 99 % ethanol, > 30 min time between each step) that is

Table 3.1. **Average length and thickness of myotubes grown for 14 days in fibronectin-functionalized aero-PEDOT:PSS or on cell culture plastic (Figure 3.9 b3, e3).**

	Length in µm	Thickness in µm
Aero-PEDOT:PSS	174.8 ± 49.2	15.9 ± 5.5
Control	256.1 ± 106.1	21.4 ± 6.2

necessary for the subsequent critical-point-drying process using an EMS 3000. Prior to SEM, the cells were coated with a thin sputtered gold layer (Bal-Tec SCD 050, 30 mA, 60 s). After 7 and 14 days of C2C12 myoblasts growth periods inside aero-PEDOT:PSS scaffolds, no distinct difference in myotube formation and adhesion is visible between aero-PEDOT:PSS samples incubated in fibronectin or in pure cell culture medium (Figure 3.10). Predictably, myotube formation has only taken place after 14 days and was not visible after 7 days as myoblasts were still not confluent enough to start myogenesis. The good cell adhesion of muscle cells to the PEDOT:PSS scaffold is highlighted in Figure 3.10 a2 and c3 and that cells are well spread is visible in c2 where a myoblast spans between the PEDOT:PSS arms.
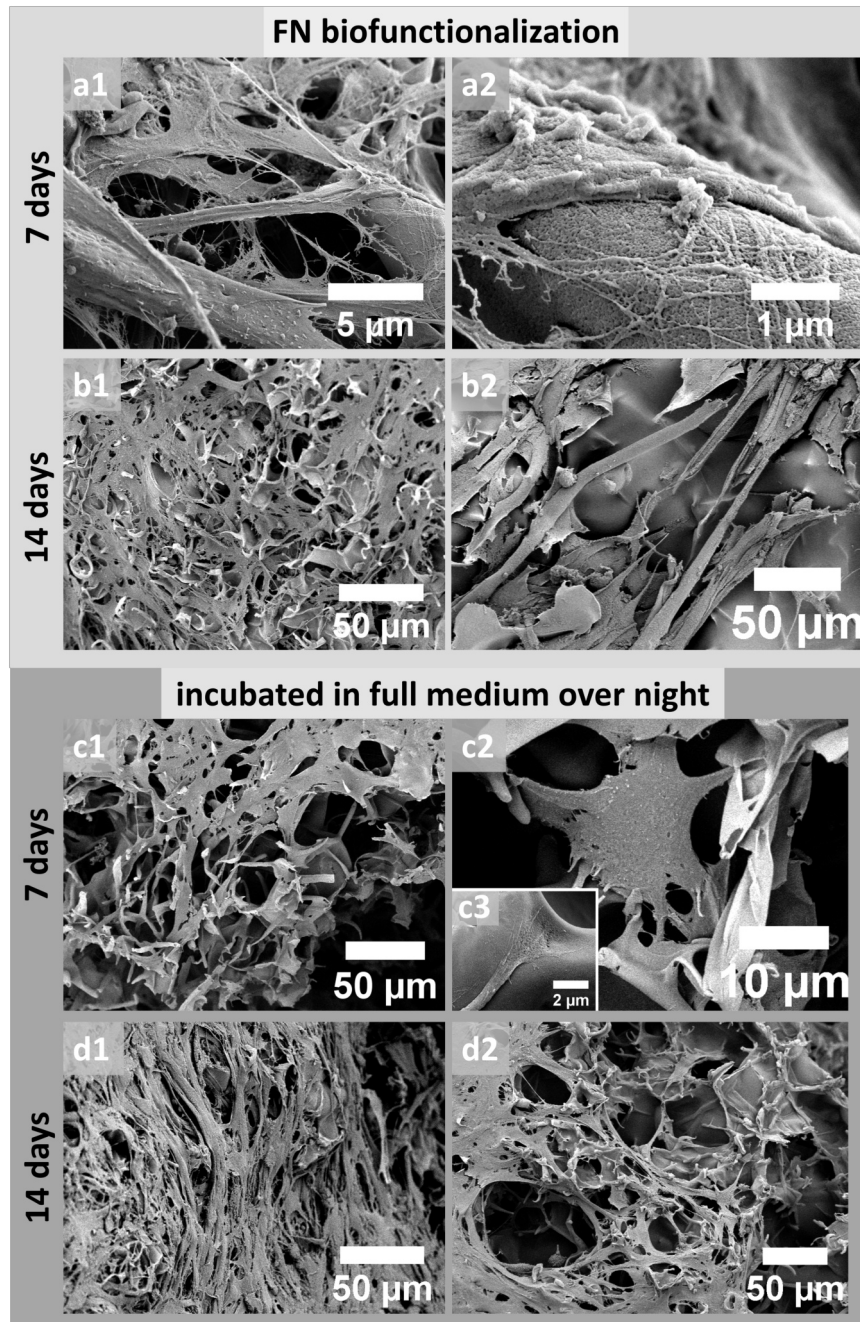
Figure 3.10. *SEM micrographs of C2C12 skeletal muscle cells grown for 7 and 14 days on a and b image series) fibronectin-biofunctionalized samples (FN, 20 µg/sample) or c and d image series) samples incubated in growth medium over night. Cells are well spread and show good adhesion to their substrates in both functionalization strategies, notably visible in a2 and c3. Myotube formation can be observed after 14 days of cell culture (b2, d1).*

3.5. Contractile cells on aero-PEDOT:PSS scaffolds

With an applicable conductivity of $22.6\,\mathrm{S\,m^{-1}}$ (after 14 days stored in water) and suitable mechanical properties with a $15\,\mathrm{kPa}$ Young's modulus in aqueous environment for contractile cells, aero-PEDOT:PSS is a promising structural material for use in biohybrid applications. The aero-PEDOT:PSS potential as a scaffold for contractile cells like cardiomyocytes is presented in this section. Cardiomyocytes derived from induced pluripotent stem cells (iPSC-CM) and whole heart tissue from rice fish are analyzed.

3.5.1. Electrical stimulation setup

External electrical stimulation is required to trigger skeletal muscle contraction or orchestrate a synchronized cardiomyocytes beating behavior if they form a monolayer within a scaffold. [44] The stimulation is provided by an electrical setup that consists of a small electric circuit ($1\,\mathrm{k\Omega}$ resistance, $220\,\mathrm{\mu F}$ capacitance in series), to prevent electrolysis by producing a signal with alternating polarity, and $1\,\mathrm{cm}$ wide electrodes with an interelectrode distance of $1\,\mathrm{cm}$ attached to a function generator (Rigol DG1022) as shown in Figure 3.11 a.
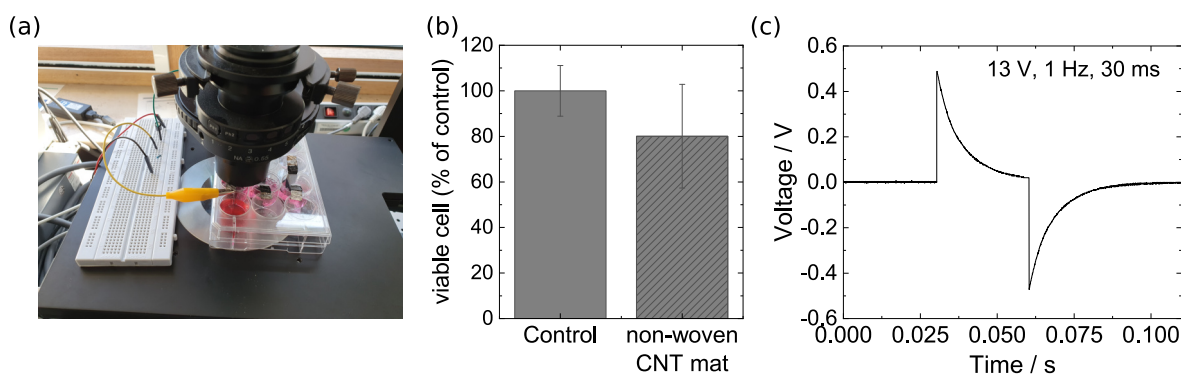
Figure 3.11. *a) The electrical stimulation setup combined with an inverted microscope. b) MTT extraction assay with REF52 wt cells of non-woven CNT mats. c) A characteristic single electrical pulse with 1 cm interelectrode distance with a 13 V, 1 Hz input signal and 30 ms pulse width measured in full cell culture medium.*

The electrodes made from non-woven carbon nanotubes (CNTs) mats[5] with a conductivity around $0.3 \cdot 10^5\,\mathrm{S\,m^{-1}}$[6] were inserted in the cell culture medium that in turn carries the electrical current by ionic conductivity. CNT mats are great electrode material candidates despite their conductivity is about two orders of magnitude lower than those of platinum, gold, copper or silver. CNT mats are cheaper than the other elements, do

---

[5]The non-woven CNT mats were kindly provided by the company Tortech Nano Fibers, Israel.
[6]Numbers provided by Tortech Nano Fibers.

not cause electrolysis [38] or pH change [175] as platinum does and they also do not share the copper and silver's drawbacks in having antibacterial [176] and cytotoxic [177] properties. The non-woven CNT mats were autoclaved while immersed in water prior to use and an MTT extraction assay with rat embryonic fibroblasts (REF52 wt) showed that the mats were suitable for use with cells (Figure 3.11 b). A characteristic pulse is shown in Figure 3.11 c measured with an oscilloscope (VOLTCRAFT DSO-1084E) in growth medium[7] with an input voltage of 13 V, 1 Hz and 30 ms pulse width, which results in an electrical field strength of approximately $0.5\,\mathrm{V\,cm^{-1}}$ as the electrodes are 1 cm apart from each other. The Dulbecco's modified Eagle's medium (DMEM) that was used for culturing, e.g., C2C12 skeletal muscle cells, has an approximately $1.5\,\mathrm{S\,m^{-1}}$ ionic conductivity. IPSC-CMs were cultured in RPMI-1640 medium with an ionic conductivity of approximately $1.4\,\mathrm{S\,m^{-1}}$. Both values were measured using a universal conductivity measuring cell (TetraCon® 325, WTW) and both are in good agreement with the $1.7\,\mathrm{S\,m^{-1}}$ DMEM electrical conductivity found in literature. [178] However, the media salt concentration is additionally affected by cell metabolites and fluid evaporation over time as well as by the addition of supplements like FBS or the B-27 supplement in the iPSC-CMs case that change the volume of the medium and in turn the salt ions concentration.

The C2C12 mouse myoblasts is a widely used contractile cell line that fuse into multi-nucleated myotubes under low serum conditions when the cell density is sufficiently high as explained in the previous section. Myoblasts were grown on normal cell culture plastic to a confluency stage at which the growth medium was exchanged to a starvation medium[8] and cells started to fuse into myotubes that were subsequently electrically-stimulated three days later. Although culturing skeletal myotubes on conductive substrates or scaffolds would be advantageous, this setup is ideal for electrically stimulating the cells to trigger their contraction when grown on cell culture plastic as can be deduced from their response to the stimulus in Figure 3.12. Figures a1 and a2 show myotubes at two different time points during a contraction after stimulation by pulsed square waves with 10 V, 1 Hz and 30 ms pulse width and $0.5\,\mathrm{V\,cm^{-1}}$ electrical field strength. To examine the change between the two stages, the two images were subtracted from each other using the Image Calculator function in the ImageJ software [146] to excerpt the difference (shown in a3) that was then superimposed onto the original image (a4) to elucidate the transformation (displayed in cyan color) upon contraction. The myotubes changed their length by approximately 0.88 µm and their thickness by approximately 0.96 µm upon a single contraction.

To quantitatively study cellular behavior after electrical stimulation, the cells contraction frequency was analyzed using a Python [9] script where the Fast Fourier Transfor-

---

[7]Dulbecco's modified Eagle's medium (DMEM) supplemented with 10 % fetal bovine serum (FBS) and 1 % Penicillin/Streptomycin.

[8]DMEM supplemented with 2 % FBS for starvation medium and 1 % Penicillin/Streptomycin.

[9]Python programming language: Python Software Foundation, `https://www.python.org/`.
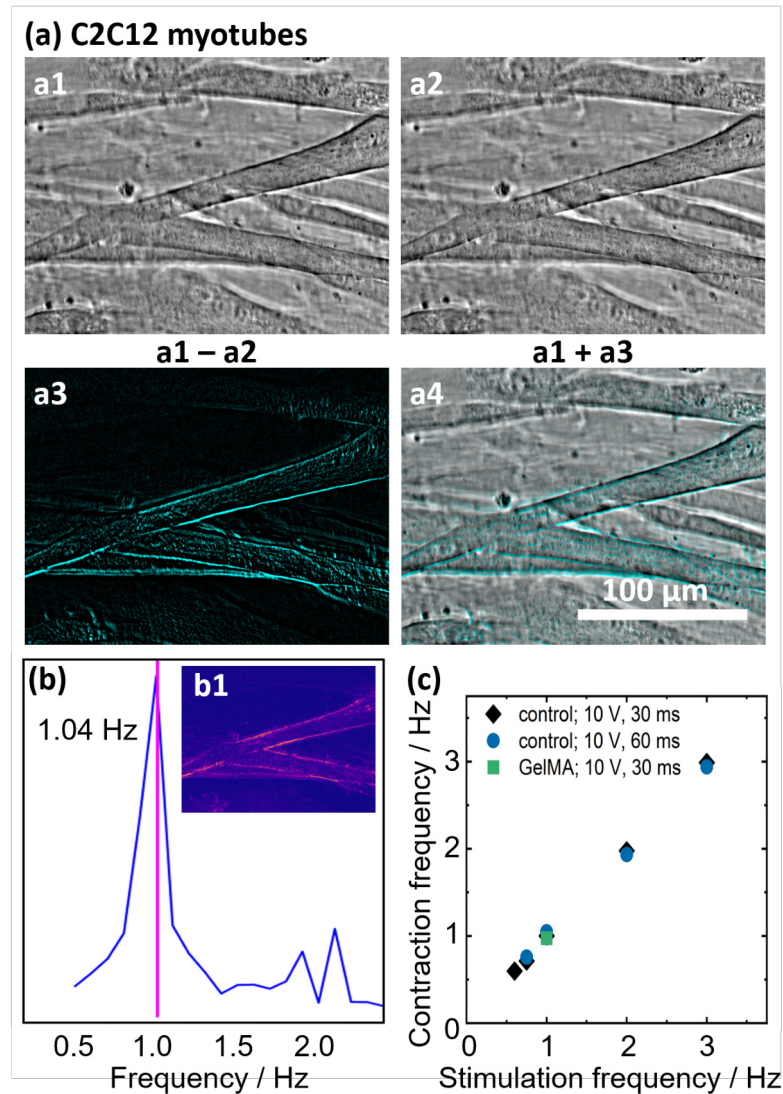
Figure 3.12. *C2C12 cells grown on cell culture plastic 3 days after changing to starvation medium and electrically stimulated with different frequencies (10 V, 30 ms or 60 ms pulse width). a1, a2) show C2C12 myotubes at two different time points during a contraction (electrically stimulated with 10 V, 1 Hz, 30 ms). a3) shows the difference between the images in a1 and a2. The change in length of the myotube is approx. 0.88 μm, the thickness changes by 0.96 μm. a4) shows an overlay highlighting the changes (turquoise) during a contraction. b) Exemplary result of Fast Fourier transformation analysis of the beating frequency of C2C12 myotubes. The resonance frequency is 1.04 Hz. In b1) active areas at this specific frequency are visible. c) Contraction frequency of C2C12 myotubes vs stimulation frequency for different electrical stimulation settings and on different substrates.*

mation (FFT) algorithm (numpy.fft) was employed. FFT is an algorithm used for an efficient computation of the Discrete Fourier transform (DFT) that functions by sepa-

rating the frequency component from a discrete-time signal to yield a spectrum similar to the example shown in Figure 3.12 b. In that spectrum, the peak is at 1.04 Hz and the areas where the contraction at that frequency took place are highlighted in inset b1. The results illustrate that myotubes contraction frequency corresponds with the electrical stimulation frequency as shown in Figure 3.12 c. The contraction and stimulation frequencies are directly proportional when frequencies up to 3 Hz were applied regardless of pulse width or the substrate used (GelMA or cell culture plastic in this study) that is in agreement with previous works published. [38, 179]

3.5.2. Induced pluripotent stem cell derived cardiomyocytes

In contrast to skeletal muscle cells, cardiomyocytes need no specific alignment on the scaffold surface and necessitate no electrical stimulation by virtue of their spontaneous contraction. However, a cardiomyocyte cell line able to generate high enough forces is not commercially available, [13] hence primary neonatal cardiomyocytes are commonly used, albeit animals are sacrificed and ethical questions are raised. Therefore, induced pluripotent stem cells (iPSCs) represent a good alternative as they are donated by patients to then be differentiated into cardiomyocytes, a time-consuming yet valuable process to prepare cardiomyocytes (iPSC-CM) with all original features. Cardiomyocytes derived from induced pluripotent stem cells (iPSC-CMs) and their culturing media were kindly provided by Dr. Ayca Seyhan Agircan and Prof. Dr. Johannes Backs from Heidelberg University Hospital. 6 mm in diameter and 0.5 - 1 mm in height circular aero-PEDOT:PSS samples were incubated in fibronectin solution (20 µg/sample) over night and then fixed with sterile needles to transwell bottoms to prevent them from floating while the cell suspension was carefully poured on top to ensure a high cell density of approximately $3 \cdot 10^5$ cells per sample. 48 hours later, cells were fixed with 4 % paraformaldehyde and the cytoskeleton structure was evaluated by immunofluorescent staining of the nuclei (blue), actin filaments (red) and myosin (green) as shown in Figure 3.13. The cardiomyocytes show good distribution throughout the aero-PEDOT:PSS sample as depicted in the overview images in Figure 3.13 a and figures b and c display individual cardiomyocytes and their actin and myosin filaments in different magnifications where the cells are spreading and extending well within the scaffold. The lateral boundaries of each sarcomere and the smallest contractile unit of cardiomyocytes (also known as Z-bands) are illustrated and marked with white arrows in the confocal microscopy images in Figure 3.13 d.

Figure 3.13 e shows the various shapes and clear actin filament expression of cardiomyocytes seeded on fibronectin-coated glass with no apparent difference to those cultured on PEDOT:PSS in appearance or morphology of the sarcomeric structure, myofibers organization and actin stress fibers as emphasized in higher magnification in Figure 3.14. The contraction course analysis of individual iPSCs growing in aero-PEDOT:PSS is shown in Figure 3.15 and was analyzed using FFT analysis as presented in Section 3.5.1. Cells in aero-PEDOT:PSS scaffolds were beating with around 0.7 Hz. Figures a1 and
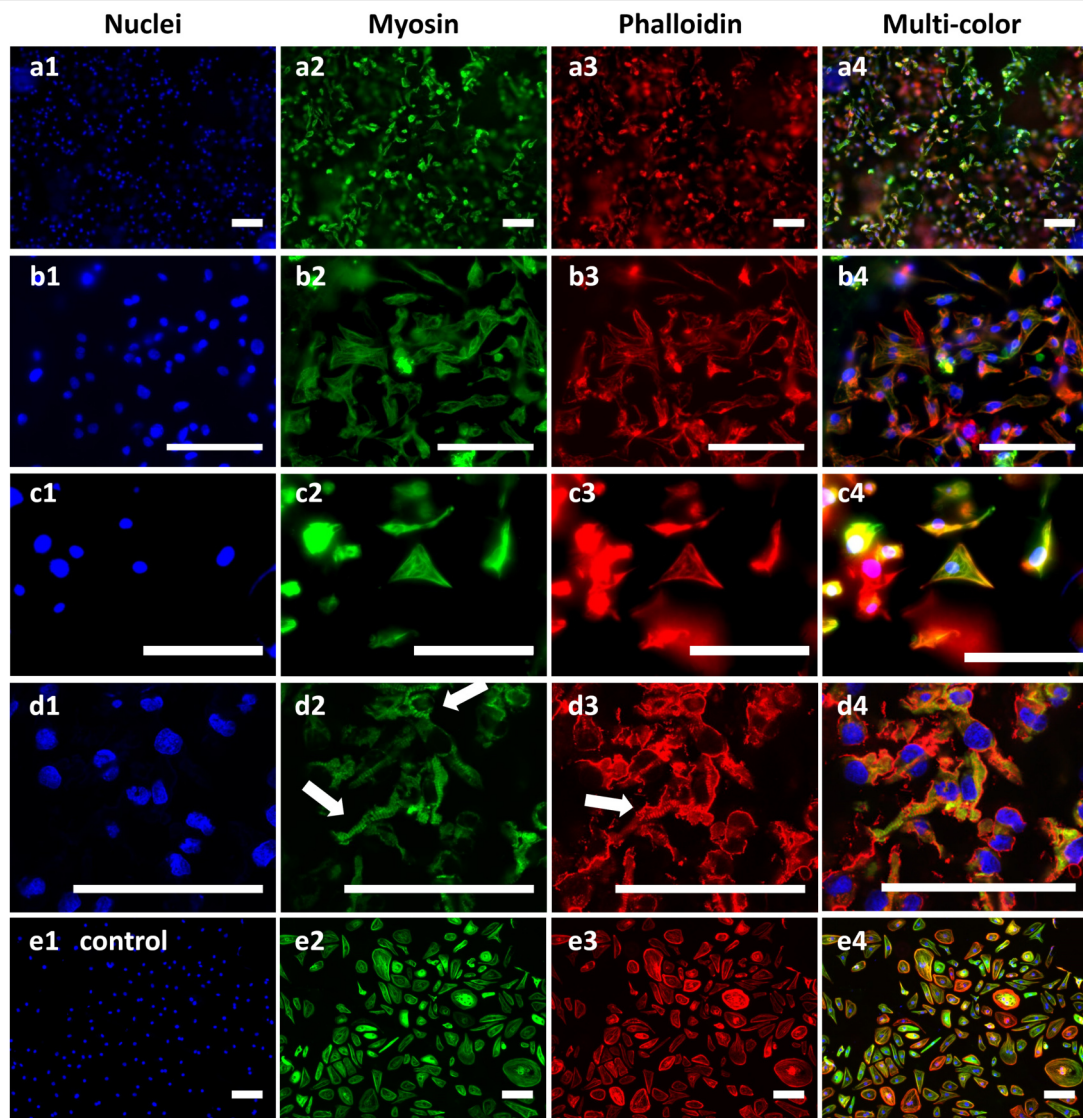
Figure 3.13. *Cardiomyocytes in aero-PEDOT:PSS scaffolds immunofluorescently stained for nuclei (Hoechst, blue), actin filaments (Phalloidin-Rhodamine, red) and myosin (anti-myosin heavy chain, green). Image series a) Overview of cardiomyocyte distribution in the aero-PEDOT:PSS scaffolds. Image series b) Cardiomcyoytes showing different shapes while spanning the PEDOT:PSS arms, especially visible in image series c. Image series d) Confocal microscopy images depicting the Z-bands in cardiomyocytes as highlighted by the white arrows. Image series e) Cardiomyocytes grown on fibronectin-coated glass substrates. Scale bars: 100 μm.*

a2 show the beating behaviour at two different time points during a contraction and the change that took place during this time period is projected in a3, which in turn is superimposed onto the original image (a1) to elucidate the transformation (displayed

in cyan color) upon cell contraction (a4). A similar analysis procedure was followed for image series b and c in Figure 3.15. As already shown in Section 2.6.3, cardiomyocytes cultured on plastic or glass substrates show isometric contraction, i.e., no change in their length during a contraction as seen in Figure 3.15 c, whereas cardiomyocytes in aero-PEDOT:PSS are able to perform concentric contractions and cause a deformation of their surrounding (a, b).
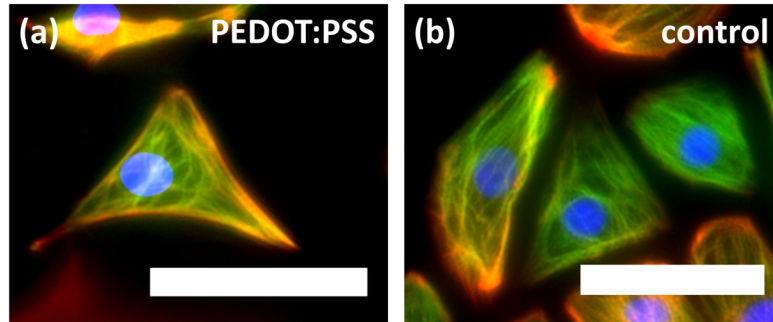
Figure 3.14. *Single cardiomyocytes immunofluorescently stained for nuclei (Hoechst, blue), actin filaments (Phalloidin-Rhodamine, red) and myosin (anti-myosin heavy chain, green) in a) aero-PEDOT:PSS scaffold and b) cultured on a glass substrate. Scale bars: 50 μm.*

A more detailed macroscopic analysis of cardiomyocyte-induced scaffold contraction is shown in Figure 3.16. In figure series a, the deformation of a large part of the aero-PEDOT:PSS scaffold during a cell contraction is expressed using a comparable analysis method to that presented above, whereas b shows the change upon contraction at the scaffold boarder. To quantify scaffold deformation caused by cells contraction, the thickness of multiple red lines (marked exemplary with white arrows) in b that resemble material displacement during a two-beats interval was analyzed using the ImageJ software for three different samples with approximately 30 measurements taken per specimen. The results show that the cardiomyocytes induced an approximately 4.3 μm deformation at the edge of the aero-PEDOT:PSS scaffold as shown in figure c. As a comparison to these values, iPSC cardiomyocytes cultured on 2D GelMA substrates deformed their underlaying material by approximately 2.5 μm (cf. Section 2.6.3), which therefore makes the aero-PEDOT:PSS fibrous structure more favorable for cells due to the ease of deformation.

Biohybrid robots reported in literature are almost exclusively based on 2D scaffolds and rely on sheets of contractile cells for actuation. One of the prominent examples is the mimicry of the batoid fish shape by Shin *et al.* [21] who used a 10 μm thick hierarchically-structured hydrogel scaffold with an incorporated flexible gold micro-electrode array seeded with a cardiomyocyte cell layer for actuation. Another example is the culturing of optogenetically modified primary cardiomyocytes on structured poly(dimethylsiloxane) (PDMS) thin films that encloses a microfabricated gold skeleton in the shape of a tissue-engineered ray with a maximum PDMS backbone thickness
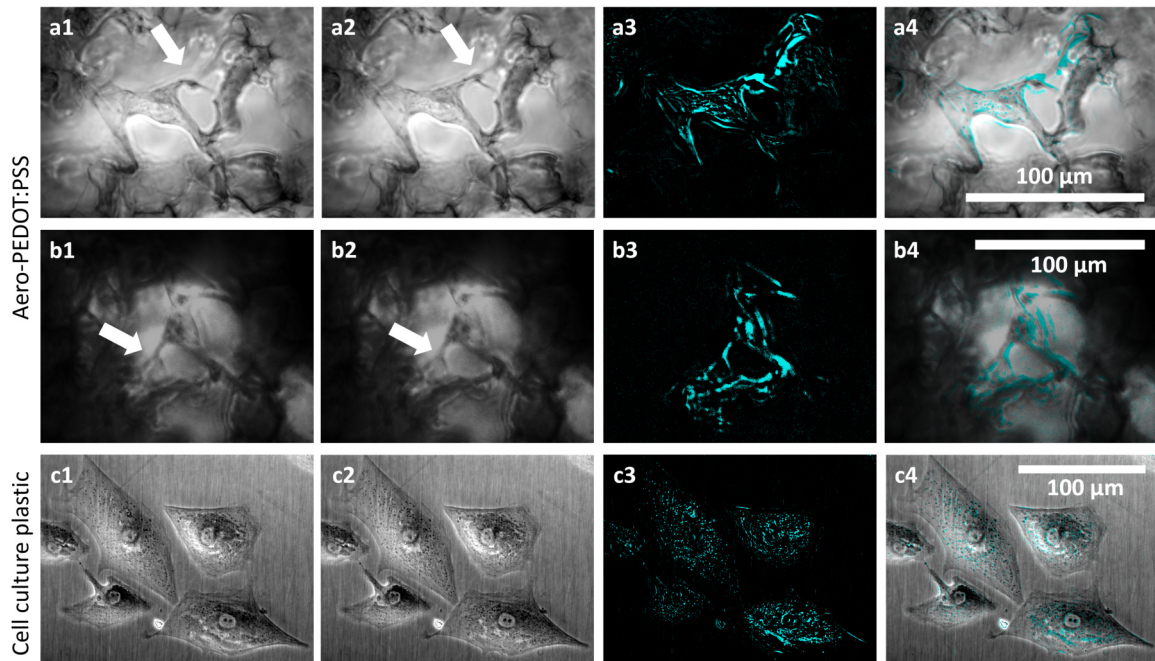
Figure 3.15. *Contraction of individual cardiomyocytes cultured in aero-PEDOT:PSS (a and b image series) and on cell culture plastic (c image series) as a control. a1, a2, b1, b2, c1, c2) Cells at two different time points during a contraction. The white arrows in image series a and b) highlight areas where contraction is particularly visible. a3, b3, c3) The subtraction of images 1 and 2 in their respective image series. a4, b4, c4) Overlay of images 1 with 3 in the respective image series that highlights the changes (cyan) during a contraction. Cells on cell culture plastic show isometric contraction, i.e., no change in their length during a contraction, whereas cells in aero-PEDOT:PSS show concentric contraction that causes a deformation of their surrounding.*

of 28 µm. The same group also presented an autonomously swimming biohybrid fish powered by a bilayer of cardiomyocytes seeded on both sides of a 200 µm thick structured hydrogel. 3D attempts involved the use of whole muscle tissue for actuation as for instance the dorsal vessel tissue of insects [13], engineered skeletal muscle strips [23] and neuromuscular tissue circuits from marine sea slugs [34]. Although the culturing of single cells in 3D scaffolds was reported in tissue engineering, [15,50] it has not been explored in the field of biohybrid robotics. In a breakthrough, Noor *et al.* [17] 3D-printed a thick vascularized, perfusable heart tissue with a natural architecture where iPSC-CM at a concentration higher than 10^8 cells mL^{-1} were directly printed within the structure, however neither an apparent tissue contraction nor blood pumping was achieved. Although lacking a quantitative analysis, the work of Noor *et al.* also illustrated that macroscopic contraction of cardiac patches with vacscularization requires an extremely high number of cells. Hence, increasing the number of cardiomyocytes in the scaffold and enhancing the cell beating synchronization would perspectively make
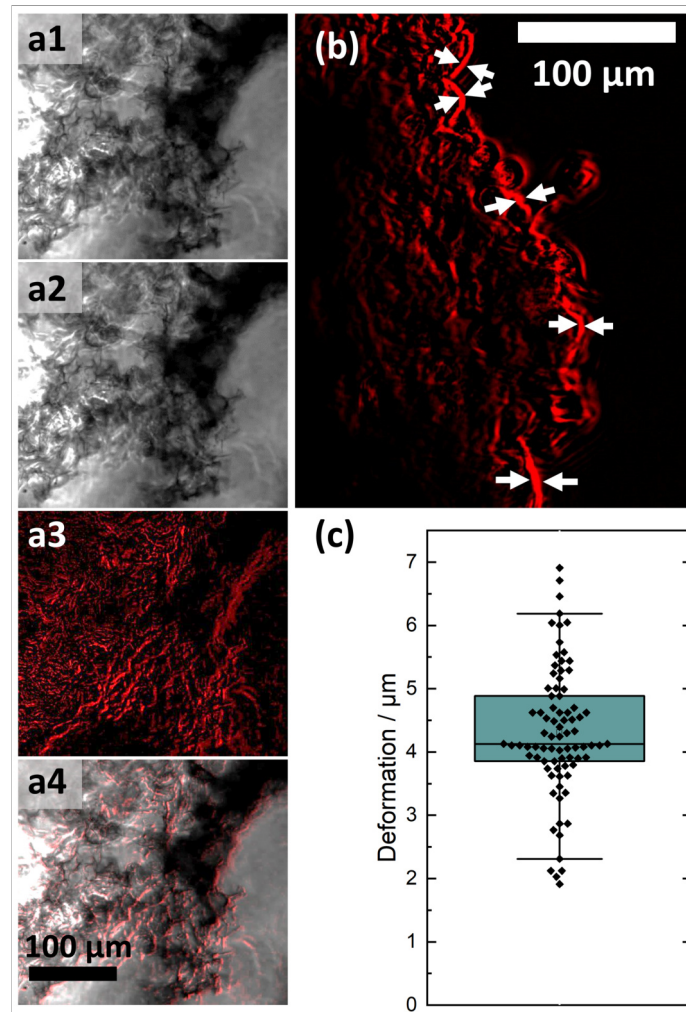
Figure 3.16. *Contraction of cardiomyocytes cultured in aero-PEDOT:PSS. a1 and a2) The scaffold deformed by cells at two different time points during a contraction. a3) Subtraction of a2 from a1. a4) Overlay of a1 with a3, highlighting the changes (red) during a contraction. b) The difference between two contractions at the boarder of an aero-PEDOT:PSS scaffold is represented by the thickness of the red lines. c) The line thicknesses (marked exemplary with white arrows in b) measurements for three different samples showing around 4.3 µm average deformation.*

macroscopic contraction attainable. Cardiomyocytes grown on fibronectin-coated glass slides showed no noticeable reaction to electrical stimulation. This might be attributed to the low cells density that was not enough to transfer cell-to-cell signals with the lack of a conductive substrate that caused a synchronization hindrance. [13] Similarly, cardiomyocytes grown in aero-PEDOT:PSS scaffolds showed no significant reaction to electrical stimulation as well, which might be due to an insufficient ionic conductivity of the cell culture medium to transfer the electrical signals and induce electrical stimu-

lation in the cells. The RPMI-1640 medium showed adequate conductivity of approximately $1.4\,\mathrm{S\,m^{-1}}$, however the salt concentration in the media is additionally affected by cell metabolites, fluid evaporation over time and the addition of supplements like B-27 that changes the medium volume and consequently the salt ions concentration. Therefore, the triggering signal was possibly too weak to induce sufficient electrical stimulation in the cells in these experiments. A higher stimulation signal can be obtained by a greater applied voltage, but this can cause a local increase in temperature that impacts cell viability. A more synchronized beating would lead to an increase in cell force and thus to higher deformation capabilities, hence this should be the focus of future studies. Despite the limited, microscopic-level of achievable deformation, my results represent a stepping stone in the field of 3D scaffolds for biohybrid soft robotics.

3.5.3. Fish hearts from medaka

One promising alternative animal source especially for primary cells are cardiomyocytes isolated from zebrafish (*Danio rerio*) or Japanese rice fish (also known as medaka; *Oryzias latipes*) embryos. Fish embryos are considered a replacement or refinement method according to the 3Rs (replacement, reduction and refinement) of animal experiments as they are likely to experience no suffering, distress or lasting harm at these development stages. [180] Early-life stages of fish are not protected as animals until being capable of independent feeding which is $120\,\mathrm{h}$ post fertilization[10] and are thus not falling into the regulatory framework when employed for animal experiments. [181] Furthermore, not only the breeding time and cell development for these fish are faster than in mammals, they also keep their functionality at a 10 to $40\,^{\circ}\mathrm{C}$ temperature range [182], thus enable biohybrid actuators operation should they be used at room temperature.

Medaka rice fish hearts were isolated by Dr. Thomas Thumberger from the group of Prof. Jochen Wittbrodt at the Center of Organismal Studies (COS) in Heidelberg University. The isolated hearts were reanimated by electrical stimulation (pulse square signals, $15\,\mathrm{V}$, $10\,\mathrm{Hz}$, $50\,\mathrm{ms}$) while placed in complete cell culture medium (DMEM supplemented with $10\,\%$ FBS and $1\,\%$ Penicillin/Streptomycin) and subsequently glued to PEDOT:PSS samples using a superglue (Figure 3.17).

In this proof-of-principle study, a whole heart tissue was opted for in order to ensure that a sufficient number of cells are available for prompting contraction and to allow the influence of stimulation to be easily visible. A piece of aero-PEDOT:PSS glued to a whole beating heart at a frequency of $1.4\,\mathrm{Hz}$ was observed rotating 90°(Figure 3.17 a-c) within a minute. The resonant beating frequency was determined using a video analysis with FFT functions and the resulting frequency spectrum is shown in Figure 3.17 d where the $1.4\,\mathrm{Hz}$ peak is marked with a pink line. The inset in d illustrates the area

---

[10]According to the EU Directive 2010/63/EU on the protection of animals used for scientific purposes.

where contraction at this frequency took place. This finding demonstrates a first macroscopic biohybrid actuator that represents a significant stepping stone for future studies.
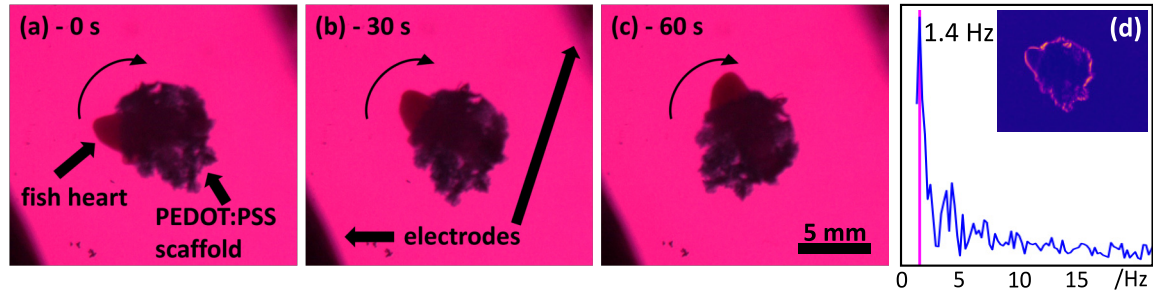
Figure 3.17. *PEDOT:PSS scaffold glued to a fish heart. The heart's contractions caused a scaffold rotation of approximately 90° within one minute with a 1.4 Hz beating frequency.*

Nevertheless, instead of using a whole heart, implementing individual cardiomyocytes would be a more feasible approach as discussed in Section 3.5.2 where cardiomyocytes could either be isolated from heart tissue or generated by induced pluripotent stem cells from, e.g., fibroblast cells. An additional advantage to using fish or lower vertebrates is their cardiomyocyte's lifelong ability to proliferate in comparison to the mammals' drastic drop within a month after birth. [183] Isolated primary cardiomyocytes from adult zebrafish hearts could be cultured up to 4 weeks while maintaining their mature sarcomeric integrity and contractile properties. [184] Although the iPSC technology was mainly focusing on mammalian species in the past decade, efforts were also made to generate induced pluripotent stem cells from fish as new chemical reprogramming methods were successfully employed. [185] Taken together, the use of fish cardiomyocytes offers great potential in biohybrid robotic applications due to their proliferation capabilities, fast development in contrast to mammals and their functionality at room temperature.

3.6. Conclusion and perspective

In this chapter, I presented a novel preparation method of reproducible fibrous, conductive scaffolds made from aero-PEDOT:PSS that is suitable for culturing contractile cells and applicable in biohybrid soft robotics. Based on a microengineering approach, this method enables a fast and easy fabrication of MTT assay-confirmed biocompatible macroscopic specimens with a fibrous structure analogous to a cell's extracellular matrix. The scaffolds exhibit a high specific conductivity of $22.6\,\mathrm{S\,m^{-1}}$ even after two weeks of storage in water, which is four orders of magnitude larger than previously reported 3D PEDOT:PSS structures with a $0.014\,\mathrm{S\,m^{-1}}$ maximum conductivity. They also demonstrate a sufficient mechanical stability with a $15\,\mathrm{kPa}$ Young's modulus in

an aqueous environment, which renders them suited to serve as artificial extracellular matrix environments for contractile cells like skeletal muscle cells or cardiomyocytes. I displayed a straight-forward incubation procedure to achieve a homogeneous coverage of the aero-PEDOT:PSS scaffold arms with cell adhesion promoting motifs. Cell adhesion studies using fibroblasts and skeletal muscle cells were carried out to verify the aero-PEDOT:PSS scaffolds suitability as artificial cell platforms through fluorescence staining and scanning electron microscopy that elucidated the cells' excellent adhesion and proliferation as well as myotube formation in the case of skeletal muscle cells. This was additionally validated by the lack of any significant differences in cell behavior between those cultured on fibronectin-biofunctionalized scaffolds or when merely incubated in pure medium, thus infers a sufficient protein adsorption capability of PEDOT:PSS. Moreover, cardiomyocytes derived from induced pluripotent stem cells (iPSC-CMs) cultured on aero-PEDOT:PSS scaffolds illustrated great spreading, developed visible actin fibers and Z-bands as well as enacting a good beating behavior. The cardiomyocytes' ability to deform the individual PEDOT:PSS arms they were attached to was also analyzed and the overall scaffold deformation was calculated to be around 4.3 µm. I also carried out a pioneering study using a whole heart tissue from a medaka rice fish that was integrated successfully with a PEDOT:PSS scaffold. The use of individual fish cardiomyocytes, whether isolated from animals or derived from induced pluripotent stem cells, offers a great potential in biohybrid robotic applications due to their proliferation capabilities, rapid development and their ability to function at room temperature in contrast to those extracted from mammals. This work represents an important advancement and a crucial step towards future work in this field.

Taken together, I demonstrated that aero-PEDOT:PSS scaffolds are valuable scaffolds for culturing contractile cells by virtue of their fibrous structure, great protein adsorption aptitude, high electrical conductivity, applicable mechanical properties and a promising capacity to assimilate the extracellular matrix structurally and biochemically.

Conclusion

I developed and employed a microengineering approach to fabricate two different 3D conductive scaffold systems for culturing contractile cells like skeletal muscle cells and cardiomyocytes that can serve as motors for biohybrid soft robotics. Both systems were able to provide the required electrical and mechanical cues for a successful implementation as artificial scaffolds that mimic the physical and structural characteristics of a cell's natural extracellular matrix. The approach is based on exploiting a functionally-coated sacrificial template of interconnected tetrapod-shaped zinc oxide micro particles (t-ZnO) that resulted in a highly porous network of conductive pathways from either a hydrogel permeated with a filler material that renders it conductive or a conductive polymer matrix.

In the hydrogel system, the conductivity was obtained through incorporating an exfoliated graphene (EG) framework into a polyacrylamide (PAM) hydrogel to create a conductive network that pervades the matrix. Filler graphene concentrations as low as $0.16\,\text{vol}\%$ EG resulted in an electrical conductivity as high as $0.34\,\text{S}\,\text{m}^{-1}$ while inflicting a negligible impact on the hydrogel mechanical stability that displayed a mere $10\,\%$ increase in Young's modulus, which represents an unprecedented success in comparison to state of the art techniques. The approach also demonstrated a great versatility and allowed a useful control over matrix size, shape, porosity, conductivity and mechanical behavior in addition to offering the freedom to adjust matrix features through various means such as t-ZnO sacrificial template density, infiltrations number and conductive filler dispersion concentration as well as by using different nanomaterials. For instance, conductivities that spanned a range between $0.012\,\text{S}\,\text{m}^{-1}$ to $1.8\,\text{S}\,\text{m}^{-1}$ were achieved by using different filler concentrations whereas mechanical strengths between 60 to $90\,\text{kPa}$ were attainable in PAM with an ability to customise it to a level between 25 and $55\,\text{kPa}$ using assorted PAM and gelatin methacryloyl (GelMA) composites. GelMA and combinations of PAM and GelMA also demonstrated their suitability as biofunctional conductive hydrogels that were capable of promoting good skeletal muscle cells spreading and proliferation. Cardiomyocytes induced from pluripotent stem cells (iPSCs) showed concentric contraction that led to a GelMA substrate deformation by a few micrometers that translates to $5\,\%$ change in cell length, which presents a valuable potential in biohybrid applications. I additionally studied the microengineering method's capacity for enhancing the thermoresponsive poly-N-isopropylacrylamide hydrogel volume change that increased from around $5.3\,\%$ in bulk hydrogels in terms of deformation to a remarkable $54\,\%$ in microengineered specimens even without a conductive filler material. The integration of these findings with added suitable conductive fillers in a perspective work would enable heating up only the hydrogel via applied electrical or light pulses instead of the entire hydrogel surrounding.

In a pioneering study, fibroblasts as a non-contractile mammalian cell type were em-

ployed as motor cells for biohybrid actuation. Here, photoswitchable drug optojasps were exploited as means to release the tensile forces exerted by fibroblasts that generated a collagen scaffold contraction and result in a 6% change in specimen diameter.

In the second part of my thesis, I exploited the microengineering approach in combination with the conductive poly(3,4-ethylenedioxythiophene):polystyrene sulfonate (PEDOT:PSS) polymer to generate biocompatible 3D scaffolds suitable for contractile cells culturing with a fibrous structure that mimics a cell's extracellular matrix. Even after two weeks of storage in water, the scaffolds exhibited a high specific conductivity of $22.6\,\mathrm{S\,m^{-1}}$ that is four orders of magnitude greater than previously reported 3D PEDOT:PSS structures with a $0.014\,\mathrm{S\,m^{-1}}$ maximum conductivity in addition to demonstrating a substantial mechanical integrity with a $15\,\mathrm{kPa}$ Young's modulus in an aqueous environment, which makes it structurally capable as an artificial cellular environment. The scaffolds showed a good biocompatibility of around 80% in MTT assays and also a high protein adsorption capacity of about 66% of the available proteins in solution within $24\,\mathrm{h}$, thus allowing for a simple biofunctionalization procedure via incubation. Cultured fibroblasts and skeletal muscle cells elucidated excellent adhesion and proliferation besides myotube formation in the case of skeletal muscle cells whereas iPSC-cardiomyocytes were able to spread well, developed visible actin fibers and Z-bands in addition to enacting a steady beating behavior while inducing a $4.3\,\mathrm{\mu m}$ overall scaffold deformation.

The various 3D scaffolds I developed, investigated and presented in my work are valuable for culturing contractile cells by virtue of their microstructure, great protein adsorption aptitude, high electrical conductivity, applicable mechanical properties and a promising ability to assimilate the extracellular matrix. They also demonstrate potential in a wide variety of desirable applications from liquid transport and drug delivery where the interconnected channel system pervading the hydrogel can enhance diffusion to bioelectronics, biosensing and biohybrid soft robotics.

Bibliography

[1] T. Distler and A. R. Boccaccini, "3D printing of electrically conductive hydrogels for tissue engineering and biosensors – A review," *Acta Biomaterialia*, vol. 101, pp. 1–13, 2020.

[2] I. Y. Jung, J. S. Kim, B. R. Choi, K. Lee, and H. Lee, "Hydrogel Based Biosensors for In Vitro Diagnostics of Biochemicals, Proteins, and Genes," *Advanced Healthcare Materials*, vol. 6, no. 12, p. 1601475, 2017.

[3] S. R. Shin, R. Farzad, A. Tamayol, V. Manoharan, P. Mostafalu, Y. S. Zhang, M. Akbari, S. M. Jung, D. Kim, M. Comotto, N. Annabi, F. E. Al-Hazmi, M. R. Dokmeci, and A. Khademhosseini, "A Bioactive Carbon Nanotube-Based Ink for Printing 2D and 3D Flexible Electronics," *Advanced Materials*, vol. 28, no. 17, pp. 3280–3289, 2016.

[4] H. S. Song, O. S. Kwon, J. H. Kim, J. Conde, and N. Artzi, "3D hydrogel scaffold doped with 2D graphene materials for biosensors and bioelectronics," *Biosensors and Bioelectronics*, vol. 89, pp. 187–200, 2017.

[5] F. Fu, J. Wang, H. Zeng, and J. Yu, "Functional Conductive Hydrogels for Bioelectronics," *ACS Materials Letters*, vol. 2, no. 10, pp. 1287–1301, 2020.

[6] Q. Ding, X. Xu, Y. Yue, C. Mei, C. Huang, S. Jiang, Q. Wu, and J. Han, "Nanocellulose-Mediated Electroconductive Self-Healing Hydrogels with High Strength, Plasticity, Viscoelasticity, Stretchability, and Biocompatibility toward Multifunctional Applications," *ACS Applied Materials and Interfaces*, vol. 10, no. 33, pp. 27987–28002, 2018.

[7] C. Zheng, K. Lu, Y. Lu, S. Zhu, Y. Yue, X. Xu, C. Mei, H. Xiao, Q. Wu, and J. Han, "A stretchable, self-healing conductive hydrogels based on nanocellulose supported graphene towards wearable monitoring of human motion," *Carbohydrate Polymers*, vol. 250, p. 116905, 2020.

[8] M. Sasaki, B. C. Karikkineth, K. Nagamine, H. Kaji, K. Torimitsu, and M. Nishizawa, "Highly Conductive Stretchable and Biocompatible Electrode-Hydrogel Hybrids for Advanced Tissue Engineering," *Advanced Healthcare Materials*, vol. 3, no. 11, pp. 1919–1927, 2014.

[9] S. Wang, S. Guan, J. Xu, W. Li, D. Ge, C. Sun, T. Liu, and X. Ma, "Neural stem cell proliferation and differentiation in the conductive PEDOT-HA/Cs/Gel scaffold for neural tissue engineering," *Biomaterials Science*, vol. 5, no. 10, pp. 2024–2034, 2017.

[10] A. Navaei, N. Moore, R. T. Sullivan, D. Truong, R. Q. Migrino, and M. Nikkhah, "Electrically conductive hydrogel-based micro-topographies for the development

of organized cardiac tissues," *RSC Advances*, vol. 7, no. 6, pp. 3302–3312, 2017.

[11] S. R. Shin, C. Zihlmann, M. Akbari, P. Assawes, L. Cheung, K. Zhang, V. Manoharan, Y. S. Zhang, M. Yüksekkaya, K. Wan, M. Nikkhah, M. R. Dokmeci, X. S. Tang, and A. Khademhosseini, "Reduced Graphene Oxide-GelMA Hybrid Hydrogels as Scaffolds for Cardiac Tissue Engineering," *Small*, vol. 12, no. 27, pp. 3677–3689, 2016.

[12] B. Guo and P. X. Ma, "Conducting Polymers for Tissue Engineering," *Biomacromolecules*, vol. 19, no. 6, pp. 1764–1782, 2018.

[13] C. Appiah, C. Arndt, K. Siemsen, A. Heitmann, A. Staubitz, and C. Selhuber-Unkel, "Living Materials Herald a New Era in Soft Robotics," *Advanced Materials*, vol. 31, no. 36, p. 1807747, 2019.

[14] K. Roshanbinfar, L. Vogt, B. Greber, S. Diecke, A. R. Boccaccini, T. Scheibel, and F. B. Engel, "Electroconductive Biohybrid Hydrogel for Enhanced Maturation and Beating Properties of Engineered Cardiac Tissues," *Advanced Functional Materials*, vol. 28, no. 42, p. 1803951, 2018.

[15] K. Roshanbinfar, Z. Mohammadi, A. S.-M. Mesgar, M. M. Dehghan, O. P. Oommen, J. Hilborn, and F. B. Engel, "Carbon nanotube doped pericardial matrix derived electroconductive biohybrid hydrogel for cardiac tissue engineering," *Biomaterials Science*, vol. 7, no. 9, pp. 3906–3917, 2019.

[16] F. Martino, A. R. Perestrelo, V. Vinarský, S. Pagliari, and G. Forte, "Cellular mechanotransduction: From tension to function," *Frontiers in Physiology*, vol. 9, p. 824, 2018.

[17] N. Noor, A. Shapira, R. Edri, I. Gal, L. Wertheim, and T. Dvir, "3D Printing of Personalized Thick and Perfusable Cardiac Patches and Hearts," *Advanced Science*, vol. 6, no. 11, p. 1900344, 2019.

[18] E. C. Novosel, C. Kleinhans, and P. J. Kluger, "Vascularization is the key challenge in tissue engineering," *Advanced Drug Delivery Reviews*, vol. 63, no. 4-5, pp. 300–311, 2011.

[19] J. Min, M. Patel, and W.-G. Koh, "Incorporation of Conductive Materials into Hydrogels for Tissue Engineering Applications," *Polymers*, vol. 10, no. 10, p. 1078, 2018.

[20] C. Chen, Y. Wang, T. Meng, Q. Wu, L. Fang, D. Zhao, Y. Zhang, and D. Li, "Electrically conductive polyacrylamide/carbon nanotube hydrogel: reinforcing effect from cellulose nanofibers," *Cellulose*, vol. 26, no. 16, pp. 8843–8851, 2019.

[21] S. R. Shin, B. Migliori, B. Miccoli, Y. Li, P. Mostafalu, J. Seo, S. Mandla, A. Enrico, S. Antona, R. Sabarish, T. Zheng, L. Pirrami, K. Zhang, Y. S. Zhang, K. Wan, D. Demarchi, M. R. Dokmeci, and A. Khademhosseini, "Electrically Driven Microengineered Bioinspired Soft Robots," *Advanced Materials*, vol. 30,

no. 10, p. 1704189, 2018.

[22] K. Y. Lee, S.-J. Park, D. G. Matthews, S. L. Kim, C. A. Marquez, J. F. Zimmerman, H. A. M. Ardoña, A. G. Kleber, G. V. Lauder, and K. K. Parker, "An autonomously swimming biohybrid fish designed with human cardiac biophysics," *Science*, vol. 375, no. 6581, pp. 639–647, 2022.

[23] R. Raman, C. Cvetkovic, S. G. M. Uzel, R. J. Platt, P. Sengupta, R. D. Kamm, and R. Bashir, "Optogenetic skeletal muscle-powered adaptive biological machines," *Proceedings of the National Academy of Sciences*, vol. 113, no. 13, pp. 3497–3502, 2016.

[24] Y. Akiyama, K. Iwabuchi, Y. Furukawa, and K. Morishima, "Long-term and room temperature operable bioactuator powered by insect dorsal vessel tissue," *Lab ChipChip*, vol. 9, no. 1, pp. 140–144, 2009.

[25] L. Ricotti, B. Trimmer, A. W. Feinberg, R. Raman, K. K. Parker, R. Bashir, M. Sitti, S. Martel, P. Dario, and A. Menciassi, "Biohybrid actuators for robotics: A review of devices actuated by living cells," *Science Robotics*, vol. 2, no. 12, p. eaaq0495, 2017.

[26] Y. Haraguchi, T. Shimizu, M. Yamato, A. Kikuchi, and T. Okano, "Electrical coupling of cardiomyocyte sheets occurs rapidly via functional gap junction formation," *Biomaterials*, vol. 27, no. 27, pp. 4765–4774, 2006.

[27] J. Zhou, J. Chen, H. Sun, X. Qiu, Y. Mou, Z. Liu, Y. Zhao, X. Li, Y. Han, C. Duan, R. Tang, C. Wang, W. Zhong, J. Liu, Y. Luo, M. (Mengqiu) Xing, and C. Wang, "Engineering the heart: Evaluation of conductive nanomaterials for improving implant integration and cardiac function," *Scientific Reports*, vol. 4, no. 1, p. 3733, 2014.

[28] A. D. Bach, J. Stern-Straeter, J. P. Beier, H. Bannasch, and G. B. Stark, "Engineering of muscle tissue," *Clinics in Plastic Surgery*, vol. 30, no. 4, pp. 589–599, 2003.

[29] I. Y. Shadrin, A. Khodabukus, and N. Bursac, "Striated muscle function, regeneration, and repair," *Cellular and Molecular Life Sciences*, vol. 73, no. 22, pp. 4175–4202, 2016.

[30] A. Kajzar, C. M. Cesa, N. Kirchgeßner, B. Hoffmann, and R. Merkel, "Toward Physiological Conditions for Cell Analyses: Forces of Heart Muscle Cells Suspended Between Elastic Micropillars," *Biophysical Journal*, vol. 94, no. 5, pp. 1854–1866, 2008.

[31] B. Hinz, "The myofibroblast: Paradigm for a mechanically active cell," *Journal of Biomechanics*, vol. 43, no. 1, pp. 146–155, 2010.

[32] A. M. Samarel, "Costameres, focal adhesions, and cardiomyocyte mechanotransduction," *American Journal of Physiology-Heart and Circulatory Physiology*,

vol. 289, no. 6, pp. H2291–H2301, 2005.

[33] P. M. Hopkins, "Skeletal muscle physiology," *Continuing Education in Anaesthesia Critical Care & Pain*, vol. 6, no. 1, pp. 1–6, 2006.

[34] V. A. Webster, K. J. Chapin, E. L. Hawley, J. M. Patel, O. Akkus, H. J. Chiel, and R. D. Quinn, "Aplysia Californica as a Novel Source of Material for Biohybrid Robots and Organic Machines," in *Biomimetic and Biohybrid Systems* (N. F. Lepora, A. Mura, M. Mangan, P. F. Verschure, M. Desmulliez, and T. J. Prescott, eds.), (Edinburgh), pp. 365–374, Springer Verlag, 2016.

[35] R. Bischoff, "Regeneration of single skeletal muscle fibers in vitro," *The Anatomical Record*, vol. 182, no. 2, pp. 215–235, 1975.

[36] K. Kikuchi and K. D. Poss, "Cardiac regenerative capacity and mechanisms.," *Annual review of cell and developmental biology*, vol. 28, pp. 719–41, 2012.

[37] J. G. Betts, K. A. Young, J. A. Wise, E. Johnson, B. Poe, D. H. Kruse, O. Korol, J. E. Johnson, M. Womble, and P. DeSaix, *Anatomy & Physiology*. Houston, Texas: OpenStax, 1 ed., 2013.

[38] R. M. Duffy and A. W. Feinberg, "Engineered skeletal muscle tissue for soft robotics: Fabrication strategies, current applications, and future challenges," *Wiley Interdisciplinary Reviews: Nanomedicine and Nanobiotechnology*, vol. 6, no. 2, pp. 178–195, 2014.

[39] I. Hunter and S. Lafontaine, "A comparison of muscle with artificial actuators," in *Technical Digest IEEE Solid-State Sensor and Actuator Workshop*, pp. 178–185, IEEE, 1992.

[40] A. J. Engler, M. A. Griffin, S. Sen, C. G. Bönnemann, H. L. Sweeney, and D. E. Discher, "Myotubes differentiate optimally on substrates with tissue-like stiffness: Pathological implications for soft or stiff microenvironments," *Journal of Cell Biology*, vol. 166, no. 6, pp. 877–887, 2004.

[41] J. Shintake, V. Cacucciolo, D. Floreano, and H. Shea, "Soft Robotic Grippers," *Advanced Materials*, vol. 30, no. 29, p. 1707035, 2018.

[42] R. N. Palchesko, L. Zhang, Y. Sun, and A. W. Feinberg, "Development of Polydimethylsiloxane Substrates with Tunable Elastic Modulus to Study Cell Mechanobiology in Muscle and Nerve," *PLoS ONE*, vol. 7, no. 12, p. e51499, 2012.

[43] H. Kaji, T. Ishibashi, K. Nagamine, M. Kanzaki, and M. Nishizawa, "Electrically induced contraction of C2C12 myotubes cultured on a porous membrane-based substrate with muscle tissue-like stiffness," *Biomaterials*, vol. 31, no. 27, pp. 6981–6986, 2010.

[44] S. Ahadian, S. Ostrovidov, V. Hosseini, H. Kaji, M. Ramalingam, H. Bae, and

A. Khademhosseini, "Electrical stimulation as a biomimicry tool for regulating muscle cell behavior.," *Organogenesis*, vol. 9, no. 2, pp. 87–92, 2013.

[45] C. A. Powell, B. L. Smiley, J. Mills, and H. H. Vandenburgh, "Mechanical stimulation improves tissue-engineered human skeletal muscle," *American Journal of Physiology-Cell Physiology*, vol. 283, no. 5, pp. C1557–C1565, 2002.

[46] T. Asano, T. Ishizuka, K. Morishima, and H. Yawo, "Optogenetic induction of contractile ability in immature C2C12 myotubes," *Scientific Reports*, vol. 5, p. 8317, 2015.

[47] S. I. Rich, R. J. Wood, and C. Majidi, "Untethered soft robotics," *Nature Electronics*, vol. 1, no. 2, pp. 102–112, 2018.

[48] S. R. Shin, S. M. Jung, M. Zalabany, K. Kim, P. Zorlutuna, S. B. Kim, M. Nikkhah, M. Khabiry, M. Azize, J. Kong, K. T. Wan, T. Palacios, M. R. Dokmeci, H. Bae, X. W. Tang, and A. Khademhosseini, "Carbon-Nanotube-Embedded Hydrogel Sheets for Engineering Cardiac Constructs and Bioactuators," *ACS Nano*, vol. 7, no. 3, pp. 2369–2380, 2013.

[49] C.-W. W. Hsiao, M.-Y. Y. Bai, Y. Chang, M.-F. F. Chung, T.-Y. Y. Lee, C.-T. T. Wu, B. Maiti, Z.-X. X. Liao, R.-K. K. Li, and H.-W. W. Sung, "Electrical coupling of isolated cardiomyocyte clusters grown on aligned conductive nanofibrous meshes for their synchronized beating," *Biomaterials*, vol. 34, no. 4, pp. 1063–1072, 2013.

[50] L. Wang, Y. Wu, T. Hu, B. Guo, and P. X. Ma, "Electrospun conductive nanofibrous scaffolds for engineering cardiac tissue and 3D bioactuators," *Acta Biomaterialia*, vol. 59, pp. 68–81, 2017.

[51] S. A. Bernstein and G. E. Morley, "Gap junctions and propagation of the cardiac action potential.," *Advances in cardiology*, vol. 42, pp. 71–85, 2006.

[52] B. Maher, "Tissue engineering: How to build a heart," *Nature*, vol. 499, no. 7456, pp. 20–22, 2013.

[53] A. K. Peter, M. A. Bjerke, and L. A. Leinwand, "Biology of the cardiac myocyte in heart disease," *Molecular Biology of the Cell*, vol. 27, no. 14, pp. 2149–2160, 2016.

[54] S.-J. Park, M. Gazzola, K. S. Park, S. Park, V. Di Santo, E. L. Blevins, J. U. Lind, P. H. Campbell, S. Dauth, A. K. Capulli, F. S. Pasqualini, S. Ahn, A. Cho, H. Yuan, B. M. Maoz, R. Vijaykumar, J.-W. Choi, K. Deisseroth, G. V. Lauder, L. Mahadevan, and K. K. Parker, "Phototactic guidance of a tissue-engineered soft-robotic ray," *Science*, vol. 353, no. 6295, pp. 158–162, 2016.

[55] B. Liau, D. Zhang, and N. Bursac, "Functional cardiac tissue engineering.," *Regenerative medicine*, vol. 7, no. 2, pp. 187–206, 2012.

[56] M. Tiburcy, J. E. Hudson, P. Balfanz, S. Schlick, T. Meyer, M.-L. Chang Liao, E. Levent, F. Raad, S. Zeidler, E. Wingender, J. Riegler, M. Wang, J. D. Gold, I. Kehat, E. Wettwer, U. Ravens, P. Dierickx, L. W. van Laake, M. J. Goumans, S. Khadjeh, K. Toischer, G. Hasenfuss, L. A. Couture, A. Unger, W. A. Linke, T. Araki, B. Neel, G. Keller, L. Gepstein, J. C. Wu, and W.-H. Zimmermann, "Defined Engineered Human Myocardium With Advanced Maturation for Applications in Heart Failure Modeling and Repair.," *Circulation*, vol. 135, no. 19, pp. 1832–1847, 2017.

[57] K. Takahashi and S. Yamanaka, "Induction of Pluripotent Stem Cells from Mouse Embryonic and Adult Fibroblast Cultures by Defined Factors," *Cell*, vol. 126, no. 4, pp. 663–676, 2006.

[58] K. Takahashi, K. Tanabe, M. Ohnuki, M. Narita, T. Ichisaka, K. Tomoda, and S. Yamanaka, "Induction of Pluripotent Stem Cells from Adult Human Fibroblasts by Defined Factors," *Cell*, vol. 131, no. 5, pp. 861–872, 2007.

[59] D. Boujard, B. Anselme, C. Cullin, and C. Raguénès-Nicol, *Zell- und Molekularbiologie im Überblick*. Heidelberg: Springer Spektrum, 1 ed., 2014.

[60] K. Munk, *Biochemie - Zellbiologie*. Stuttgart: Georg Thieme Verlag, 1 ed., 2008.

[61] B. M. Gumbiner, "Cell adhesion: The molecular basis of tissue architecture and morphogenesis," *Cell*, vol. 84, pp. 345–357, 1996.

[62] D. Carson, M. Hnilova, X. Yang, C. L. Nemeth, J. H. Tsui, A. S. Smith, A. Jiao, M. Regnier, C. E. Murry, C. Tamerler, and D.-H. Kim, "Nanotopography-Induced Structural Anisotropy and Sarcomere Development in Human Cardiomyocytes Derived from Induced Pluripotent Stem Cells," *ACS Applied Materials & Interfaces*, vol. 8, no. 34, pp. 21923–21932, 2016.

[63] A. Solouk, B. G. Cousins, F. Mirahmadi, H. Mirzadeh, M. R. J. Nadoushan, M. A. Shokrgozar, and A. M. Seifalian, "Biomimetic modified clinical-grade POSS-PCU nanocomposite polymer for bypass graft applications: A preliminary assessment of endothelial cell adhesion and haemocompatibility," *Materials Science and Engineering: C*, vol. 46, pp. 400–408, 2015.

[64] Y. S. Chen, P. C. Tsou, J. M. Lo, H. C. Tsai, Y. Z. Wang, and G. H. Hsiue, "Poly(N-isopropylacrylamide) hydrogels with interpenetrating multiwalled carbon nanotubes for cell sheet engineering," *Biomaterials*, vol. 34, no. 30, pp. 7328–7334, 2013.

[65] Y. Chandorkar, A. Castro Nava, S. Schweizerhof, M. Van Dongen, T. Haraszti, J. Köhler, H. Zhang, R. Windoffer, A. Mourran, M. Möller, and L. De Laporte, "Cellular responses to beating hydrogels to investigate mechanotransduction," *Nature Communications*, vol. 10, no. 1, p. 4027, 2019.

[66] A. J. Engler, S. Sen, H. L. Sweeney, and D. E. Discher, "Matrix Elasticity Directs

Stem Cell Lineage Specification," *Cell*, vol. 126, no. 4, pp. 677–689, 2006.

[67] H.-B. Wang, M. Dembo, and Y.-L. Wang, "Substrate flexibility regulates growth and apoptosis of normal but not transformed cells," *American Journal of Physiology - Cell Physiology*, vol. 279, no. 5, pp. C1345–C1350, 2000.

[68] A. J. Engler, C. Carag-Krieger, C. P. Johnson, D. E. Discher, J. W. Sanger, D. W. Speicher, J. M. Sanger, M. Raab, and H.-Y. Tang, "Embryonic cardiomyocytes beat best on a matrix with heart-like elasticity: scar-like rigidity inhibits beating," *Journal of Cell Science*, vol. 121, no. 22, pp. 3794–3802, 2008.

[69] C. S. Chen, M. Mrksich, S. Huang, G. M. Whitesides, and D. E. Ingber, "Geometric Control of Cell Life and Death," *Science*, vol. 276, no. 5317, pp. 1425–1428, 1997.

[70] U. S. Schwarz, N. Q. Balaban, D. Riveline, A. Bershadsky, B. Geiger, and S. A. Safran, "Calculation of Forces at Focal Adhesions from Elastic Substrate Data: The Effect of Localized Force and the Need for Regularization," *Biophysical Journal*, vol. 83, no. 3, pp. 1380–1394, 2002.

[71] F. Klein, T. Striebel, J. Fischer, Z. Jiang, C. M. Franz, G. von Freymann, M. Wegener, and M. Bastmeyer, "Elastic Fully Three-dimensional Microstructure Scaffolds for Cell Force Measurements," *Advanced Materials*, vol. 22, no. 8, pp. 868–871, 2010.

[72] K. Shimizu, H. Sasaki, H. Hida, H. Fujita, K. Obinata, M. Shikida, and E. Nagamori, "Assembly of skeletal muscle cells on a Si-MEMS device and their generative force measurement," *Biomedical Microdevices*, vol. 12, no. 2, pp. 247–252, 2010.

[73] R. Kocen, M. Gasik, A. Gantar, and S. Novak, "Viscoelastic behaviour of hydrogel-based composites for tissue engineering under mechanical load," *Biomedical Materials*, vol. 12, no. 2, p. 025004, 2017.

[74] M. Rizwan, R. Yahya, A. Hassan, M. Yar, A. D. Azzahari, V. Selvanathan, F. Sonsudin, and C. N. Abouloula, "pH sensitive hydrogels in drug delivery: Brief history, properties, swelling, and release mechanism, material selection and applications," *Polymers*, vol. 9, no. 4, 2017.

[75] L. H. Sperling, *Physical Polymer Science*. Hoboken, New Jersey, USA: John Wiley & Sons, 3 ed., 2001.

[76] S. R. Caliari and J. A. Burdick, "A practical guide to hydrogels for cell culture," *Nature Methods*, vol. 13, no. 5, pp. 405–414, 2016.

[77] C. F. Guimarães, L. Gasperini, A. P. Marques, and R. L. Reis, "The stiffness of living tissues and its implications for tissue engineering," *Nature Reviews Materials*, vol. 5, no. 5, pp. 351–370, 2020.

[78] C. C. Lin and A. T. Metters, "Hydrogels in controlled release formulations: Network design and mathematical modeling," *Advanced Drug Delivery Reviews*, vol. 58, no. 12-13, pp. 1379–1408, 2006.

[79] L. Fan, X. Ge, Y. Qian, M. Wei, Z. Zhang, W.-E. Yuan, and Y. Ouyang, "Advances in Synthesis and Applications of Self-Healing Hydrogels," *Frontiers in Bioengineering and Biotechnology*, vol. 8, pp. 1–14, 2020.

[80] E. Ruel-Gariépy and J. C. Leroux, "In situ-forming hydrogels—review of temperature-sensitive systems," *European Journal of Pharmaceutics and Biopharmaceutics*, vol. 58, no. 2, pp. 409–426, 2004.

[81] V. Brunella, S. A. Jadhav, I. Miletto, G. Berlier, E. Ugazio, S. Sapino, and D. Scalarone, "Hybrid drug carriers with temperature-controlled on–off release: A simple and reliable synthesis of PNIPAM-functionalized mesoporous silica nanoparticles," *Reactive and Functional Polymers*, vol. 98, pp. 31–37, 2016.

[82] M. A. Haq, Y. Su, and D. Wang, "Mechanical properties of PNIPAM based hydrogels: A review," *Materials Science and Engineering: C*, vol. 70, pp. 842–855, 2017.

[83] Y. Qiu and K. Park, "Environment-sensitive hydrogels for drug delivery," *Advanced Drug Delivery Reviews*, vol. 64, pp. 49–60, 2012.

[84] Y. Gao, D. Zhou, J. Lyu, A. Sigen, Q. Xu, B. Newland, K. Matyjaszewski, H. Tai, and W. Wang, "Complex polymer architectures through free-radical polymerization of multivinyl monomers," *Nature Reviews Chemistry*, vol. 4, no. 4, pp. 194–212, 2020.

[85] G. Odian, *Principles of Polymerization.* New York, New York, USA: John Wiley & Sons Inc., 4 ed., 2004.

[86] Y. Piao, H. You, T. Xu, H.-P. Bei, I. Z. Piwko, Y. Y. Kwan, and X. Zhao, "Biomedical applications of gelatin methacryloyl hydrogels," *Engineered Regeneration*, vol. 2, pp. 47–56, 2021.

[87] B. Trappmann, J. E. Gautrot, J. T. Connelly, D. G. Strange, Y. Li, M. L. Oyen, M. A. Cohen Stuart, H. Boehm, B. Li, V. Vogel, J. P. Spatz, F. M. Watt, and W. T. Huck, "Extracellular-matrix tethering regulates stem-cell fate," *Nature Materials*, vol. 11, no. 7, pp. 642–649, 2012.

[88] L. Klouda and A. G. Mikos, "Thermoresponsive hydrogels in biomedical applications," *European Journal of Pharmaceutics and Biopharmaceutics*, vol. 68, no. 1, pp. 34–45, 2008.

[89] L. Tang, L. Wang, X. Yang, Y. Feng, Y. Li, and W. Feng, "Poly(N-isopropylacrylamide)-based smart hydrogels: Design, properties and applications," *Progress in Materials Science*, vol. 115, p. 100702, 2021.

[90] M. Noh, Y. Mok, S. Lee, H. Kim, S. H. Lee, G.-w. Jin, J.-H. Seo, H. Koo, T. H. Park, and Y. Lee, "Novel lower critical solution temperature phase transition materials effectively control osmosis by mild temperature changes," *Chemical Communications*, vol. 48, no. 32, pp. 3845–3847, 2012.

[91] K. Ishida, T. Uno, T. Itoh, and M. Kubo, "Synthesis and Property of Temperature-Responsive Hydrogel with Movable Cross-Linking Points," *Macromolecules*, vol. 45, no. 15, pp. 6136–6142, 2012.

[92] B. Strachota, A. Strachota, M. Šlouf, J. Brus, and V. Cimrová, "Monolithic intercalated PNIPAm/starch hydrogels with very fast and extensive one-way volume and swelling responses to temperature and pH: prospective actuators and drug release systems," *Soft Matter*, vol. 15, no. 4, pp. 752–769, 2019.

[93] X. Z. Zhang and R. X. Zhuo, "Dynamic Properties of Temperature-Sensitive Poly(N-isopropylacrylamide) Gel Cross-Linked through Siloxane Linkage," *Langmuir*, vol. 17, no. 1, pp. 12–16, 2000.

[94] L.-W. Xia, R. Xie, X.-J. Ju, W. Wang, Q. Chen, and L.-Y. Chu, "Nano-structured smart hydrogels with rapid response and high elasticity," *Nature Communications*, vol. 4, no. 1, p. 2226, 2013.

[95] R. Yoshida, K. Uchida, Y. Kaneko, K. Sakai, A. Kikuchi, Y. Sakurai, and T. Okano, "Comb-type grafted hydrogels with rapid deswelling response to temperature changes," *Nature*, vol. 374, no. 6519, pp. 240–242, 1995.

[96] X. D. Xu, X. Z. Zhang, J. Yang, S. X. Cheng, R. X. Zhuo, and Y. Q. Huang, "Strategy to Introduce a Pendent Micellar Structure into Poly(N-isopropylacrylamide) Hydrogels," *Langmuir*, vol. 23, no. 8, pp. 4231–4236, 2007.

[97] T. Spratte, C. Arndt, I. Wacker, M. Hauck, R. Adelung, R. R. Schröder, F. Schütt, and C. Selhuber-Unkel, "Thermoresponsive Hydrogels with Improved Actuation Function by Interconnected Microchannels," *Advanced Intelligent Systems*, vol. 4, no. 3, p. 2100081, 2022.

[98] E. Lee, D. Kim, H. Kim, and J. Yoon, "Photothermally driven fast responding photo-actuators fabricated with comb-type hydrogels and magnetite nanoparticles," *Scientific Reports*, vol. 5, no. 1, p. 15124, 2015.

[99] X. Peng, C. Jiao, Y. Zhao, N. Chen, Y. Wu, T. Liu, and H. Wang, "Thermoresponsive Deformable Actuators Prepared by Local Electrochemical Reduction of Poly(N-isopropylacrylamide)/Graphene Oxide Hydrogels," *ACS Applied Nano Materials*, vol. 1, no. 4, pp. 1522–1530, 2018.

[100] T. E. de Oliveira, D. Mukherji, K. Kremer, and P. A. Netz, "Effects of stereochemistry and copolymerization on the LCST of PNIPAm," *The Journal of Chemical Physics*, vol. 146, no. 3, p. 034904, 2017.

[101] Y. Tanaka, K. Sato, T. Shimizu, M. Yamato, T. Okano, and T. Kitamori, "A

micro-spherical heart pump powered by cultured cardiomyocytes," *Lab Chip*, vol. 7, no. 2, pp. 207–212, 2007.

[102] H. Shirahama, B. H. Lee, L. P. Tan, and N.-J. Cho, "Precise Tuning of Facile One-Pot Gelatin Methacryloyl (GelMA) Synthesis," *Scientific Reports*, vol. 6, no. 1, p. 31036, 2016.

[103] J. Ratanavaraporn, S. Damrongsakkul, N. Sanchavanakit, T. Banaprasert, and S. Kanokpanont, "Comparison of Gelatin and Collagen Scaffolds for Fibroblast Cell Culture," *Journal of Metals, Materials and Minerals*, vol. 16, no. 1, pp. 31–36, 2006.

[104] A. O. Elzoghby, "Gelatin-based nanoparticles as drug and gene delivery systems: Reviewing three decades of research," *Journal of Controlled Release*, vol. 172, no. 3, pp. 1075–1091, 2013.

[105] Q. Xing, K. Yates, C. Vogt, Z. Qian, M. C. Frost, and F. Zhao, "Increasing mechanical strength of gelatin hydrogels by divalent metal ion removal," *Scientific Reports*, vol. 4, no. 1, p. 4706, 2014.

[106] M. Costantini, S. Testa, E. Fornetti, A. Barbetta, M. Trombetta, S. M. Cannata, C. Gargioli, and A. Rainer, "Engineering Muscle Networks in 3D Gelatin Methacryloyl Hydrogels: Influence of Mechanical Stiffness and Geometrical Confinement," *Frontiers in Bioengineering and Biotechnology*, vol. 5, no. 22, pp. 1–8, 2017.

[107] B. J. van Meer, H. de Vries, K. S. Firth, J. van Weerd, L. G. Tertoolen, H. B. Karperien, P. Jonkheijm, C. Denning, A. P. IJzerman, and C. L. Mummery, "Small molecule absorption by PDMS in the context of drug response bioassays," *Biochemical and Biophysical Research Communications*, vol. 482, no. 2, pp. 323–328, 2017.

[108] S. B. Campbell, Q. Wu, J. Yazbeck, C. Liu, S. Okhovatian, and M. Radisic, "Beyond Polydimethylsiloxane: Alternative Materials for Fabrication of Organ-on-a-Chip Devices and Microphysiological Systems," *ACS Biomaterials Science & Engineering*, vol. 7, no. 7, pp. 2880–2899, 2020.

[109] K. Obata, S. Slobin, A. Schonewille, A. Hohnholz, C. Unger, J. Koch, O. Suttmann, and L. Overmeyer, "UV laser direct writing of 2D/3D structures using photo-curable polydimethylsiloxane (PDMS)," *Applied Physics A: Materials Science and Processing*, vol. 123, no. 7, pp. 1–5, 2017.

[110] P. Dörschmann, S. Böser, D. Isik, C. Arndt, J. Roider, C. Selhuber-Unkel, and A. Klettner, "Influence of carrier materials and coatings on retinal pigment epithelium cultivation and functions," *Experimental Eye Research*, vol. 219, p. 109063, 2022.

[111] M. L. Oyen, "Mechanical characterisation of hydrogel materials," *International*

Materials Reviews, vol. 59, no. 1, pp. 44–59, 2014.

[112] S. Huth, S. Sindt, and C. Selhuber-Unkel, "Automated analysis of soft hydrogel microindentation: Impact of various indentation parameters on the measurement of Young's modulus," *PLoS ONE*, vol. 14, no. 8, p. e0220281, 2019.

[113] A. K. Denisin and B. L. Pruitt, "Tuning the Range of Polyacrylamide Gel Stiffness for Mechanobiology Applications," *ACS Applied Materials and Interfaces*, vol. 8, no. 34, pp. 21893–21902, 2016.

[114] M. Krieg, G. Fläschner, D. Alsteens, B. M. Gaub, W. H. Roos, G. J. L. Wuite, H. E. Gaub, C. Gerber, Y. F. Dufrêne, and D. J. Müller, "Atomic force microscopy-based mechanobiology," *Nature Reviews Physics*, vol. 1, no. 1, pp. 41–57, 2019.

[115] C. Arndt, M. Hauck, I. Wacker, B. Zeller-Plumhoff, F. Rasch, M. Taale, A. S. Nia, X. Feng, R. Adelung, R. R. Schröder, F. Schütt, and C. Selhuber-Unkel, "Microengineered Hollow Graphene Tube Systems Generate Conductive Hydrogels with Extremely Low Filler Concentration," *Nano Letters*, vol. 21, no. 8, pp. 3690–3697, 2021.

[116] A. J. Marsden, D. G. Papageorgiou, C. Vallés, A. Liscio, V. Palermo, M. A. Bissett, R. J. Young, and I. A. Kinloch, "Electrical percolation in graphene–polymer composites," *2D Materials*, vol. 5, no. 3, p. 032003, 2018.

[117] Y. Wu, Y. X. Chen, J. Yan, D. Quinn, P. Dong, S. W. Sawyer, and P. Soman, "Fabrication of conductive gelatin methacrylate–polyaniline hydrogels," *Acta Biomaterialia*, vol. 33, pp. 122–130, 2016.

[118] Y. Ganji, Q. Li, E. S. Quabius, M. Böttner, C. Selhuber-Unkel, and M. Kasra, "Cardiomyocyte behavior on biodegradable polyurethane/gold nanocomposite scaffolds under electrical stimulation," *Materials Science and Engineering: C*, vol. 59, pp. 10–18, 2016.

[119] M. Taale, F. Schütt, T. Carey, J. Marx, Y. K. Mishra, N. Stock, B. Fiedler, F. Torrisi, R. Adelung, and C. Selhuber-Unkel, "Biomimetic Carbon Fiber Systems Engineering: A Modular Design Strategy to Generate Biofunctional Composites from Graphene and Carbon Nanofibers," *ACS Applied Materials and Interfaces*, vol. 11, no. 5, pp. 5325–5335, 2019.

[120] J. Han, H. Wang, Y. Yue, C. Mei, J. Chen, C. Huang, Q. Wu, and X. Xu, "A self-healable and highly flexible supercapacitor integrated by dynamically cross-linked electro-conductive hydrogels based on nanocellulose-templated carbon nanotubes embedded in a viscoelastic polymer network," *Carbon*, vol. 149, pp. 1–18, 2019.

[121] C. Lee, X. Wei, J. W. Kysar, and J. Hone, "Measurement of the Elastic Properties and Intrinsic Strength of Monolayer Graphene," *Science*, vol. 321, no. 5887, pp. 385–388, 2008.

[122] J. Phiri, P. Gane, and T. C. Maloney, "General overview of graphene: Production, properties and application in polymer composites," *Materials Science and Engineering B: Solid-State Materials for Advanced Technology*, vol. 215, pp. 9–28, 2017.

[123] R. R. Nair, P. Blake, A. N. Grigorenko, K. S. Novoselov, T. J. Booth, T. Stauber, N. M. R. Peres, and A. K. Geim, "Fine Structure Constant Defines Visual Transparency of Graphene," *Science*, vol. 320, no. 5881, pp. 1308–1308, 2008.

[124] K. Didehban, M. Abdi, and F. Sharif, "Synthesis and Electrochemical Evaluation of Conductive Polyacrylamide Nanocomposite Hydrogels," *Advances in Polymer Technology*, vol. 35, no. 4, pp. 369–377, 2016.

[125] F. Rasch, F. Schütt, L. M. Saure, S. Kaps, J. Strobel, O. Polonskyi, A. S. Nia, M. R. Lohe, Y. K. Mishra, F. Faupel, L. Kienle, X. Feng, and R. Adelung, "Wet-Chemical Assembly of 2D Nanomaterials into Lightweight, Microtube-Shaped, and Macroscopic 3D Networks," *ACS Applied Materials and Interfaces*, vol. 11, no. 47, pp. 44652–44663, 2019.

[126] Y. K. Mishra, S. Kaps, A. Schuchardt, I. Paulowicz, X. Jin, D. Gedamu, S. Freitag, M. Claus, S. Wille, A. Kovalev, S. N. Gorb, and R. Adelung, "Fabrication of Macroscopically Flexible and Highly Porous 3D Semiconductor Networks from Interpenetrating Nanostructures by a Simple Flame Transport Approach," *Particle & Particle Systems Characterization*, vol. 30, no. 9, pp. 775–783, 2013.

[127] Y. K. Mishra, G. Modi, V. Cretu, V. Postica, O. Lupan, T. Reimer, I. Paulowicz, V. Hrkac, W. Benecke, L. Kienle, and R. Adelung, "Direct Growth of Freestanding ZnO Tetrapod Networks for Multifunctional Applications in Photocatalysis, UV Photodetection, and Gas Sensing," *ACS Applied Materials & Interfaces*, vol. 7, no. 26, pp. 14303–14316, 2015.

[128] F. Schütt, S. Signetti, H. Krüger, S. Röder, D. Smazna, S. Kaps, S. N. Gorb, Y. K. Mishra, N. M. Pugno, and R. Adelung, "Hierarchical self-entangled carbon nanotube tube networks," *Nature Communications*, vol. 8, no. 1, pp. 1–10, 2017.

[129] W. Li, J. Zhou, and Y. Xu, "Study of the in vitro cytotoxicity testing of medical devices," *Biomedical Reports*, vol. 3, no. 5, pp. 617–620, 2015.

[130] Z. Kaberova, E. Karpushkin, M. Nevoralová, M. Vetrík, M. Šlouf, and M. Dušková-Smrčková, "Microscopic Structure of Swollen Hydrogels by Scanning Electron and Light Microscopies: Artifacts and Reality," *Polymers*, vol. 12, no. 3, p. 578, 2020.

[131] R. Aston, K. Sewell, T. Klein, G. Lawrie, and L. Grøndahl, "Evaluation of the impact of freezing preparation techniques on the characterisation of alginate hydrogels by cryo-SEM," *European Polymer Journal*, vol. 82, pp. 1–15, 2016.

[132] K. Xu, P. Cao, and J. R. Heath, "Scanning Tunneling Microscopy Characteriza-

tion of the Electrical Properties of Wrinkles in Exfoliated Graphene Monolayers," *Nano Letters*, vol. 9, no. 12, pp. 4446–4451, 2009.

[133] H. C. Schniepp, J. L. Li, M. J. McAllister, H. Sai, M. Herrera-Alonson, D. H. Adamson, R. K. Prud'homme, R. Car, D. A. Seville, and I. A. Aksay, "Functionalized single graphene sheets derived from splitting graphite oxide," *Journal of Physical Chemistry B*, vol. 110, no. 17, pp. 8535–8539, 2006.

[134] H. Aoki and M. S. Dresselhaus, *Physics of Graphene.* NanoScience and Technology, Basel: Springer International Publishing, 1 ed., 2014.

[135] J. Suhr, P. Victor, L. Ci, S. Sreekala, X. Zhang, O. Nalamasu, and P. M. Ajayan, "Fatigue resistance of aligned carbon nanotube arrays under cyclic compression," *Nature Nanotechnology*, vol. 2, no. 7, pp. 417–421, 2007.

[136] H. Wang and Q. Li, "Prediction of elastic modulus and Poisson's ratio for unsaturated concrete," *International Journal of Solids and Structures*, vol. 44, no. 5, pp. 1370–1379, 2007.

[137] Y. Liu, X. Wu, Y. Tian, X. Zhou, B. Yu, Q. Zhang, R. Du, Q. Fu, and F. Chen, "Largely enhanced oxidation of graphite flakes via ammonium persulfate assisted gas expansion for the preparation of graphene oxide sheets," *Carbon*, vol. 146, pp. 618–626, 2019.

[138] Q. Peng, J. Chen, T. Wang, X. Peng, J. Liu, X. Wang, J. Wang, and H. Zeng, "Recent advances in designing conductive hydrogels for flexible electronics," *InfoMat*, vol. 2, no. 5, pp. 843–865, 2020.

[139] J. Kumai, S. Sasagawa, M. Horie, and Y. Yui, "A Novel Method for Polyacrylamide Gel Preparation Using N-hydroxysuccinimide-acrylamide Ester to Study Cell-Extracellular Matrix Mechanical Interactions," *Frontiers in Materials*, vol. 8, p. 20, 2021.

[140] A. Bettadapur, G. C. Suh, N. A. Geisse, E. R. Wang, C. Hua, H. A. Huber, A. A. Viscio, J. Y. Kim, J. B. Strickland, and M. L. McCain, "Prolonged Culture of Aligned Skeletal Myotubes on Micromolded Gelatin Hydrogels," *Scientific Reports*, vol. 6, no. 1, p. 28855, 2016.

[141] Y. K. Mishra and R. Adelung, "ZnO tetrapod materials for functional applications," *Materials Today*, vol. 21, no. 6, pp. 631–651, 2018.

[142] L. Han, J. Xu, X. Lu, D. Gan, Z. Wang, K. Wang, H. Zhang, H. Yuan, and J. Weng, "Biohybrid methacrylated gelatin/polyacrylamide hydrogels for cartilage repair," *Journal of Materials Chemistry B*, vol. 5, no. 4, pp. 731–741, 2017.

[143] I. Noshadi, S. Hong, K. E. Sullivan, E. Shirzaei Sani, R. Portillo-Lara, A. Tamayol, S. R. Shin, A. E. Gao, W. L. Stoppel, L. D. Black III, A. Khademhosseini, and N. Annabi, "In vitro and in vivo analysis of visible light crosslinkable gelatin methacryloyl (GelMA) hydrogels," *Biomaterials Science*, vol. 5, no. 10,

pp. 2093–2105, 2017.

[144] L. T. Denes, L. A. Riley, J. R. Mijares, J. D. Arboleda, K. McKee, K. A. Esser, and E. T. Wang, "Culturing C2C12 myotubes on micromolded gelatin hydrogels accelerates myotube maturation," *Skeletal Muscle*, vol. 9, no. 1, pp. 1–10, 2019.

[145] I. Batalov, Q. Jallerat, S. Kim, J. Bliley, and A. W. Feinberg, "Engineering aligned human cardiac muscle using developmentally inspired fibronectin micropatterns," *Scientific Reports*, vol. 11, no. 1, p. 11502, 2021.

[146] W. S. Rasband, "ImageJ," *US National Institutes of Health, Bethesda, Maryland, USA, https://imagej.nih.gov/ij/*, 2005.

[147] T. S. H. Tran, B. D. Ho, J. P. Beech, and J. O. Tegenfeldt, "Open channel deterministic lateral displacement for particle and cell sorting," *Lab Chip*, vol. 17, no. 21, pp. 3592–3600, 2017.

[148] E. Brauer, E. Lippens, O. Klein, G. Nebrich, S. Schreivogel, G. Korus, G. N. Duda, and A. Petersen, "Collagen Fibrils Mechanically Contribute to Tissue Contraction in an In Vitro Wound Healing Scenario," *Advanced Science*, vol. 6, no. 9, 2019.

[149] M. Borowiak, F. Küllmer, F. Gegenfurtner, S. Peil, V. Nasufovic, S. Zahler, O. Thorn-Seshold, D. Trauner, and H.-D. Arndt, "Optical Manipulation of F-Actin with Photoswitchable Small Molecules," *Journal of the American Chemical Society*, vol. 142, no. 20, pp. 9240–9249, 2020.

[150] X. Fan, W. Nie, H. Tsai, N. Wang, H. Huang, Y. Cheng, R. Wen, L. Ma, F. Yan, and Y. Xia, "PEDOT:PSS for Flexible and Stretchable Electronics: Modifications, Strategies, and Applications," *Advanced Science*, vol. 6, no. 19, p. 1900813, 2019.

[151] F. Amorini, I. Zironi, M. Marzocchi, I. Gualandi, M. Calienni, T. Cramer, B. Fraboni, and G. Castellani, "Electrically Controlled "sponge Effect" of PEDOT:PSS Governs Membrane Potential and Cellular Growth," *ACS Applied Materials and Interfaces*, vol. 9, no. 8, pp. 6679–6689, 2017.

[152] B. J. Worfolk, S. C. Andrews, S. Park, J. Reinspach, N. Liu, M. F. Toney, S. C. Mannsfeld, and Z. Bao, "Ultrahigh electrical conductivity in solution-sheared polymeric transparent films," *Proceedings of the National Academy of Sciences of the United States of America*, vol. 112, no. 46, pp. 14138–14143, 2015.

[153] H. Shi, C. Liu, Q. Jiang, and J. Xu, "Effective Approaches to Improve the Electrical Conductivity of PEDOT:PSS: A Review," *Advanced Electronic Materials*, vol. 1, no. 4, p. 1500017, 2015.

[154] A. Sanchez-Sanchez, I. del Agua, G. G. Malliaras, and D. Mecerreyes, "Conductive Poly(3,4-Ethylenedioxythiophene) (PEDOT)-Based Polymers and Their Applications in Bioelectronics," *Smart Polymers and their Applications*, pp. 191–

218, 2019.

[155] D. Khodagholy, T. Doublet, P. Quilichini, M. Gurfinkel, P. Leleux, A. Ghestem, E. Ismailova, T. Hervé, S. Sanaur, C. Bernard, and G. G. Malliaras, "In vivo recordings of brain activity using organic transistors," *Nature Communications*, vol. 4, no. 1, p. 1575, 2013.

[156] A. G. Guex, J. L. Puetzer, A. Armgarth, E. Littmann, E. Stavrinidou, E. P. Giannelis, G. G. Malliaras, and M. M. Stevens, "Highly porous scaffolds of PE-DOT:PSS for bone tissue engineering," *Acta Biomaterialia*, vol. 62, pp. 91–101, 2017.

[157] P. J. Molino, L. Garcia, E. M. Stewart, M. Lamaze, B. Zhang, A. R. Harris, P. Winberg, and G. G. Wallace, "PEDOT doped with algal, mammalian and synthetic dopants: polymer properties, protein and cell interactions, and influence of electrical stimulation on neuronal cell differentiation," *Biomaterials Science*, vol. 6, no. 5, pp. 1250–1261, 2018.

[158] B. Yang, F. Yao, L. Ye, T. Hao, Y. Zhang, L. Zhang, D. Dong, W. Fang, Y. Wang, X. Zhang, C. Wang, and J. Li, "A conductive PEDOT/alginate porous scaffold as a platform to modulate the biological behaviors of brown adipose-derived stem cells," *Biomaterials Science*, vol. 8, no. 11, pp. 3173–3185, 2020.

[159] I. del Agua, D. Mantione, U. Ismailov, A. Sanchez-Sanchez, N. Aramburu, G. G. Malliaras, D. Mecerreyes, and E. Ismailova, "DVS-Crosslinked PEDOT:PSS Free-Standing and Textile Electrodes toward Wearable Health Monitoring," *Advanced Materials Technologies*, vol. 3, no. 10, pp. 1–8, 2018.

[160] U. Lang, N. Naujoks, and J. Dual, "Mechanical characterization of PEDOT:PSS thin films," *Synthetic Metals*, vol. 159, no. 5-6, pp. 473–479, 2009.

[161] L. V. Kayser and D. J. Lipomi, "Stretchable Conductive Polymers and Composites Based on PEDOT and PEDOT:PSS," *Advanced Materials*, vol. 31, no. 10, p. 1806133, 2019.

[162] J. E. Collazos-Castro, J. L. Polo, G. R. Hernández-Labrado, V. Padial-Cañete, and C. García-Rama, "Bioelectrochemical control of neural cell development on conducting polymers," *Biomaterials*, vol. 31, no. 35, pp. 9244–9255, 2010.

[163] A. Shahini, M. Yazdimamaghani, K. J. Walker, M. Eastman, H. Hatami-Marbini, B. Smith, J. L. Ricci, S. Madihally, and D. Vashaee, "3D conductive nanocomposite scaffold for bone tissue engineering," *International Journal of Nanomedicine*, vol. 9, no. 1, p. 167, 2013.

[164] A. M.-D. Wan, S. Inal, T. Williams, K. Wang, P. Leleux, L. Estevez, E. P. Giannelis, C. Fischbach, G. G. Malliaras, and D. Gourdon, "3D conducting polymer platforms for electrical control of protein conformation and cellular functions," *Journal of Materials Chemistry B*, vol. 3, no. 25, pp. 5040–5048, 2015.

[165] G. Shao, D. A. H. Hanaor, X. Shen, and A. Gurlo, "Freeze Casting: From Low-Dimensional Building Blocks to Aligned Porous Structures—A Review of Novel Materials, Methods, and Applications," *Advanced Materials*, vol. 32, no. 17, p. 1907176, 2020.

[166] S. Inal, A. Hama, M. Ferro, C. Pitsalidis, J. Oziat, D. Iandolo, A.-M. Pappa, M. Hadida, M. Huerta, D. Marchat, P. Mailley, and R. M. Owens, "Conducting Polymer Scaffolds for Hosting and Monitoring 3D Cell Culture," *Advanced Biosystems*, vol. 1, no. 6, p. 1700052, 2017.

[167] F. Rasch, C. Schmitt, L. M. Saure, R. Meyer, V. Adamski, D. Dengiz, R. Scherließ, R. Lucius, M. Synowitz, Y. K. Mishra, K. Hattermann, R. Adelung, J. Held-Feindt, and F. Schütt, "Macroscopic Silicone Microchannel Matrix for Tailored Drug Release and Localized Glioblastoma Therapy," *ACS Biomaterials Science and Engineering*, vol. 6, no. 6, pp. 3388–3397, 2020.

[168] L. S. Pingree, B. A. MacLeod, and D. S. Ginger, "The changing face of PEDOT:PSS films: Substrate, bias, and processing effects on vertical charge transport," *Journal of Physical Chemistry C*, vol. 112, no. 21, pp. 7922–7927, 2008.

[169] J. Liao, Y. Zhu, Z. Zhou, J. Chen, G. Tan, C. Ning, and C. Mao, "Reversibly Controlling Preferential Protein Adsorption on Bone Implants by Using an Applied Weak Potential as a Switch," *Angewandte Chemie International Edition*, vol. 53, no. 48, pp. 13068–13072, 2014.

[170] A. Magaz, B. F. Spencer, J. G. Hardy, X. Li, J. E. Gough, and J. J. Blaker, "Modulation of Neuronal Cell Affinity on PEDOT-PSS Nonwoven Silk Scaffolds for Neural Tissue Engineering," *ACS Biomaterials Science and Engineering*, vol. 6, no. 12, pp. 6906–6916, 2020.

[171] J. H. Lin, H. Y. Chang, W. L. Kao, K. Y. Lin, H. Y. Liao, Y. W. You, Y. T. Kuo, D. Y. Kuo, K. J. Chu, Y. H. Chu, and J. J. Shyue, "Effect of Surface Potential on Extracellular Matrix Protein Adsorption," *Langmuir*, vol. 30, no. 34, pp. 10328–10335, 2014.

[172] J. S. Nanda and J. R. Lorsch, "Labeling a protein with fluorophores using NHS ester derivitization," *Methods in Enzymology*, vol. 536, pp. 87–94, 2014.

[173] R. T. Kendall and C. A. Feghali-Bostwick, "Fibroblasts in fibrosis: novel roles and mediators," *Frontiers in Pharmacology*, vol. 5, p. 123, 2014.

[174] K. Legerstee, B. Geverts, J. A. Slotman, and A. B. Houtsmuller, "Dynamics and distribution of paxillin, vinculin, zyxin and VASP depend on focal adhesion location and orientation," *Scientific Reports*, vol. 9, no. 1, p. 10460, 2019.

[175] P. D. Nguyen, S. T. Hsiao, P. Sivakumaran, S. Y. Lim, and R. J. Dilley, "Enrichment of neonatal rat cardiomyocytes in primary culture facilitates long-term maintenance of contractility in vitro," *American Journal of Physiology-Cell Phys-*

iology, vol. 303, no. 12, pp. C1220–C1228, 2012.

[176] R. B.-K. Wakshlak, R. Pedahzur, and D. Avnir, "Antibacterial activity of silver-killed bacteria: the "zombies" effect," *Scientific Reports*, vol. 5, no. 1, p. 9555, 2015.

[177] I.-L. Steffensen, O. Mesna, E. Andruchow, E. Namork, K. Hylland, and R. Andersen, "Cytotoxicity and accumulation of Hg, Ag, Cd, Cu, Pb and Zn in human peripheral T and B lymphocytes and monocytes In Vitro," *General Pharmacology: The Vascular System*, vol. 25, no. 8, pp. 1621–1633, 1994.

[178] Q. Lang, Y. Wu, Y. Ren, Y. Tao, L. Lei, and H. Jiang, "AC Electrothermal Circulatory Pumping Chip for Cell Culture," *ACS Applied Materials & Interfaces*, vol. 7, no. 48, pp. 26792–26801, 2015.

[179] M. Marotta, R. Bragós, and A. M. Gómez-Foix, "Design and performance of an electrical stimulator for long-term contraction of cultured muscle cells," *BioTechniques*, vol. 36, no. 1, pp. 68–73, 2004.

[180] EFSA, "Opinion of the Scientific Panel on Animal Health and Welfare (AHAW) on a request from the Commission related to the aspects of the biology and welfare of animals used for experimental and other scientific purposes," *EFSA Journal*, vol. 3, no. 12, p. 292, 2005.

[181] U. Strähle, S. Scholz, R. Geisler, P. Greiner, H. Hollert, S. Rastegar, A. Schumacher, I. Selderslaghs, C. Weiss, H. Witters, and T. Braunbeck, "Zebrafish embryos as an alternative to animal experiments—A commentary on the definition of the onset of protected life stages in animal welfare regulations," *Reproductive Toxicology*, vol. 33, no. 2, pp. 128–132, 2012.

[182] J. Wittbrodt, A. Shima, and M. Schartl, "Medaka — a model organism from the far east," *Nature Reviews Genetics*, vol. 3, no. 1, pp. 53–64, 2002.

[183] G. Matrone, C. S. Tucker, and M. A. Denvir, "Cardiomyocyte proliferation in zebrafish and mammals: lessons for human disease," *Cellular and Molecular Life Sciences*, vol. 74, no. 8, pp. 1367–1378, 2017.

[184] V. Sander, G. Suñe, C. Jopling, C. Morera, and J. C. I. Belmonte, "Isolation and in vitro culture of primary cardiomyocytes from adult zebrafish hearts," *Nature Protocols*, vol. 8, no. 4, pp. 800–809, 2013.

[185] W. Xu, H. Li, L. Peng, L. Pu, S. Xiang, Y. Li, L. Tao, W. Liu, J. Liu, Y. Xiao, and S. Liu, "Fish Pluripotent Stem-Like Cell Line Induced by Small-Molecule Compounds From Caudal Fin and its Developmental Potentiality," *Frontiers in Cell and Developmental Biology*, vol. 9, pp. 1–11, 2022.

[186] B. Zimerman, T. Volberg, and B. Geiger, "Early molecular events in the assembly of the focal adhesion-stress fiber complex during fibroblast spreading," *Cell Motility and the Cytoskeleton*, vol. 58, no. 3, pp. 143–159, 2004.

[187] D. Yaffe and O. Saxel, "Serial passaging and differentiation of myogenic cells isolated from dystrophic mouse muscle," *Nature*, vol. 270, no. 5639, pp. 725–727, 1977.

[188] Verena Schwach and Robert Passier, "Native cardiac environment and its impact on engineering cardiac tissue," *Biomaterials Science*, vol. 7, no. 9, pp. 3566–3580, 2019.

[189] S. Sayyar, E. Murray, B. C. Thompson, J. Chung, D. L. Officer, S. Gambhir, G. M. Spinks, and G. G. Wallace, "Processable conducting graphene/chitosan hydrogels for tissue engineering," *Journal of Materials Chemistry B*, vol. 3, no. 3, pp. 481–490, 2015.

[190] A. Alam, H. C. Kuan, Z. Zhao, J. Xu, and J. Ma, "Novel polyacrylamide hydrogels by highly conductive, water-processable graphene," *Composites Part A: Applied Science and Manufacturing*, vol. 93, pp. 1–9, 2017.

[191] S. Das, F. Irin, L. Ma, S. K. Bhattacharia, R. C. Hedden, and M. J. Green, "Rheology and morphology of pristine graphene/polyacrylamide gels," *ACS Applied Materials and Interfaces*, vol. 5, no. 17, pp. 8633–8640, 2013.

[192] B. Li, C. Wu, C. Wang, Z. Luo, and J. Cao, "Fabrication of tough, self-recoverable, and electrically conductive hydrogels by in situ reduction of poly(acrylic acid) grafted graphene oxide in polyacrylamide hydrogel matrix," *Journal of Applied Polymer Science*, vol. 137, no. 23, p. 48781, 2020.

[193] K. Awasthi, R. Kumar, H. Raghubanshi, S. Awasthi, R. Pandey, D. Singh, T. P. Yadav, and O. N. Srivastava, "Synthesis of nano-carbon (nanotubes, nanofibres, graphene) materials," *Bulletin of Materials Science*, vol. 34, no. 4, pp. 607–614, 2011.

[194] M. Boruah, P. Phukon, B. jyoti Saikia, and S. Dolui, "Electrical actuation of electroresponsive hydrogels based on poly(acrylamide- co -acrylic acid)/graphite suitable for biomedical applications," *Polymer Composites*, vol. 35, no. 1, pp. 27–36, 2014.

[195] A. Alam and M. Moussa, "Preparation of graphene/poly(vinyl alcohol) composite hydrogel films with enhanced electrical and mechanical properties," *Polymer Composites*, vol. 41, no. 3, pp. 809–816, 2020.

[196] S. Sayyar, S. Gambhir, J. Chung, D. L. Officer, and G. G. Wallace, "3D printable conducting hydrogels containing chemically converted graphene," *Nanoscale*, vol. 9, no. 5, pp. 2038–2050, 2017.

[197] X. Liu, A. L. Miller, S. Park, B. E. Waletzki, Z. Zhou, A. Terzic, and L. Lu, "Functionalized Carbon Nanotube and Graphene Oxide Embedded Electrically Conductive Hydrogel Synergistically Stimulates Nerve Cell Differentiation," *ACS Applied Materials and Interfaces*, vol. 9, no. 17, pp. 14677–14690, 2017.

[198] B. Qu, C. Chen, L. Qian, H. Xiao, and B. He, "Facile preparation of conductive composite hydrogels based on sodium alginate and graphite," *Materials Letters*, vol. 137, pp. 106–109, 2014.

[199] P. J. Bora, A. G. Anil, K. J. Vinoy, and P. C. Ramamurthy, "Outstanding Absolute Electromagnetic Interference Shielding Effectiveness of Cross-Linked PEDOT:PSS Film," *Advanced Materials Interfaces*, vol. 6, no. 22, p. 1901353, 2019.

A | Supplementary general information

A.1. Cell lines and tissue

REF52 wt are rat embryonic fibroblasts wild type cells. Fibroblasts are incompletely differentiated cells and are the most common cells in the connective tissue. They are important for tissue development, are responsible for secreting extracellular matrix (ECM) precursors and thus preserve the structural integrity of the connective tissue. [173] REF52 wt cells were isolated from rat embryos (B.Geiger, Weizmann Institute, Israel). [186]

C2C12 is an immortalized mouse myoblast cell line originally derived by Yaffe and Saxel in 1977. [187] The cells undergo rapid proliferation under high serum conditions, whereas the myoblasts fuse into myotubes with an ability to contract and exert forces under low serum conditions or starvation.

iPSC-CM are cardiomyocytes differentiated from induced pluripotent stem cells, which are able to self-replicate and differentiate into any cell type in the body. [188]

Fish heart isolated from medaka The Japanese medaka fish (*Oryzias latipes*) is a small, egg-laying fresh-water fish that is easy to bread and very tolerant against a wide range of salinities and temperatures between 10 to 40 °C. [182]

A.2. Cell culture

In general, cells were cultured in Dulbecco's modified Eagle's medium (DMEM, PAN-Biotech) supplemented with 10 % fetal bovine serum (FBS, PAN-Biotech) and 1 % Penicillin/Streptomycin (Sigma-Aldrich) at 37 °C with a CO_2 level of 5 % and about 90 % humidity. Rat embryonic fibroblasts (REF52 wt) are used at 70 - 80 %, skeletal muscle cells (C2C12) at 60 - 70 % confluency. For detaching cells Accutase® (PAN-Biotech) is used and cells were centrifuged at 800 x g for 4 minutes or 200 x g for 5 minutes,

respectively. Cardiomyocytes from induced pluripotent stem cells (iPSC-CMs) were differentiated and cultured in the group of Prof. Dr. med. Johannes Backs from Heidelberg University Hospital. Medaka fish are bred and maintained in the group of Prof. Dr. Jochen Wittbrodt from Heidelberg University.

A.3. Cell viability assay

Information about the cytotoxicity of biomaterials on cells can be obtained by using the MTT tetrazolium reduction assay in agreement with ISO-10993. In an MTT assay methylthiazolyldiphenyl-tetrazolium bromide (MTT; Sigma-Aldrich) is converted into a purple colored crystalline formazan product by viable cells with active metabolism. Dead cells are not able to convert the dye, thus the color formation can be assumed to be directly proportional to the number of viable cells. [129] For an indirect MTT assay, extractions are prepared by incubating samples in culture medium (for fibroblasts: Dulbecco's modified Eagle's medium (DMEM) supplemented with 10% fetal bovine serum (FBS) and 1% penicillin/streptomycin.) for $24\,h$ at $37\,°C$. $1{\cdot}10^4$ cells are seeded in a 96-well plate and incubated in $100\,µL$ culture medium for 24 hours. Afterwards, the medium is removed and a dilution series of the extract medium (30%, 50%, 70%, 100% of extract medium) with culture medium as the diluent is added to the wells. Culture medium with 10% dimethyl sulfoxide (DMSO) is used as a positive control and pure culture medium as a negative control. After 24 hours of incubation the medium is removed and $50\,µL$ of MTT solution ($1\,mg\,mL^{-1}$; in culture medium) is added to each well. After 2 hours of incubation, the MTT solution is exchanged with $100\,µL$ isopropanol and the absorbance is measured at $570\,nm$ (Epoch 2, BioTek). The blank value (empty wells, OD_{blank}) is calculated as an arithmetic mean and subtracted from all measured values. To calculate the cytotoxicity of the test substances the values obtained from the negative control are set as 100% (OD_{negative}) and the cell viability is calculated as follows:

$$\text{cell viability}\,(\%) = \frac{(OD_{\text{sample}} - OD_{\text{blank}}) \cdot 100}{OD_{\text{negative}} - OD_{\text{blank}}} \tag{A.1}$$

OD is short for optical density. OD_{sample} is the measured optical density of the tested samples.

A.4. Fluorescent staining

A.4.1. Live/Dead assay

For a live/dead assay CalceinAM (Sigma-Aldrich) and Propidium Iodide (PI, Thermo Fisher Scientific) at concentrations of $1\,µg\,mL^{-1}$ were used. Optionally, Hoechst

(Thermo Fisher Scientific) can be added to stain cell nuclei at the same concentration. After 20 minutes of incubation protected from light, samples are washed three times with PBS and afterwards imaged with GFP, RFP and DAPI filter units.

A.4.2. Immunofluorescent staining

Cells are fixed with paraformaldehyde (PFA, 4 %, Sigma-Aldrich) for 20 minutes at room temperature, followed by cell permeabilization with 0.1 % Triton X-100 (Sigma-Aldrich) for 15 min. Afterwards, non-specific antigens are blocked with bovine serum albumin (BSA, Sigma-Aldrich, 1 %, 20 min) and subsequently samples are incubated with primary antibodies diluted in BSA over night at 4 °C. The next day, samples are incubated with the secondary antibodies diluted in BSA for two hours at room temperature. Additionally, cells can be stained with phalloidin conjugated with rhodamine or iFluor 488, which is added during the secondary antibody reaction step as well. In the last 20 minutes of incubation time, Hoechst ($1\,\mu g\,mL^{-1}$, Thermo Fischer Scientific) is added for nuclei staining. Between each step, the samples are washed extensively with PBS (3x, 5 min). Antibodies used in this thesis are shown in Table A.1. Images were acquired with GFP, RFP, Cy5 and DAPI filter units with an IX81 Olympus inverted microscope or with a Nikon A1R confocal microscope.

Table A.1. Primary and secondary antibodies used in this work.

	Antigen	Produced in	Conjugation	Concentration	Manufacturer
Primary	Myosin heavy chain 7	Mouse	unconjugated	1:100	antibodies-online GmbH
	Zyxin	Rabbit	unconjugated	1:100	SigmaAldrich (Z4751)
	Paxillin	Mouse	unconjugated	1:250	Invitrogen (AHO0492)

	Host species	Target species	Conjugation	Concentration	Manufacturer
Secondary	Goat	Mouse	Alexa Fluor® 488	1:500	abcam (ab150113)
	Goat	Mouse	Alexa Fluor® 568	1:500	abcam (ab175473)
	Goat	Mouse	Alexa Fluor® 647	1:500	abcam (ab150115)
	Goat	Rabbit	Alexa Fluor® 488	1:500	abcam (ab150077)
	Goat	Rabbit	Alexa Fluor® 568	1:500	abcam (ab175471)
	Goat	Rabbit	Cy5®	1:500	abcam (ab6564)
	-	-	Rhodamine-Phalloidin	1:300	abcam (ab235138)
	-	-	Phalloidin-iFluor488	1:300	abcam (ab176753)

B | Supplementary information for Chapter 2

B.1. Fabrication of microchannel-containing PAM-EG networks

Table B.1 shows the components and amount necessary for the polyacrylamide synthesis. Recipe A refers here to the original recipe used for almost all experiments in Chapter 2. Recipe B was used to restore mechanical properties for scaffolds with $0.32\,\mathrm{vol\,\%}$ exfoliated graphene and PAM-GelMA composites. Higher amounts and/or concentrations of ammonium persulfate and N, N, N', N'-tetramethylethylenediamine were necessary because exfoliated graphene acted as a radical scavenger during polyacrylamide synthesis.

B.2. Diffusion experiments

Diffusion through bulk PAM samples and network PAM samples obtained from 0.3 and $0.9\,\mathrm{g\,cm^{-3}}$ sacrificial t-ZnO templates was analyzed via methylene blue diffusion and absorption (Figure B.1). Two half-cells separated by a wall containing a hole for the samples to act as diffusional membranes were used, which were either filled with distilled water or an aqueous methylene blue solution (MB, Eydam, $2.5\,\mathrm{mM}$). After specific time points, $1\,\mathrm{mL}$ of the solution from the water-filled half-cell was analyzed using an UV-Vis spectrometer (Lambda 9000 by Perkin Elmer) by recording absorption spectra in a range of 550 to $750\,\mathrm{nm}$. The solution was placed back in the respective half-cell after the measurement. Absorption values at $662\,\mathrm{nm}$ were extracted from the spectra for each sample type and time point and absorption values for network PAM were normalized to the absorption value of bulk PAM as shown in Figure B.1. Although methylene blue also diffuses through the PAM matrix, the results clearly indicate that the microchannel network enhances the diffusion as the values of network PAM samples are twice as high as that of bulk PAM after 30 hours.

Table B.1. Components for the synthesis of polyacrylamide hydrogels

	Component	Quantity (μL)		Manufacturer
		Recipe A	Recipe B	
Precursor	40 % acrylamide solution	1250	1250	BioRad
	2 % bis-acrylamide solution	1000	1000	BioRad
	HEPES, pH = 7.5	50	50	SigmaAldrich
	Double distilled water	2625	2625	-
	APS	75 (10 %($\frac{w}{v}$))	75 (20 %($\frac{v}{v}$))	SigmaAldrich
	TEMED	100 (10 %($\frac{w}{v}$))	200 (18.2 %($\frac{v}{v}$))	SigmaAldrich

APS = ammonium persulfate; bis-acrylamide = N, N'-methylenebis(acrylamide); HEPES = 4-(2-hydroxyethyl)-1-piperazineethanesulfonic acid, TEMED = N, N, N', N'-tetramethylethylenediamine
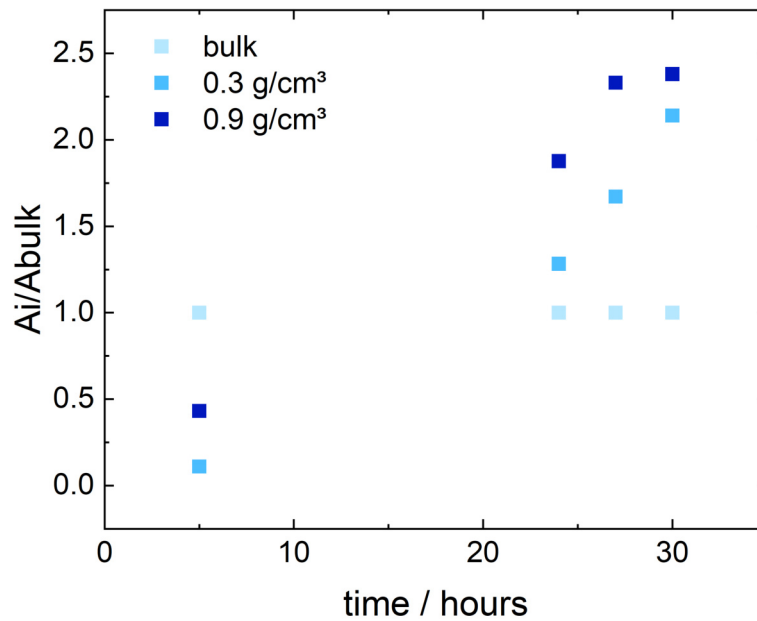
Figure B.1. *Absorption values A_i (λ = 662 nm) normalized to the values of bulk PAM (A_{bulk}) measured with UV-Vis for different time points for bulk PAM, network PAM (0.3 g cm^{-3} t-ZnO template) and network PAM (0.9 g cm^{-3} t-ZnO template) samples.*

B.3. TNBS assay

To determine the degree of substitution (DS) of gelatin methacryloyl (GelMA) a TNBS assay [102] is performed. TNBS is 2,4,6-Trinitrobenzene sulfonic acid, which reacts with primary amines to form a highly chromogenic product that is orange in color. For the assay, gelatin and GelMA samples are dissolved at a concentration of $1.6\,\mathrm{mg\,mL^{-1}}$ in $0.1\,\mathrm{mol\,L^{-1}}$ sodium bicarbonate buffer. To $500\,\mathrm{\mu L}$ of the sample solution $500\,\mathrm{\mu L}$ of $0.01\,\%$ TNBS is added and incubated for two hours at $37\,°\mathrm{C}$. Afterwards, $250\,\mathrm{\mu L}$ of $10\,\%$ sodium dodecyl sulfate and $125\,\mathrm{\mu L}$ of hydrochloric acid $(1\,\mathrm{mol\,L^{-1}})$ are added and the absorbance is measured at $335\,\mathrm{nm}$ (Epoch 2, BioTek). As a standard glycine $(\mathrm{M}_W = 75.07\,\mathrm{g\,mol^{-1}})$ with one free amine group per molecule is used. An example of a standard curve and the chemical formula of glycine are displayed in Figure B.2 a. The absorption values at $335\,\mathrm{nm}$ of concentrations of glycine with 0.8, 2, 4, 8, 16 and $32\,\mathrm{\mu g\,mL^{-1}}$ in $0.1\,\mathrm{mol\,L^{-1}}$ in sodium bicarbonate buffer are plotted and fitted linearly. Figure B.2 b shows exemplary absorption spectra of gelatin and GelMA. With the linear fit, the concentrations of primary amines present in gelatin and GelMA and subsequently by comparison the degree of substitution can be determined.
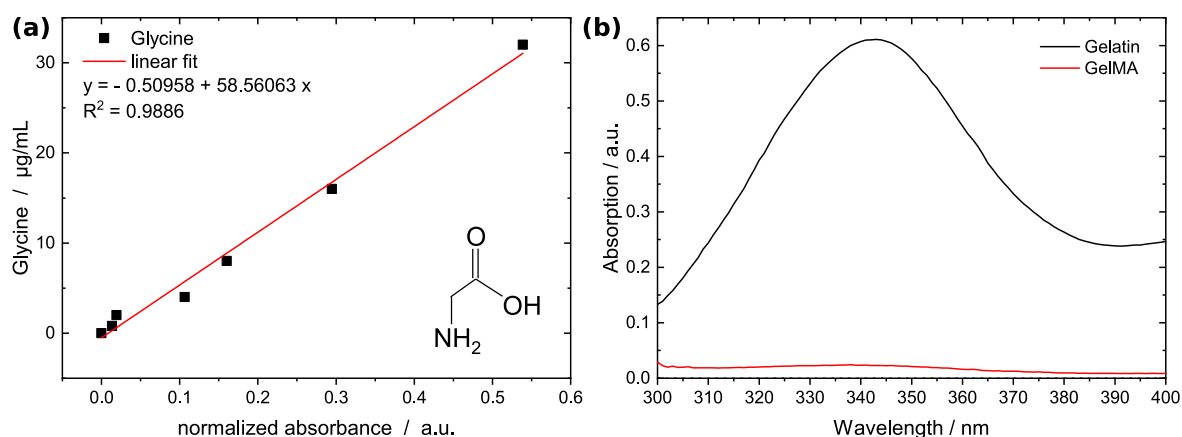
Figure B.2. *a) Exemplary standard curve with linear fit (red) for determining the degree of substitution of gelatin methacryloyl. Glycine which has one free amine group (chemical formula displayed) was used for the standard curve. b) Absorption spectra of gelatin (black) and GelMA (red). Absorption values at 335 nm are used for determining the degree of substitution.*

B.4. Photoinitiated polymerization

Hydrogels used in this thesis are crosslinked by free radical polymerization. For radical generation, photoinitiators can be used, which are activated upon exposure to UV ($365\,\mathrm{nm}$) or blue ($405\,\mathrm{nm}$) light. The lamps used are from Sahlmann Photochemical solutions (Nichia NVSU233A-U365 or Nichia NVSU233A-U405 LEDs). The irradiance, measured with a laser power and energy meter (Coherent), as a function of lamp

intensity[1] is shown in Figure B.3 for 365 and 405 nm LEDs, respectively. For 405 nm, the decrease in absorption by a cover glass is shown as well. The intensity loss is approximately 8 %.
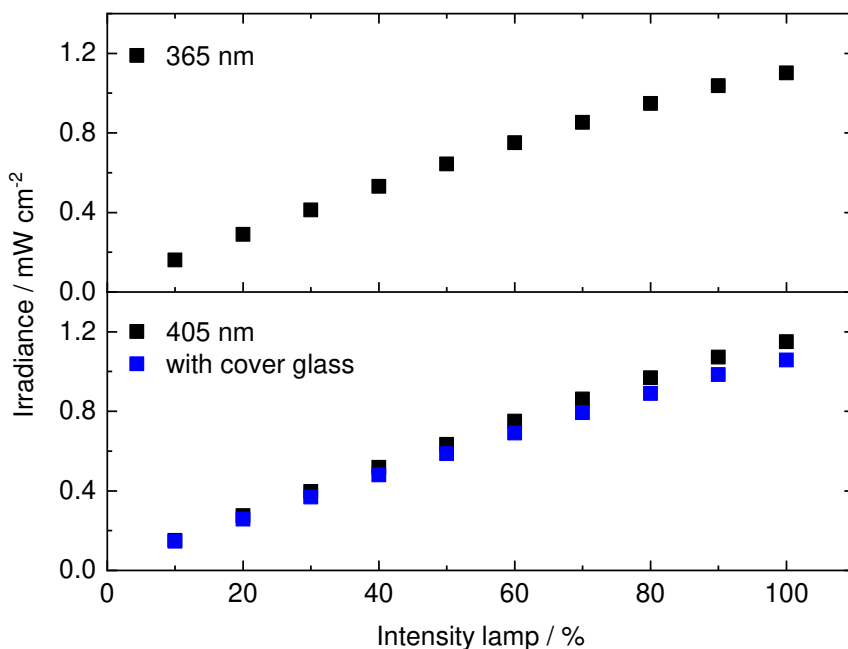
Figure B.3. *Irradiance E of 365 and 405 nm LEDs as a function of lamp intensity is shown. Intensities determined here are used to calculate the UV dose for the individual reactions.*

B.5. Microindentation measurement

Samples to be measured in a microindenter (Pavone, Optics11 Life) have to be fixed to prevent floating. To promote hydrogels to stick to their glass substrate, the glass slides are pretreated with methacrylate. Glass slides were cleaned three times with double-distilled water and ethanol and are afterwards incubated over night in a solution of ethanol (19.1 mL), double-distilled water (800 µL) and 3-(Trimethoxysilyl)propyl methacrylate (100 µL; Sigma-Aldrich). The next day, cover slips are washed twice with double-distilled water and ethanol followed by heat-treatment at 80 °C over night. For sample preparation, 380 µL of hydrogel precursor solution is placed between a silanized glass slide and a round coverslip with a diameter of 22 mm, which is removed after hydrogel polymerization. This results in a hydrogel with a height of 1 mm with an even surface. The polymerization reaction is either initiated by the APS/TEMED radical

---

[1]100 % = 4 x 1400 mW = 5600 mW

formation system or by photoinitiators. To induce photopolymerization, the samples are subsequently exposed to UV or blue light, respectively. After polymerization, samples are stored in double distilled water at $4\,^\circ$C until the measurement.

Figure B.4 shows an exemplary recorded force-distance curve (black) for a GelMA sample with $97\,\%$ degree of substitution. The Young's modulus is determined by applying a Hertzian fit (red) using the software DataViewer (V.2.4.0, Optics11). Fits with a $R^2 \leq 0.97$ were excluded and the Poisson's ratio ν is assumed with 0.5.
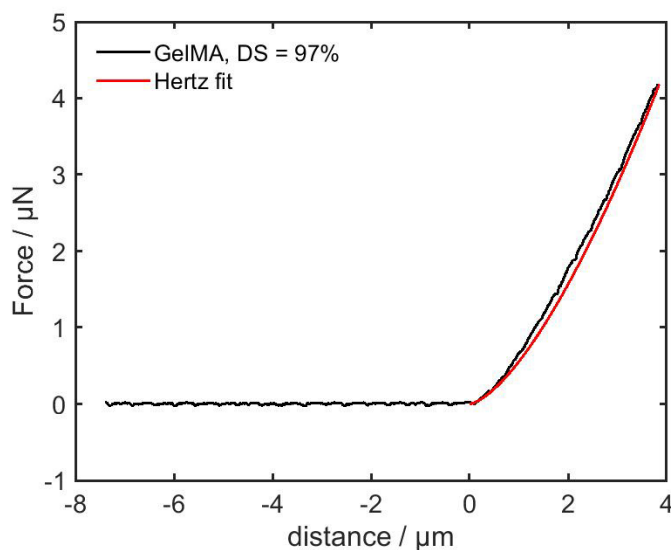
Figure B.4. *Force-distance curve of GelMA sample (degree of substitution (DS) = 97 %) measured by microindentation (black). A Hertz fit (red) is used to determine the Young's modulus.*

B.6. Supplementary information for Figure 2.9 and Figure 2.15

In Table B.2 and Table B.3 information about different conductive hydrogels based on carbon fillers from literature are shown and compared with the microengineered conductive hydrogel.

Table B.2. Data and references of electrically conductive hydrogels from Figure 2.9

Hydrogel	Filler material	Preparation method	Filler conc. (wt%)	Conductivity ($S\,m^{-1}$)	Reference
Chitosan-lactic acid	graphene	solution mix.	3.0	0.133	Sayyar et al. [189]
PAM	graphene	in situ polym.	4.0	20.0	Didehban et al. [124]
PAM	graphene	in situ polym.	3.0	$3.56 \cdot 10^{-6}$	Alam et al. [190]
PAM	graphene	in situ polym.	2.0	$1.02 \cdot 10^{-6}$	Das et al. [191]
PAM	rGO	in situ polym.	1.2	$9.1 \cdot 10^{-5}$	Li et al. [192]
PAM	MWCNTs	in situ polym.	40.0	120.0	Awasthi et al. [193]
PAM	MWCNTs	in situ polym.	15.0	$3.48 \cdot 10^{-4}$	Awasthi et al. [193]
PAM	CNTs	solution mix.	1.0	0.085	Chen et al. [20]
Poly(AAm-co-AAc)	graphite	solution mix.	9.0	9.2	Boruah et al. [194]
PVA	graphene	solution mix.	10.0	$1.33 \cdot 10^{-6}$	Alam et al. [195]
PVBA	CNT-CNF	in situ polym.	0.3	0.8	Han et al. [120]
PVBA	CNT-CNF	in situ polym.	0.5	8.0	Han et al. [120]
PVBA	CNT-CNF	in situ polym.	0.7	10.0	Han et al. [120]
Methacrylated chitosan	graphene	solution mix.	3.0	0.25	Sayyar et al. [196]
Methacrylated chitosan	graphene	solution mix.	1.5	0.02	Sayyar et al. [196]
OPF	rGOa/CNT pega	solution mix.	1.1	$3 \cdot 10^{-3}$	Liu et al. [197]
Sodium alginate	graphite	solution mix.	30.0	0.17	Qu et al. [198]
PAM	Exfoliated graphene	Microengineered graphene tube system	0.06	0.012	Arndt et al. [115]
			0.12	0.08	
			0.20	0.34	
			0.47	1.8	

CNTs = carbon nanotubes; CNT-CNF = carbon nanotube cellulose nanofiber; mix. = mixing; MWCNTs = multi-walled carbon nanotubes; OPF = Oligo(poly(ethylene glycol)fumarate); rGO = reduced graphene oxide; Poly(AAm-co-AAc) = poly(acrylamide-co-acrylic acid); PAM = polyacrylamide; polym. = polymerization; PVA = poly(vinyl alcohol); PVBA = polyvinyl alcohol-borax

Table B.3. Data and references of electrically conductive hydrogels from Figure 2.15

Hydrogel	Filler material	Preparation method	Filler conc. (wt%)	Normalized conductivity $(\mathrm{S\,m^{-1}\,wt\%^{-1}})$	E at 0 wt% (kPa)	E at x wt% as given (kPa)	increase by factor	Reference
Chitosan-lactic acid	graphene	solution mix.	3.0	$4.4 \cdot 10^{-2}$	$5.8 \cdot 10^{6}$	$1.4 \cdot 10^{7}$	2.35	Sayyar et al. [189]
PAM	graphene	in situ polym.	3.0	$1.19 \cdot 10^{-6}$	$1.8 \cdot 10^{3}$	$4.4 \cdot 10^{3}$	2.44	Alam et al. [190]
PAM	graphene	in situ polym.	1.68	$9.29 \cdot 10^{-6}$	$1.6 \cdot 10^{4}$	$1.9 \cdot 10^{5}$	10.3	Alam et al. [195]
PAM	rGO	in situ polym.	1.2	$7.58 \cdot 10^{-5}$	$7.0 \cdot 10^{2}$	$1.5 \cdot 10^{3}$	2.14	Li et al. [192]
PAM	CNTs	solution mix.	1.0	$8.5 \cdot 10^{-2}$	$1.1 \cdot 10^{3}$	$3.2 \cdot 10^{3}$	2.91	Chen et al. [20]
PVA	graphene	solution mix.	10.0	$1.33 \cdot 10^{-6}$	$1.1 \cdot 10^{5}$	$1.2 \cdot 10^{6}$	11.6	Alam et al. [195]
Methacrylated chitosan	graphene	solution mix.	1.5	$2.0 \cdot 10^{-2}$	$1.8 \cdot 10^{4}$	$4.0 \cdot 10^{4}$	2.22	Sayyar et al. [196]
OPF	rGOa/CNT pega	solution mix.	1.1	$2.7 \cdot 10^{-3}$	$1.8 \cdot 10^{3}$	$5.4 \cdot 10^{3}$	5.35	Liu et al. [197]
PAM	EG	Microengineered graphene tube system	0.20	1.7	45.0	91.0	2.02	Arndt et al. [115]

CNTs = carbon nanotubes; mix. = mixing; MWCNTs = multi-walled carbon nanotubes; OPF = Oligo(poly(ethylene glycol)fumarate); rGO = reduced graphene oxide; PAM = polyacrylamide; polym. = polymerization; PVA = poly(vinyl alcohol)

C | Supplementary information for Chapter 3

C.1. Chemical structure of aero-PEDOT:PSS

The chemical structure of PEDOT:PSS with divinyl sulfone (DVS) as a crosslinking agent used in this thesis is shown in Figure C.1.
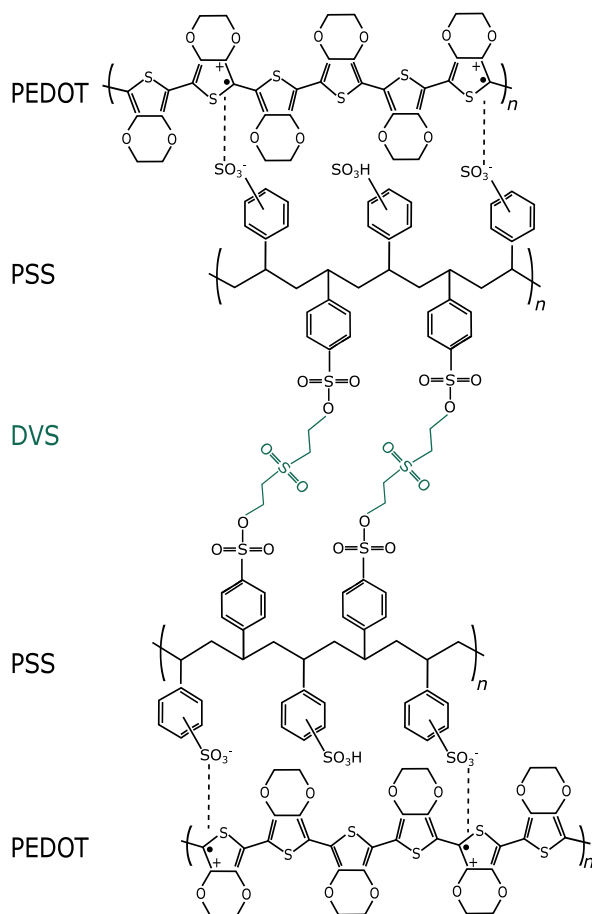
Figure C.1. *Chemical structure of aero-PEDOT:PSS scaffolds with divinyl sulfone (DVS, greenish blue) as a crosslinking agent. Adapted from [199].*

C.2. XPS analysis

The XPS analysis was done by Igor Barg in the group of Prof. Franz Faupel at Kiel University. The spectra in Figure C.2 show PEDOT:PSS samples before (a) and after (b) the wet-chemical treatment with acid to remove the sacrificial t-ZnO template. The intensity of the sulfur (S) 2p peak decreases after the treatment and the ratio between PSS and PEDOT is reduced to 0.34, which means that 66% of PSS is removed by the treatment.
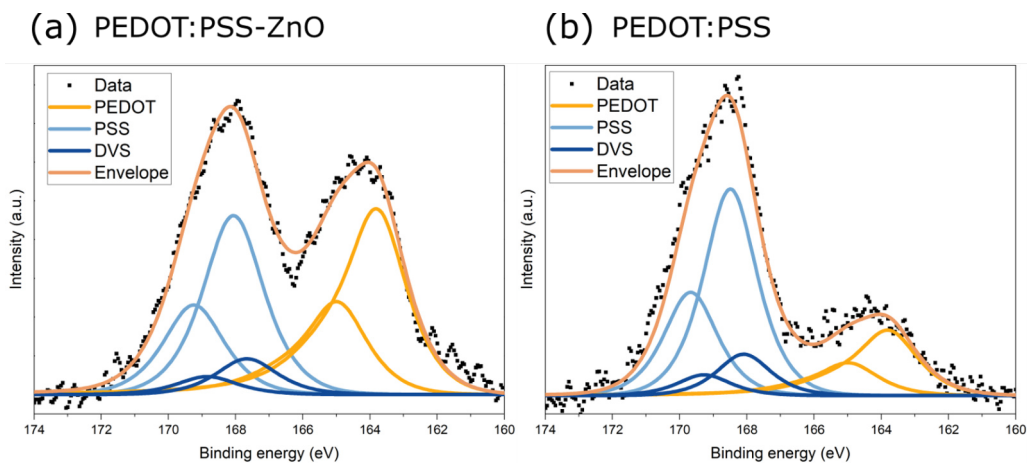
Figure C.2. *XPS spectra of PEDOT:PSS a) on the sacrifical t-ZnO template and b) after the t-ZnO is removed by wet-chemical treatment.*

Acknowledgement

Publications

C. Arndt*, C. Appiah*, K. Siemsen, A. Heitmann, A. Staubitz, and C. Selhuber-Unkel, Living materials herald a new era in soft robotics, *Advanced Materials*, vol. 31, p. 1807747, **2019**.

N. Lukat, R. Friedrich, B. Spetzler, C. Kirchhof, **C. Arndt**, L. Thormählen, F. Faupel and C. Selhuber-Unkel, Mapping of magnetic nanoparticles and cells using thin film magnetoelectric sensors based on the delta-E effect, *Sensors & Actuators: A. Physical*, vol. 309, p. 112023, **2020**.

C. Arndt*, M. Hauck*, I. Wacker, B. Zeller-Plumhoff, F. Rasch, M. Taale, A. S. Nia, X. Feng, R. Adelung, R. R. Schröder, F. Schütt, and C. Selhuber-Unkel, Microengineered hollow graphene tube systems generate conductive hydrogels with extremely low filler concentration, *Nano Letters*, vol. 21, pp. 3690–3697, **2021**.

F. Block, F. Klingbeil, S. Deshpande, U. Sajjad, D. Seidler, **C. Arndt**, S. Sindt, C. Selhuber-Unkel and J. McCord, Unidirectional transport of superparamagnetic beads and biological cells along oval magnetic elements, *Applied Physics Letters*, vol. 118, p. 232405, **2021**.

T. Spratte, **C. Arndt**, I. Wacker, M. Hauck, R. Adelung, R. R. Schröder, F. Schütt and C. Selhuber-Unkel, Thermoresponsive hydrogels with improved actuation function by interconnected microchannels, *Advanced Intelligent Systems*, vol. 4, p. 2100081, **2021**.

P. Dörschmann, S. Boeser*, D. Isik*, **C. Arndt**, J. Roider, C. Selhuber-Unkel and A. Klettner, Influence of carrier materials and coatings on retinal pigment epithelium cultivation and functions, *Experimental Eye Research*, vol. 219, p. 109063, **2022**.

---

*equal contribution

Copyrights

Subject: [SPOOFED?] Request for permission to reuse figures from article in PhD thesis
From: ACS Publications <support@services.acs.org>
Date: 11.11.2021, 17:44
To: christine.arndt@uni-heidelberg.de

Dear Christine Arndt,

Thank you for contacting ACS Publications Help Desk.

Your permission requested is granted and there is no fee for this reuse. In your planned reuse, you must cite the ACS article as the source, https://pubs.acs.org/doi/10.1021/acs.nanolett.0c04375, and further permissions related to the material excerpted should be directed to the ACS.

Should you have any questions or need further assistance, please feel free to contact me.

Sincerely,

Deleep Kumar
ACS Customer Services & Information

Case Info:

Case Number : CSCSI0035323

Created On: 11-11-2021 03:38:11 AM EST

Short Description: Request for permission to reuse figures from article in PhD thesis

Description: Dear Sir or Madam,

I hope this mail finds you well. I am writing because I'd like to reuse or adapt, respectively, figures from the article:

Arndt et. al. "Microengineered Hollow Graphene Tube Systems Generate Conductive Hydrogels with Extremely Low Filler Concentration":

https://doi.org/10.1021/acs.nanolett.0c04375
(https://pubs.acs.org/doi/10.1021/acs.nanolett.0c04375)

for my *PhD thesis*, which I will submit to either Kiel University, Germany or Heidelberg University, Germany, which is not yet decided.

I would like to ask for permission to *reuse or adapt all figures* from the article and from the Supplementary Information.

Sincerely yours,

[SPOOFED?] Request for permission to reuse figures from article in PhD thesis

Christine Arndt

--
M.Sc. Christine Arndt
PhD candidate
Heidelberg University
Institute for Molecular Systems Engineering
Im Neuenheimer Feld 253
69120 Heidelberg

https://www.imse.uni-heidelberg.de/
--
Kiel University
Institute for Materials Science
Kaiserstr. 2
24143 Kiel

Sincerely,

Deleep Kumar

ACS Chemistry for Life
American Chemical Society

Ref:MSG0243449_rdCeszVWecZfdYIfpSjH

Declaration

Eidesstattliche Versicherung gemäß § 8 der Promotionsordnung für die Gesamtfakultät für Mathematik, Ingenieur- und Naturwissenschaften der Universität Heidelberg

1. Bei der eingereichten Dissertation zu dem Thema „Microengineered conductive scaffolds for cell-based actuation" handelt es sich um meine eigenständig erbrachte Leistung.

2. Ich habe nur die angegebenen Quellen und Hilfsmittel benutzt und mich keiner unzulässigen Hilfe Dritter bedient. Insbesondere habe ich wörtlich oder sinngemäß aus anderen Werken übernommene Inhalte als solche kenntlich gemacht.

3. Die Arbeit oder Teile davon habe ich bislang nicht an einer Hochschule des In- oder Auslands als Bestandteil einer Prüfungs- oder Qualifikationsleistung vorgelegt.

4. Die Richtigkeit der vorstehenden Erklärungen bestätige ich.

5. Die Bedeutung der eidesstattlichen Versicherung und die strafrechtlichen Folgen einer unrichtigen oder unvollständigen eidesstattlichen Versicherung sind mir bekannt.

Ich versichere an Eides statt, dass ich nach bestem Wissen die reine Wahrheit erklärt und nichts verschwiegen habe.

Ort, Datum   Unterschrift